Photo-induced ultrafast dynamics and non-linear processes in molecules

Debadarshini Mishra, PhD

University of Connecticut, 2024

Understanding the dynamics of various photo-induced physical and chemical processes in molecules is fundamental to physics, chemistry, and biology. These dynamics, which occur on pico- and femtosecond scales, are observable using ultrafast tools like ultrashort laser pulses that can be generated using tabletop laser and free-electron lasers. This thesis systematically studies some of these processes using different light sources and probing techniques, revealing new physics and offering insights into potential future control of these phenomena.

Building on this foundation, one of our investigations in this thesis uses tabletop laser pulses to examine the ultrafast nuclear dynamics of 1- and 2-propanol upon photoexcitation. Utilizing pump-probe spectroscopy combined with coincident Coulomb explosion imaging, we track the mechanisms leading to multi-body dissociation and identify a novel fragmentation channel in 2-propanol indicative of methyl roaming. This work not only underscores the complex behavior of molecular structures post-excitation but also aligns with comparative studies on similar molecules, enhancing our understanding of molecular behavior under photoexcitation.

Additionally, to extend the scope of coincident Coulomb explosion imaging, we developed a novel ultrafast imaging technique to explore the elusive phenomenon of roaming in acetonitrile.

By employing intense femtosecond IR radiation and sophisticated imaging methods, we captured the trajectories of neutral roaming fragments, contributing to our understanding of this type of molecular dissociation. This method provides a clear experimental signature of roaming, supported by quantum chemistry calculations, and offers a detailed view of this unique dissociative process.

Using free-electron lasers, we explored the energy redistribution dynamics in fullerenes irradiated with intense XUV radiation. By analyzing the kinetic energy spectra of ionic fragments from C_{60} molecules, we observed a transient nanoplasma state, which plays a critical role in energy redistribution within the molecule. This work not only elucidates the complex interplay between molecular and Coulombic forces in large molecules but also provides insights that are applicable to other such large molecular systems.

In the final work presented in this thesis, we investigated the photochemical behavior of 2-bromothiophene, capturing the competition between different photochemical pathways through ultrafast electron diffraction. This approach, distinct from the other works described in this thesis, reveals how excitation wavelengths influence molecular structure, offering strategies for manipulating molecular dynamics and designing photoresponsive materials.

Together, these studied demonstrate the power of time-resolved techniques to probe and investigate the ultrafast dynamics of molecules, paving the way for controlled manipulation of chemical and physical processes at the atomic level.

Photo-induced ultrafast dynamics and non-linear processes in molecules

Debadarshini Mishra

B.Sc., St. Xavier's College, Mumbai, India, 2014

M.Sc., University of Hyderabad, India, 2017

A Dissertation
Submitted in Partial Fulfillment of the
Requirements for the Degree of
Doctor of Philosophy
at the
University of Connecticut

2024

Doctor of Philosophy Dissertation

Photo-induced ultrafast dynamics and non-linear processes in molecules

Presented by

Debadarshini Mishra, B.Sc, M.Sc.

Approved by

Major Advisor: Nora Berrah

Associate Advisor: Carlos A. Trallero-Herrero

Associate Advisor: George N. Gibson

University of Connecticut

2024

Acknowledgements

... Acknowledgements

Contents

List of Figures

List of Tables

Chapter 1

Introduction

One of the central ideas of ultrafast molecular dynamics is the concept of a "molecular movie" – a series of time-resolved images that reveal the step-by-step dynamics of chemical reactions at atomic resolution [1–3]. This concept, pioneered by Ahmed H. Zewail and featured in his Nobel Prize-winning work [1], captures the transient nature of bond formation and fragmentation during chemical reactions. Measuring and understanding these ultrafast dynamics allows for the precise control of chemical reactions using ultrashort laser pulses, ultimately influencing the outcome of the reactions [4–6].

The advent of ultrafast laser technology has revolutionized scientific research and applications, making it possible to observe and manipulate chemical reactions at their inherent time scales. Intense laser pulses can now generate electric forces comparable to the Coulomb forces within molecules, thereby driving electron motion and transitions. These pulses can also achieve pulse durations down to a few femtoseconds and even attoseconds, enabling for detailed visualization of electron and nuclear dynamics. By using state-of-the-art light sources, such as intense ultrafast tabletop lasers and free-electron lasers (FELs) in combination with various time-resolved experimental techniques, we can obtain a comprehensive understanding of molecular dynamics.

Each time-resolved experimental approach has distinct advantages and limitations. For instance, ultrafast electron diffraction [7–11] provides real-time structural information of photoexcited molecules but struggles with sub-100 fs time-resolution due to electron repulsion in short pulses. In contrast, ultrafast X-ray diffraction [12–14] does not suffer from this issue, but requires a high photon flux from sources like FELs due to much lower scattering cross sections. Spectroscopy techniques such as transient absorption [15–17], involving detection of photons, can achieve high time resolution with a relatively compact setup but require detailed theoretical simulations of potential energy surfaces for correct interpretation of experimental results. Time-resolved ionization spectroscopy [18–24], based on detection of final ions and electrons, sometimes in coincidence with each other, can provide a kinematically complete picture of the induced photo-dynamics. While ions provide information about nuclear motion, electrons provide a more differential measurement of binding energies and chemical environments by measuring chemical shifts [25, 26].

Molecules can be excited and ionized using various methods, each providing insights into different regimes. With X-rays, we gain element and site-specific information on inner-shell ionization and electron correlation [27–30]. Using VUV or UV photons, we can study excited state dynamics or ionization processes through single-photon interactions [31–33]. Meanwhile, IR lasers generate intense fields that can directly influence molecular potentials and facilitate the ionization of outer valence electrons [34–38]. Ultrafast spectroscopy, in its various forms, aims to align experimental observations with theoretical models, enhancing our understanding of the complex interactions between electrons and nuclei that govern chemical transformations. A wide array of experimental methods allows for the real-time tracking of these dynamics. By integrating experimental observations with advanced computational models [39–42], it is possible to not only predict but also control reaction outcomes [4–6]. This marks a significant transition from merely observing to actively manipulating chemical reactions in research.

1.1 Outline

My dissertation work involved a wide range of research projects with the common theme of exploring photo-induced molecular dynamics at ultrafast timescales. The research work was carried out at both the Berrah ultrafast laser lab at the University of Connecticut (UConn) and at various FEL and synchrotron facilities. This thesis presents a subset of those studies, focusing specifically on the topics where I made particularly significant contributions. Chapter 2 provides an introductory discussion that covers the most significant topics and experimental techniques used, with particular emphasis on the COld Target Recoil Ion Momentum Spectrometer (COLTRIMS) technique, which is used in the Berrah lab at UConn. Chapter 3 presents results from table-top IR-IR pump-probe experiments used to investigate isomerization dynamics in small molecules, such as acetonitrile and propanol isomers. These experiments enabled the time-resolved investigation of single and double hydrogen migration in these molecules, as well as a comparison of the relative yields of various fragmentation mechanisms. Chapter 4 expands on the use of the coincidence Coulomb explosion imaging technique in combination with COLTRIMS to study neutral fragmentation processes, specifically roaming reactions. This chapter discusses how the use of these techniques provides a clear and direct experimental signature of roaming fragments in molecular reactions. Chapter 5 explores the relaxation and fragmentation dynamics of C_{60}, a larger, more complex molecular system, using intense, ultrashort FEL pulses in a single-color XUV-pump XUV-probe setup, paired with a COLTRIMS. Chapter 6 examines the use of ultrafast electron diffraction technique to structurally resolve the molecular dynamics of 2-Bromothiophene, a ring molecule, as a function of two different UV excitation wavelengths. This method allows insights into how the branching ratio between two competing processes – ring-opening and bond dissociation – changes as a function of UV excitation wavelength. Finally, Chapter 7 offers a summary and outlook on all the studies presented in this thesis.

1.2 Publications

My research experience graduate school in the Berrah group has resulted in the following publications:

Published

1. **D. Mishra**, J. Reino-González, R. Obaid, A. C. LaForge, S. Díaz-Tendero, F. Martín , and N. Berrah, "Ultrafast molecular dynamics in ionized 1-and 2-propanol: from simple fragmentation to complex isomerization and roaming mechanisms", *Phys. Chem. Chem. Phys.* 24, 433 (2022)

2. A. C. LaForge*, S.K. Son*, **D. Mishra**, M. Ilchen, S. Duncanson, E. Eronen, E. Kukk, S. Wirok-Stoletow, D. Kolbasova, P. Walter, R. Boll, A. De Fanis, M. Meyer, Y. Ovcharenko, D. E. Rivas, P. Schmidt, S. Usenko, R. Santra, and N. Berrah, "Resonance-enhanced multiphoton ionization in the x-ray regime", *Phys. Rev. Lett.* 127, 213202 (2021)

3. M. McDonnell, A. C. LaForge, J. Reino-González, M. Disla, N. G. Kling, **D. Mishra**, R. Obaid, M. Sundberg, V. Svoboda, S. Díaz-Tendero, F. Martín, and N. Berrah, "Ultrafast laser-induced isomerization dynamics in acetonitrile", *J. Phys. Chem. Lett.* 11, 6724 (2020)

4. A. C. LaForge, J. D. Asmussen, B. Bastian, M. Bonanomi, C. Callegari, S. De, M. Di Fraia, L. Gorman, S. Hartweg, S. R. Krishnan, M. F. Kling, **D. Mishra**, S. Mandal, A. Ngai, N. Pal, O. Plekan, K. C. Prince, P. Rosenberger, E. Aguirre Serrata, F. Stienkemeier, N. Berrah, and M. Mudrich, "Relaxation dynamics in excited helium nanodroplets probed with high resolution, time-resolved photoelectron spectroscopy", *Phys. Chem. Chem. Phys.*, 24, 28844 (2022)

5. A. R. Abid, S. Bhattacharyya, A. S. Venkatachalam, S. Pathak, K. Chen, H. V. S. Lam, K.Borne, **D. Mishra**, R. C. Bilodeau, I. Dumitriu, N. Berrah, M. Patanen, and D. Rolles, "Hydrogen migration in inner-shell ionized halogenated cyclic hydrocarbons", *Sci. Rep.*, 13, 2107 (2023)

6. N. Breckwoldt, S. K. Son, T. Mazza, A. Rörig, R. Boll, M. Meyer, A. C. LaForge, **D. Mishra**, N. Berrah, and R. Santra, "Machine-learning calibration

of intense x-ray free-electron-laser pulses using Bayesian optimization", *Phys. Rev. Research* 5, 023114 (2023)

Under review

1. **D. Mishra***, A. C. LaForge*, L. M. Gorman, S. Díaz-Tendero, F. Martín, and N. Berrah, "Tracking an elusive molecular reaction: Time-resolved H_2 roaming in acetonitrile", *under review at Nat. Commun.*
2. A. C. LaForge*, **D. Mishra***, U. Saalmann, R. Obaid, S. Pathak, H. Lindenblatt, S. Meister, F. Trost, P. Rosenberger, R. Michiels, S. Biswas, K. Saraswathula, F. Stienkemeier, F. Calegari, M. Braune, M. Mudrich, M. F. Kling, D. Rolles, E. Kukk, T. Pfeifer, J. M. Rost, R. Moshammer, and N. Berrah, "Fragmentation dynamics of fullerenes upon extreme electronic excitation near the giant resonance with XUV free-electron laser pulses", *under review at Phys. Rev. Lett.*

In preparation

1. **D. Mishra***, A. C. LaForge*, J. P. Nunes*, D. Lahana, N. H. List, D. Hait,A. S. P. Paz, S. Bhattacharyya, K. Borne, E. G. Champenois, X. Cheng, R. Forbes, M. C. Hoffmann, E. Kukk, M. F. Lin, S. Pathak, X. Shen, A. S. Venkatachalam, M. Ware, J. Yang, D. Rolles, M. Centurion, T. J. A. Wolf, T. J. Martinez, and N. Berrah, "Structural imaging of the wavelength-dependent competition between ring-opening and dissociation in cyclic molecules", *In preparation*

* denotes equal contribution

Chapter 2

Experimental Methods and Techniques

2.1 Strong-field ionization

Photoionization is a fundamental process that occurs when an atom or molecule interacts with electromagnetic radiation, leading to the ejection of one or more electrons. This ejection can result from the absorption of a single photon with sufficient energy, or from the absorption of multiple photons. The cross-section of photoionization quantifies the probability of an ionization event as a function of the photon energy, and plays a critical role in understanding how light interacts with matter. This process is pivotal in the study of atomic and molecular physics, offering deep insights into the electronic structure of atoms and molecules, as well as the dynamics of their ionization processes. When photoionization occurs in a molecule, it can lead to the fragmentation of the molecule into several smaller ions and/or neutrals. These fragments carry information about the dynamics the molecule undergoes upon photoexcitation. Advanced experimental techniques, such as photoelectron spectroscopy, pump-probe measurements, coincidence imaging, and Coulomb explosion imaging, enable the mapping of temporal and energy-related dynamics underlying atomic and molecular photoionization.

Photoelectric effect describes the phenomenon where an atom or molecule ejects an electron after absorbing a photon whose energy $h\nu$ (where ν is the frequency of light and h is Planck's constant) exceeds the ionization potential, E_{IP}. E_{IP} is the minimum energy required to remove an electron from the system in the ground state. If the photon energy is higher than E_{IP}, then the electron can be directly ionized into the continuum. On the other hand, if the photon energy is lower than

E_{IP}, it is still possible to remove the electron via multi-photon or tunnel ionization, provided the intensity of light is sufficiently high.

The response of an atom or molecule to a strong laser field depends on the intensity and the wavelength of the field. This interaction can be quantitatively analyzed using the Keldysh parameter, γ, a dimensionless quantity which can be defined as:

$$\gamma = \sqrt{\frac{E_{IP}}{2U_P}} \tag{2.1}$$

$$U_P = \frac{I}{4\omega^2}(\text{in atomic units}) \tag{2.2}$$

where U_P is the ponderomotive potential and I is the laser intensity. The ponderomotive energy is the cycle-averaged kinetic energy that an electron acquires while oscillating within the laser's electromagnetic field. The Keldysh parameter, γ, plays a crucial role in distinguishing between multiphoton ionization and tunneling ionization regimes by comparing the strength of the electric field that an electron experiences within an atom or molecule to that of the laser field.

When $\gamma << 1$, it signifies that the interaction belongs to the tunneling ionization regime. In this case, the intensity of the laser field is so high that it significantly distorts the potential barrier that confines the electron within the atom or molecule. This, in turn, enables the electron to tunnel through the barrier, even if the photon energy is less than the system's ionization potential.

Conversely, $\gamma >> 1$ indicates that the ionization process is dominated by the absorption of multiple photons (multiphoton ionization). The multiphoton ionization regime occurs when the electric field strength of the laser light is not sufficient to significantly distort the potential barrier. Instead, ionization occurs through the absorption of multiple photons, each contributing a quantized amount of energy that, in sum, provides the electron sufficient energy to overcome the ionization potential. An illustration of both multiphoton ionization and tunnel ionization regimes is given in Fig. 2.1.

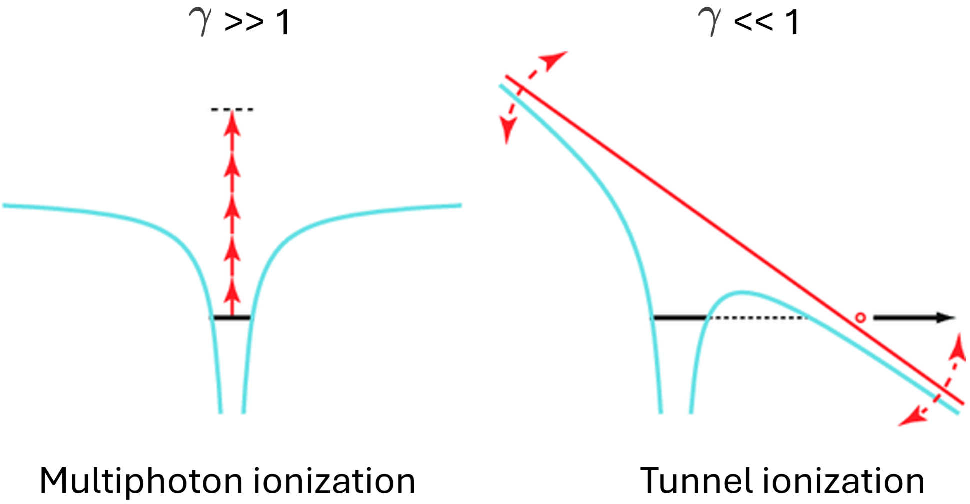

Figure 2.1: Strong-field ionization regimes: multiphoton ionization and tunneling ionization. Adapted from [43].

Typically, strong-field ionization occurs when atoms and molecules interact with a focused laser beam. For instance, using a focused beam from a Ti:sapphire laser with a wavelength, λ, of $\approx$ 800 nm, we typically can achieve intensities at the focal point ranging from $\sim 10^{13}$ to 10^{15} W/cm^2. The lab-based experiments described in this thesis using 800 nm laser pulses typically operate at a high laser intensity of around 10^{14} W/cm^2. To compute the ponderomotive potential that an electron would experience with these parameters, we can reformulate equation 2.2 as a function of laser wavelength and intensity and in units of eV as:

$$U_P[eV] = 9.34 \times 10^{-20} \times (\lambda[nm])^2 I[W/cm^2] \tag{2.3}$$

Using the typical values of laser intensity (5×10^{14} W/cm^2) and wavelength (800 nm), we calculate the U_P to be approximately 29.89 eV. For a small molecule like acetonitrile, CH_3CN, the E_{IP} is 12.2 eV [44]. Hence the Keldysh parameter, γ, in this case is 0.45. This implies that the ionization mechanism is in the tunneling ionization regime. However, it is important to note that not all molecules are exposed to the peak intensity of the focus. In fact, the data contains contributions from multiphoton ionization as well, due to focal averaging over different intensity regions in the focal plane and along the beam direction [45].

2.2 Ultrafast lasers

This section gives a brief introduction to the femtosecond laser system that was used to conduct the lab-based strong-field ionization experiments described in Chapters 3 and 4 of this thesis.

Our experiments are performed using a state-of-the-art Ti:sapphire ultrafast laser system from Coherent. This laser system generates linearly polarized (horizontal) pulses with average energy of 1 mJ at a central wavelength of 790 nm, with 35 fs pulse duration. The high repetition rate of the laser system (used at 5kHz and 10kHz for our experiments) is optimal for coincidence imaging of multiple charged fragments from a single ionization event. The two main components of the ultrafast laser system are the oscillator and the amplifier which are briefly discussed below.

The Coherent Vitara is a Ti:sapphire laser oscillator system that can generate modelocked pulses at 80MHz repetition rate. The Ti:sapphire crystal of the oscillator is pumped with a continuous wave 532 nm optically pumped semiconductor laser. A typical output pulse from the oscillator has a pulse duration of 13 fs, average power of ∼400 mW, and a central wavelength of 790 nm with 70 nm bandwidth. The output of the oscillator is used to seed the Ti:sapphire amplifier.

The Coherent Legend Elite is a regenerative amplifier based on the chirped-pulse amplification (CPA) technique [46]. Initially, the laser pulses from the oscillator are stretched in time from femtosecond to picosecond duration using grating stretcher to decrease peak intensity, which helps avoid damage to the amplifier crystal. A small subset of these stretched pulses are then selected by Pockel cells, which act as fast voltage-controlled optical switches. By choosing a subset of pulses from the oscillator, the repetition rate is reduced from 80 MHz to 10kHz or 5kHz for our experiments. The pulses are then amplified via multiple passes through the

Ti:sapphire crystal which is the gain medium. The gain medium is pumped by a diode-pumped, frequency-doubled Nd:YLF laser that generates Q-switched pulses at 527 nm. After achieving the desired amplification, the polarization of the Pockel cell is switched back to eject the amplified pulse from the cavity. These pulses are then split into two arms using a 70:30 beam-splitter, setting the stage for pump-probe spectroscopy. The pulses in each arm are then independently compressed in time using a grating compressor. This setup therefore allows us to independently control the pulse duration of each arm.

2.3 COLTRIMS

COLTRIMS is an acronym for COLd Target Recoil-Ion Momentum Spectroscopy. This technique was developed in the late 1980s and gives us access to kinematically complete experiments on atomic and molecular fragmentation processes [47, 48]. This is achieved by the coincident and momentum-resolved detection of fragment ions and electrons upon photoexcitation. Fig. 2.2 shows the standard setup of the COLTRIMS apparatus. The set-up detects both the time-of-flight (TOF) and the 2D impact position of the charged particles and the detection scheme is described in more details below. With the TOF and 2D position information, we can reconstruct the initial 3D momentum vectors of each of the detected charged fragments. The target, the molecule or atom of interest, is studied in the gas phase, which enables us to explore complex dynamics in single molecules. With the coincident momentum information of the detected fragments, we can apply momentum conservation principle to get a complete picture of a reaction process [48].

The COLTRIMS technique has been used to study a wide variety of physical phenomena such as Compton scattering [49], ionization of atoms and molecules [50], dissociation dynamics [21–24, 51], photon momentum analysis [52], to name a few, using several types of ionizing sources with energies ranging from a few eV (near infrared) to several keV (hard X-rays) such as tabletop lasers, free-electron lasers and synchrotron radiation [21–23, 53–58], with unprecedented precision and reliability.

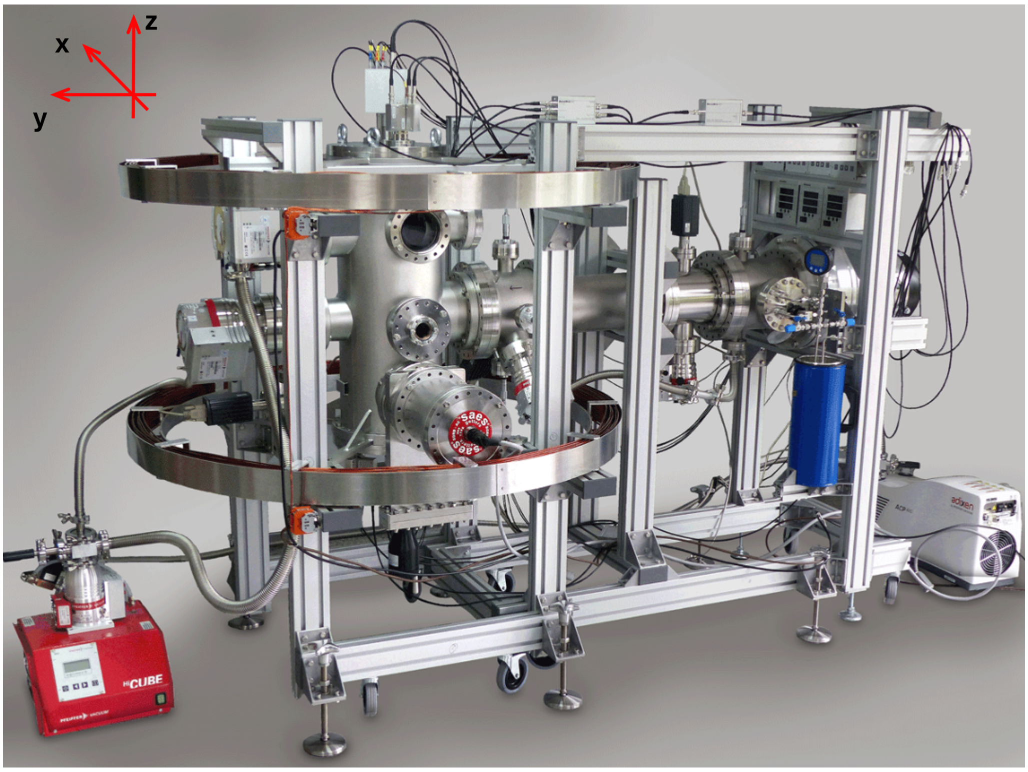

Figure 2.2: COLTRIMS setup showing the main chamber with the spectrometer and electronics. The gas jet enters the interaction region along the $y-$ axis, the laser beam enters the chamber through a window along the $x-$ axis, and the spectrometer is fixed along the $z-$ axis. Figure is adapted from [59]

The target molecules are introduced into the interaction region inside the spectrometer chamber (along the $y-$axis in Fig. 2.2) by expanding the gas through a 30 μm diameter nozzle, which is connected to a gas bottle or a liquid sample reservoir. The jet then passes through a skimmer, a reversed funnel made of copper with a very small aperture, and four-jaw slits in order to remove turbulent peripheral areas of the molecular beam. The molecular jet then enters the interaction region where the laser pulses (along the $x-$ axis in Fig. 2.2) can interact with the perpendicular molecular beam. The laser pulses are focused back into the interaction region by a concave mirror of 75 mm focal length to a spot size of $\sim$ 10 μm in diameter.

The main chamber of COLTRIMS is kept under ultra-high vacuum ($\sim 10^{-10}$ mbar) using several turbo-molecular pumps in order to reduce the signal-to-noise ratio of the detected signal from the residual background gases. The spectrometer itself is located in the main chamber along the $z-$ axis (see Fig. 2.2 for reference) and generates a tunable electric field through a stack of copper plates connected via resistors. The spectrometer has an acceleration region with constant electric field where the particles separate according to their velocity after which it has a drift region with zero electric field which allows the particles to spread out in space for better detection. The charged particles formed at the interaction region are guided by the electric fields to a z-stack 80 mm diameter microchannel plate (MCP) detector with a delay line (hex) anode. The detectors are triggered by the same timing array that triggers the Pockel cell driver of the laser system. The signals from the MCP and the hex delay line anodes are usually very small (few mV) and are amplified using a commercial fast amplifier. Next, in order to determine the precise arrival time of the different signals with respect to the trigger signal from the laser, a constant fraction discriminator (CFD) is used. CFD can accurately determine the timing of the signals independent of the signal height and works efficiently even when multiple signals arrive close together. These processed signals are fed into a time-to-digital converter (TDC). TDC converts the time interval between the detection of the event and the reference timing signal into a digital output, which is then saved for further analysis. The final data consists of the TOF and 2D position information of all the charged particles detected for a particular trigger.

2.4 Data analysis

Fig. 2.3 shows the TOF spectrum that is generated following IR (800 nm) pump-probe ionization of deuterated acetonitrile, CD_3CN. An ion's mass-to-charge ratio, m/q, is determined by its time of flight measurement. Ions are accelerated by an electric field of known strength in COLTRIMS. The velocity of the ion depends on their m/q; heavier ions with the same charge have lower velocities, while ions with

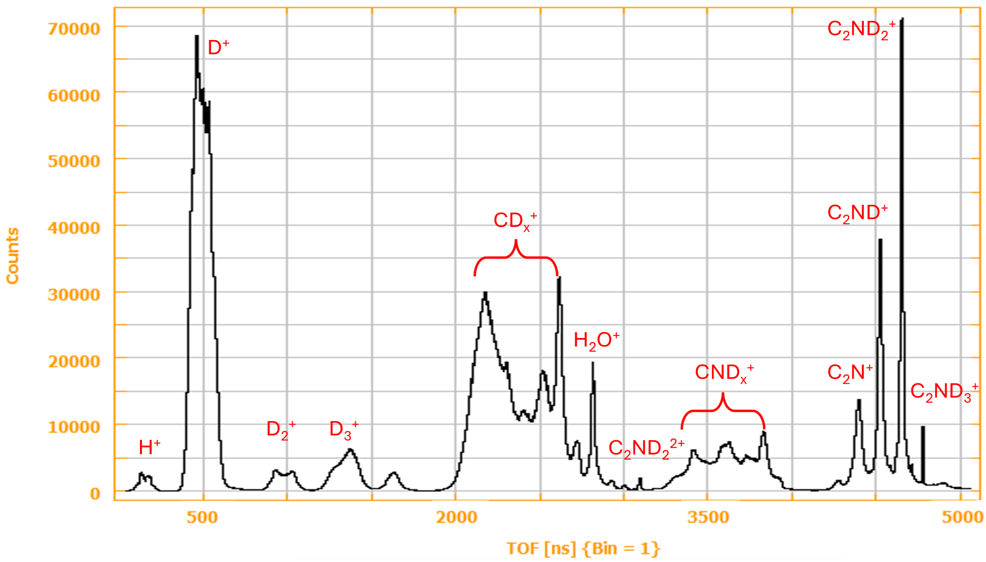

Figure 2.3: Time-of-flight spectrum of deuterated acetonitrile (CD_3CN) following pump-probe excitation.

higher charges have greater velocities. As a result, the TOF of each ion will depend on its velocity, and therefore is a measure of its m/q, with which we can identify the ion. There is a linear relation between the TOF of an ion and its m/q, given by:

$$TOF = k\sqrt{\frac{m}{q}} \tag{2.4}$$

From the TOF and 2D position signals, we can reconstruct the full 3D momenta of ions that are formed and detected from each laser trigger event. This technique is known as the photoion-photoion coincidence (PIPICO) spectroscopy. In order to determine the various two- and three-body fragmentation pathways formed from the photoionization of the parent molecule, PIPICO or photoion-photoion-photoion coincidence (PIPIPICO), also called TRIPICO, maps are often used. Fig. 2.4 shows the PIPICO map from IR pump-probe ionization of deuterated acetonitrile. The $x-$ and $y-$ axes of the plot represent the TOF of the first and second ions detected together in each trigger event. Typically, the PIPICO map helps to identify all complete pairs of ions, such that the masses of the ion pair sum up to that of the parent ion mass. These complete channels allow for the implementation of momentum conservation and appear as narrow distributions with a slope of -1 [60].

Conversely, the incomplete channels, where the masses of the fragment do not add up to that of the parent ion and hence do not conserve momentum, appear on the PIPICO map as channels with much broader distributions or with different slopes [60]. The inset figures in Fig. 2.4 identify the bonds that fragment, leading to the observation of the final channels.

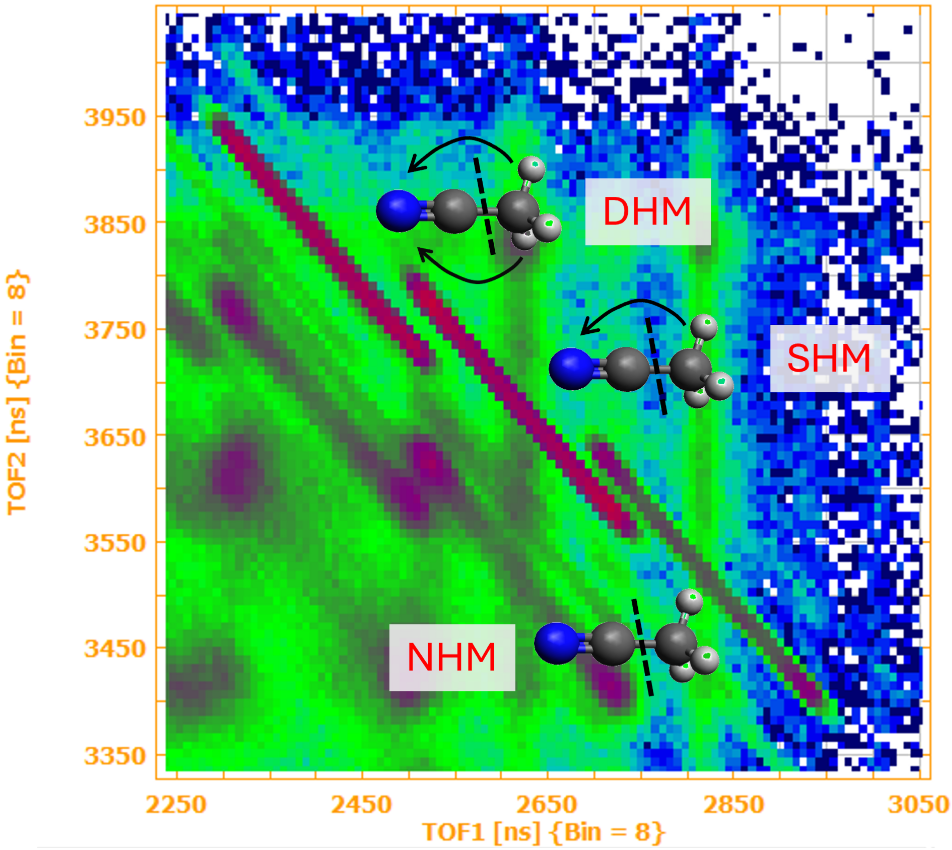

Figure 2.4: Photoion-photoion map of deuterated acetonitrile following pump-probe ionization. The inset figures show the bond fragmentation and the migration of D atoms that occurs to give rise to the observed complete coincidence channels. The three channels in this plot show no-hydrogen migration (NHM), single-hydrogen migration (SHM), and double hydrogen migration (DHM).

We can use the TOF ranges for each ion to isolate a particular coincidence channel. The 2D position for each ion allows us to compute the momentum components parallel to the detector. Since the field is uniform in the $z-$ direction, the parallel momentum components are calculated using: $P_x = m \times x/TOF$ and $P_y = m \times y/TOF$, where m is the mass of the ion, x and y are the ion hit positions on the detector, and TOF is the time-of-flight of the ions from the interaction region to the detector.

The calculation of the momentum component along the spectrometer axis, perpendicular to the detector, is slightly more complex. The acceleration of an ion in the applied electric field inside the COLTRIMS is given by $a = Eq/m$, where E is the uniform electric field. Using Newton's classical equations of motion involving uniform acceleration, initial velocity (v_{z0}), and the distance, S, from the interaction region to the detector, we can derive an expression for TOF [61]

$$TOF = -\frac{P_z}{qE} + \sqrt{\frac{2Sm}{qE}}\sqrt{1 + \frac{P_z^2}{2mSqE}} \tag{2.5}$$

From the equation above, P_z is found iteratively by calculating the root of the equation using Newton's method. Using the 3D momentum information of each ion, we can check for momentum conservation for a given fragmentation channel, and also compute kinetic energies of each of the ions.

2.5 Coulomb explosion imaging

One of the most efficient methods to study molecular dynamics and structural evolutions is a technique called Coulomb explosion imaging (CEI). With CEI, the goal is to highly ionize and strip away electrons from the molecular system, causing the multiply charged molecule to explode in smaller charged fragments. The explosion of the charged fragments results from the Coulombic repulsion among the positive charges. These charged fragments provide valuable insights into the geometry and dynamics of the original system. The key to CEI is the extremely rapid removal of many electrons to ensure that the molecule fragments into ions without undergoing any structural rearrangement during the charging up process. Originally, CEI was performed by sending beams of ionized molecules through thin foils [62], which would strip off electrons. Nowadays, CEI is triggered through photoionization using intense, femtosecond laser pulses. These short pulses not only ensure the fast removal of electrons but also enable time-resolved experiments [63–65]. CEI has been used to investigate ultrafast processes such as dissociation [66], vibration [67], isomerization reactions [27, 68] and charge transfer [69]. If the ionization process occurs on a timescale that is much smaller than that of nuclear motion – for instance, in a Coulomb explosion process initiated by inner-shell photoionization and fast Auger relaxation, or strong field ionization that takes place within a few femtoseconds – one can use the momenta of the fragment ions to extract geometrical information about the dissociating parent ion [24, 53].

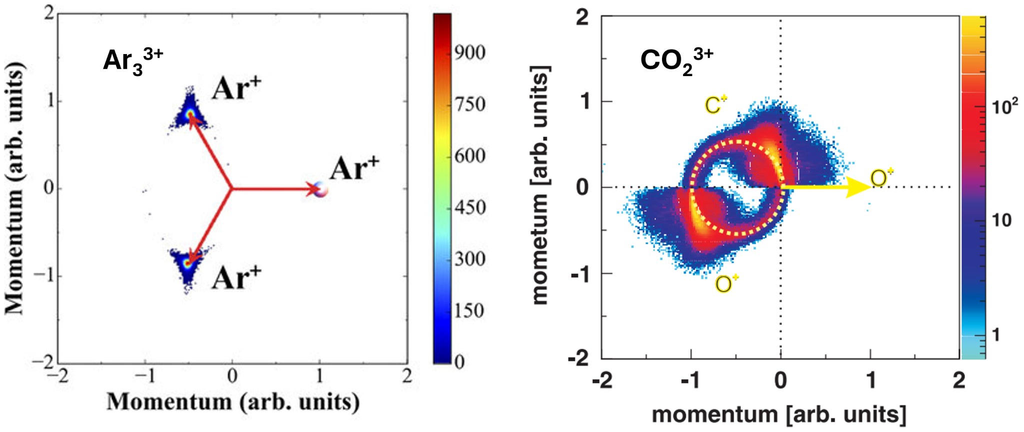

Figure 2.5: Newton plots showing direct, concerted fragmentation of Argon trimer, $Ar_3{}^{3+}$ (left panel, adapted from [70]), and sequential fragmentation of $CO_2{}^{3+}$ (right panel, adapted from [71]).

A Newton plot, or Newton diagram, provides an intuitive way to visualize the momentum correlations between coincident ionic fragments [70–72]. The Newton plot is a two-dimensional map in which the relative momenta of two of the fragments are plotted with respect to the momentum of the third fragment. In a three-body coincidence channel, the momentum of the one of the fragments is fixed along the $x-$ axis, and the momentum vectors of the other two ions are plotted, relative to the first, on the bottom and top halves of the plot. The plot is constrained to lie on a plane due to momentum conservation. If the three-body coincidence channel results from the simultaneous fragmentation of the molecule into three ions, we observe a localized distribution of the ion momentum vectors, as shown in the left panel of Fig. 2.5 [70]. However, if the three-body fragmentation occurs sequentially, such after the initial ejection of one ion, the remaining intermediate subsequently fragments into two ions, we expect to observe a semi-circular distribution. This is due to the fact that the intermediate fragment can rotate with respect to the first ion before fragmenting further, which gives rise to such a semicircular distribution shown below in the right panel of Fig. 2.5 [71].

Chapter 3

IR-induced isomerization in small molecules

3.1 Introduction

Isomers are molecules with identical chemical formulas but differing geometric structures and they play a pivotal role across a broad spectrum of biological and chemical processes [73–76]. For instance, human vision is facilitated by the cis-trans isomerization in rhodopsin, a light sensitive receptor protein, which plays a critical role by converting the chromophore 11-cis-retinal, bound within rhodopsin, to its all-trans form upon absorption of visible light [75, 77]. This isomerization process is fundamental to conversion of light energy into electrical signals that enable the brain to interpret visual information and occurs within 200 fs [78]. In general, isomerization is a universal phenomenon which is important to the fields of biochemistry and pharmacology, and has a wide variety of technological applications, specifically in the context of molecular motors, molecular switches, and re-writable optical memories [79, 80].

Laser-induced ionization of molecules can lead to changes in their molecular structures and, by extension, their chemical properties via different types of characteristic isomerization processes such as single and double hydrogen migration [21–23], rotation about a bond [51] and tautomerization [81]. In particular, hydrogen migration involves the ultrafast motion of one or more hydrogen atoms accompanied by a chemical bond rearrangement and is often observed in numerous systems, ranging from small hydrocarbons [82] and organic molecules [21] to large biomolecules like proteins and peptides [83]. The reported timescale for such fast nuclear dynamics varies from a few femtoseconds in acetylene [82] to several hundred femtoseconds in acetonitrile [22] and ethanol [21]. More generally, migration of other groups such as hydroxyl has been observed in ionized amino acids [84].

In this chapter, we study the time-resolved, photo-induced isomerization dynamics involving hydrogen migration in small molecules like acetonitrile and two structural isomers, 1- and 2-propanol using IR-pump-IR-probe spectroscopy in combination with coincident Coulomb explosion imaging (CEI). Additionally, we compare the isomerization dynamics previously studied in ethanol [21] with that observed in acetonitrile and the propanol isomers to understand the effect of increasing carbon chain length on hydrogen migration. We interpret our experimental results with the aid of quantum chemistry calculations performed by the group of Prof. Fernando Martín in Madrid, Spain.

3.2 Experimental methods

In order to understand the underlying molecular dynamics that govern such light-induced ultrafast processes, a systematic study is necessary. This can ideally be achieved by using coincident momentum imaging [85], which allows for a kinematically complete measurement of the fragments produced in ionized molecules. In combination with Coulomb explosion imaging (CEI) [86], this scheme has been used as a tool to identify isomers [**pathak2020˙JPCL**], to study the geometry of molecules [62] and even to map the presence of conical intersections [87]. In order to study the time-resolved CEI of the molecules in real time, a laser pump-probe scheme is implemented. The pump pulse initiates a molecular wave packet onto an excited electronic state whose propagation is interrogated by the probe pulse arriving at variable time delays. This intense probe pulse further ionizes the molecule to a highly charged state and thereby, induces a violent Coulomb explosion. The measured correlated momenta of the photoions provides information on the fragmentation and isomerization dynamics of the molecule on its excited electronic state. Pump-probe experiments have been successfully used to study rotational, vibrational and electronic dynamics in a wide variety of systems ranging from simple molecules to complex nanosystems and bulk solids [88].

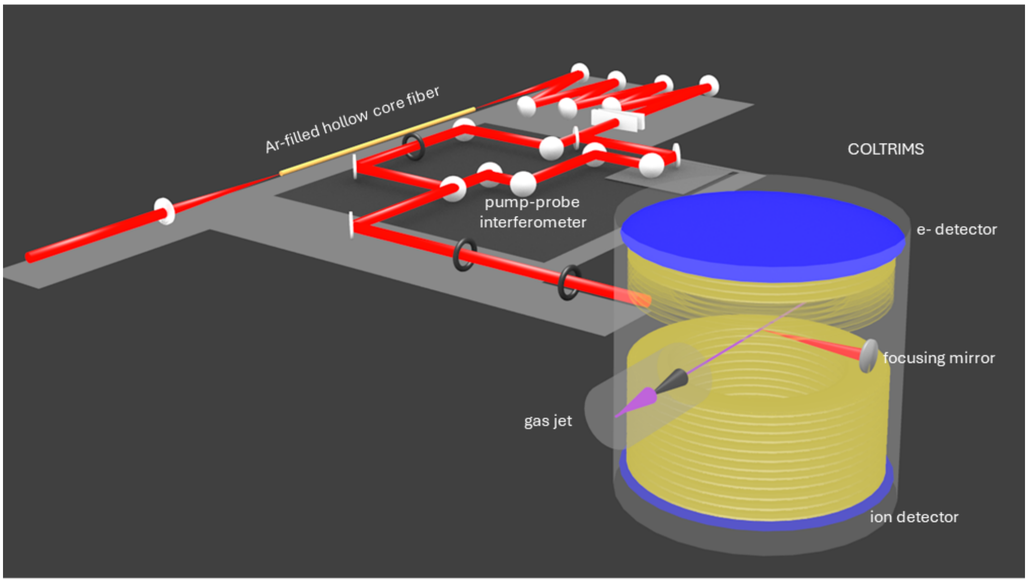

Figure 3.1: A schematic of the experimental pump-probe spectroscopy setup including the hollow-core fiber for spectral broadening of 790 nm pulse and the COLTRIMS. Adapted from [21].

The experimental setup is identical to the one described in a previous publication [21] and a schematic is shown in Fig. 3.1. Briefly, the 790 nm, 35 fs pulses generated from a Ti:Sapphire laser, with a repetition rate of 10 kHz, were focused into a hollow core fibre filled with Ar to generate 9 fs pulses with a central wavelength of 730 nm. These pulses were then split into pump and probe arms, where the probe arm is time-delayed with respect to the pump. Subsequently, the pulses were spatially overlapped and focused to a peak intensity of 2.3×10^{15} W/cm^2 and a spot size $\sim 11\ \mu$m inside the COLTRIMS [89], onto an orthogonally propagating molecular jet of the gas phase sample (1-propanol, 2-propanol). Upon ionization of the sample, the ionic fragments were directed to a position-sensitive detector using a static, homogeneous electric field. The three-dimensional momentum distributions of the charged fragments were then reconstructed using their time of arrival at the detector and their two-dimensional position information.

For acetonitrile, we used the same experimental setup as described above, but without the hollow core fiber which was used to to generate sub 10 fs pulses. The 35 fs, 790 nm pulses from the Ti:Sapphire laser were split equally into two arms for pump-probe spectroscopy, each with an intensity of 3×10^{14} W/cm^2.

3.3 Simulation methods

In general, ionization induced by a strong IR pump pulse, as is the case with the experiments described in this chapter, proceeds through both multi-photon absorption and tunneling, and their exact description is outside the scope of existing theoretical frameworks. As a result, determining the amount of excitation energy within the remaining molecular cation and the distribution of its electronic states – ground and excited – remains elusive. Therefore, following previous work [21, 84, 90–93], we will assume that, irrespective of the electronic excited states of the cation that are populated, their decay into the nuclear degrees of freedom associated with the ground electronic state, for instance through conical intersections, occurs within the initial few tens of fs. This behavior is typical for most molecular cations of a size comparable to propanol that have similar floppy structures. As a result, this theoretical description is best suited to describe the fragmentation dynamics that take place beyond ~100 fs.

Under these assumptions, our theory collaborators, Fernando Martín and Sergio Díaz-Tendero from Universidad Autónoma de Madrid, conducted *ab initio* molecular dynamics (AIMD) simulations starting with the Frank-Condon geometry, i.e., the optimized ground-state geometry of the neutral molecule, with a certain amount of internal energy randomly distributed among the nuclear degrees of freedom. The internal energies used for these simulations are 5, 10, and 15 eV for the different molecular systems. These energy values were chosen because (i) they are comparable to those found or estimated in other molecules ionized by strong IR fields with similar pulse energies, (ii) they were successfully used to describe a similar experiment with ethanol [21], and (iii) they represent the minimum amount of energy that the system must have for all fragmentation channels to appear within 1 ps (our propagation time).

Quantum chemistry calculations were carried out using the density functional theory (DFT), in particular the B3LYP functional [94, 95] in combination with the 6-31++G(d,p) basis set. This method was employed both in the exploration of the potential energy surface (PES) and in the AIMD simulations. In the PES exploration, critical points in the relevant pathways were located, thus allowing computation of the ionization potentials and dissociation energies for the relevant channels. AIMD simulations were carried out using the Atom-centered Density Matrix Propagation method (ADMP), [96–99] imposing a timestep of 0.1 fs and up to 1 ps. The dynamics are run in the electronic ground state for both cationic and dicationic states with 500 trajectories for each energy value and charge state. All the simulations have been carried out with the Gaussian16 program [100]. The combination of AIMD with PES exploration has been used with success in the past to study the fragmentation dynamics of ionized molecules of different nature [21, 84, 90, 91, 101, 102].

3.4 Hydrogen migration in acetonitrile

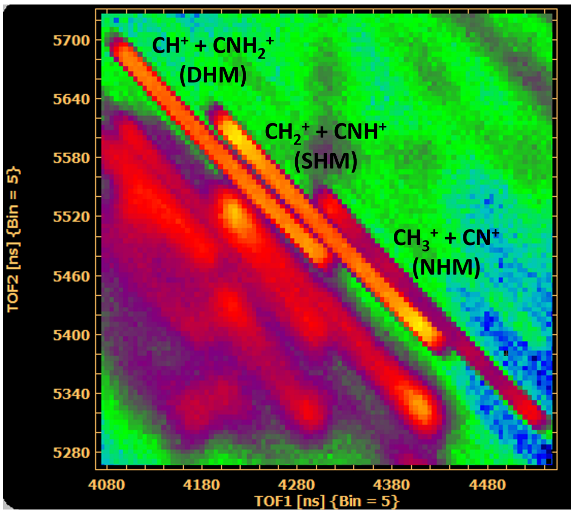

Figure 3.2: Photoion-photoion coincidence map of CH_3CN, identifying the C-C fragmentation and hydrogen migration channels.

Fig. 3.2 shows a portion of the photoion-photoion coincidence (PIPICO) time-of-flight spectrum of acetonitrile, CH_3CN. When a molecule breaks into just two fragments, the linear momenta imparted to these ionic fragments are exactly equal and opposite, leading to a narrow distribution characterized by a slope of -1. Channels that appear in PIPICO maps as broader distributions, whether with identical or varying slopes, typically result from neutral fragmentation or the incomplete detection of more complex fragmentation processes. The fragments constituting each coincidence channel are identifiable through the time-of-flight (tof) data at the center of these channels. The relevant complete channels in acetonitrile, where the fragment masses sum up to that of the parent molecule, have been identified in Fig. 3.2. The formation of ${CH_3}^+$ + CN^+ through direct C-C bond cleavage indicates no hydrogen migration (NHM), while ${CH_2}^+$ + CNH^+ and CH^+ + ${CNH_2}^+$ result from single (SHM) and double hyrogen migration (DHM), respectively. The channel intensities give information regarding the efficiency and relative yields of these isomerization and fragmentation pathways, which are summarized in Table. 3.1. Notably, the channels associated with hydrogen migration are more prevalent than those from direct C-C bond fragmentation (NHM), highlighting the preference for bond-rearrangement processes over direct bond cleavage.

Channel	Relative yield	t_0 (fs)	τ (fs)
NHM	13.5%	230 ± 10	120 ± 20
SHM	47%	300 ± 20	270 ± 30
DHM	39.5%	500 ± 30	750 ± 160

Table 3.1: Relative yields, time shift, t_0, and exponential time constant, τ of the fragmentation and hydrogen migration channels of acetonitrile.

Using coincidence imaging with COLTRIMS gives us access to kinematically complete information for the observed process by allowing the reconstruction of the full 3D momentum vector information of each detected ionic fragment. This information can, in turn, be used to generate the kinetic energy release (KER), which is the sum of the kinetic energies of all the fragments involved in the fragmentation process. Fig. 3.3 shows the pump-probe delay-dependent KER for

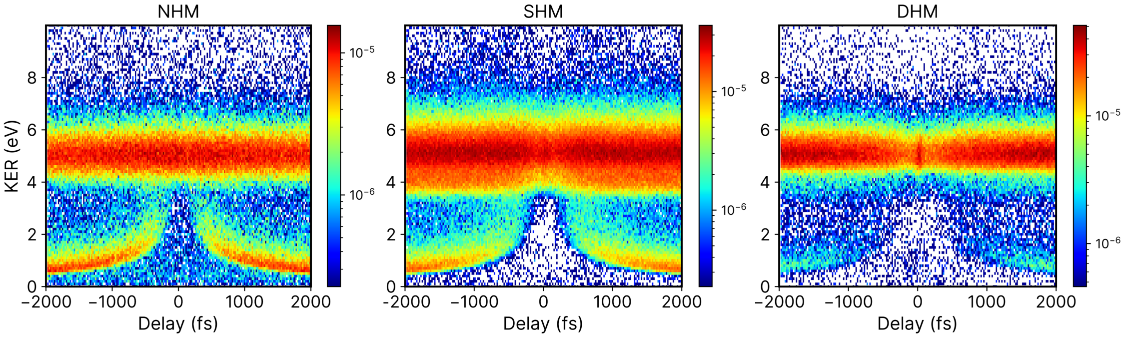

Figure 3.3: Kinetic energy release as a function of pump-probe delay for the no hydrogen migration (NHM), single hydrogen migration (SHM) and double hydrogen migration (DHM) channels of acetonitrile.

the NHM, SHM, and DHM channels. In this case, since the pump and probe pulses have nearly identical intensities, we observe similar dynamics at both positive and negative pump-probe delays.

The KER of each channel exhibits a broad, delay-independent feature centered around 5 eV. This feature occurs primarily due to a single pulse exciting the molecule to the dicationic state, which eventually fragments into the final observed products. Hence, this feature exhibits no time-dependence, since the second, time-delayed pulse plays no role in the formation of the channels.

However, there is a second, weaker distribution in the three channels, where the kinetic energy shows a strong dependence on pump-probe delay. With increasing pump-probe delays, there is a rapid decrease in KER due to the Coulomb repulsion between the ionic pair. In this case, the pump pulse excites the molecule to the cationic state and the dynamics occurring in the cationic state, such as molecular dissociation or isomerization, are probed by the second, probe pulse. The probe excites the molecule at various delays into the dicationic state, producing a dication which leads to final observed ion pair. Therefore, the measured KER at a given pump-probe delay provides an instantaneous picture of the dynamics induced by the pump pulse.

In order to extract the time constants of the underlying processes for the three channels, we fit the date with a saturating exponential of the form:

$$(1 - e^{-(\Delta t - t_0)/\tau}) \tag{3.1}$$

where Δt is the pump-probe delay, τ is the exponential time constant, and t_0 is the time shift from time zero. The values of τ and t_0 obtained from the fits are given in Table 3.1. While τ is attributed to the molecular fragmentation timescale, t_0 denotes isomerization time, which is explained in more details below, based on quantum chemistry simulations.

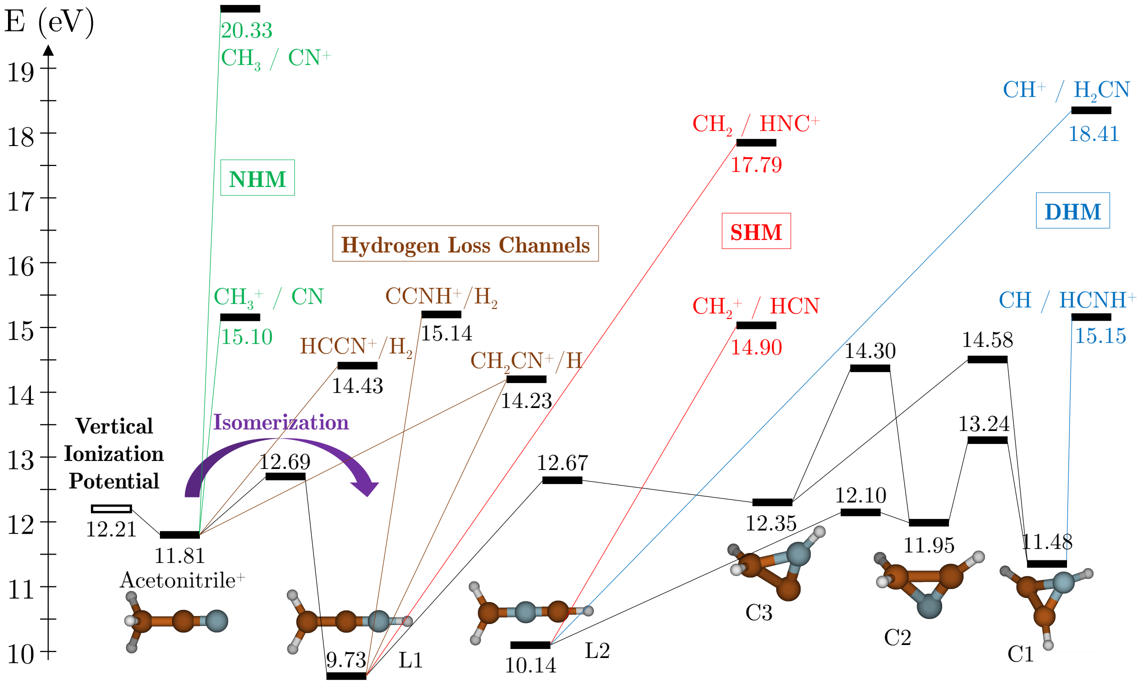

Figure 3.4: Critical points in the potential energy surface of singly charged acetonitrile computed at the B3LYP/6-31++G(d,p) level of theory. The open box corresponds to vertical ionization potential from the optimized neutral molecule. Optimized geometry of minima are shown together with the energy levels of the transition states that connect them. Relative energy values are referred to the neutral molecule and zero-point-energy corrected. The minima in the potential energy surface are Acetonitrile$^+$, linear structures L1, L2, and cyclic structures C1,C2 and C3. NHM, SHM and DHM stand for no-hydrogen migration, single-hydrogen migration and double-hydrogen migration respectively

Molecular dynamics simulations were performed for the singly- and doubly-charged acetonitrile molecule. From these simulations, we calculated the relative energies of only the most dominant fragmentation channels formed from singly-ionized acetonitrile, as well as of the transition states leading to those channels. This allows us to schematically represent the potential energy surface of the system, as shown in Fig. 3.4. The entrance channel is the vertical ionization from the neutral acetonitrile structure ($\sim$ 12 eV). In addition to the canonical form of acetonitrile, we identified five stable cationic conformers: two linear structures (L1 and L2 in Fig. 3.4) and three cyclic structures (C1, C2 and C3). Surprisingly, four of these isomers are more stable than the canonical form of CH_3CN^+. The isomer L1 is the most stable, and can be accessed through a small energy barrier of $\sim$0.5 eV above the entrance channel. The rest of the conformers are also energetically accessible, with barriers that are less than or equal to 2.5 eV above the entrance channel. The low barriers to isomerization in the potential energy surface coupled with the high stability of these structures explain why isomerization is the dominant process following ionization by the pump pulse.

The time shift values, t_0, obtained in the fit and presented in Table. 3.1, can be attributed to the isomerization processes shown in Fig. 3.4. If we consider a scenario where the ionization induced by the pump pulse brings the system into the entrance channel (indicated by the vertical ionization potential in Fig. 3.4), the excited singly-charged canonical form (CH_3CN^+) retains the excitation energy within its nuclear degrees of freedom. This allows it to undergo fragmentation after a delay ($t_0 \sim 200$ fs for NHM channel). However, there is a high likelihood for the molecule to undergo isomerization and get trapped into the potential well of L1, where it stays a longer time before fragmentation ($t_0 \sim 300$ fs for SHM channels). Further isomerization into more complex structures such as C1 or L2 leads to even longer delays before molecular cleavage ($t_0 \sim 700$ fs for DHM). Therefore, the sequential isomerization processes across subsequent potential wells account for the longer time shifts that we observe in the delay-dependent KER maps for each of the channels.

3.5 Fragmentation and isomerization dynamics in propanol

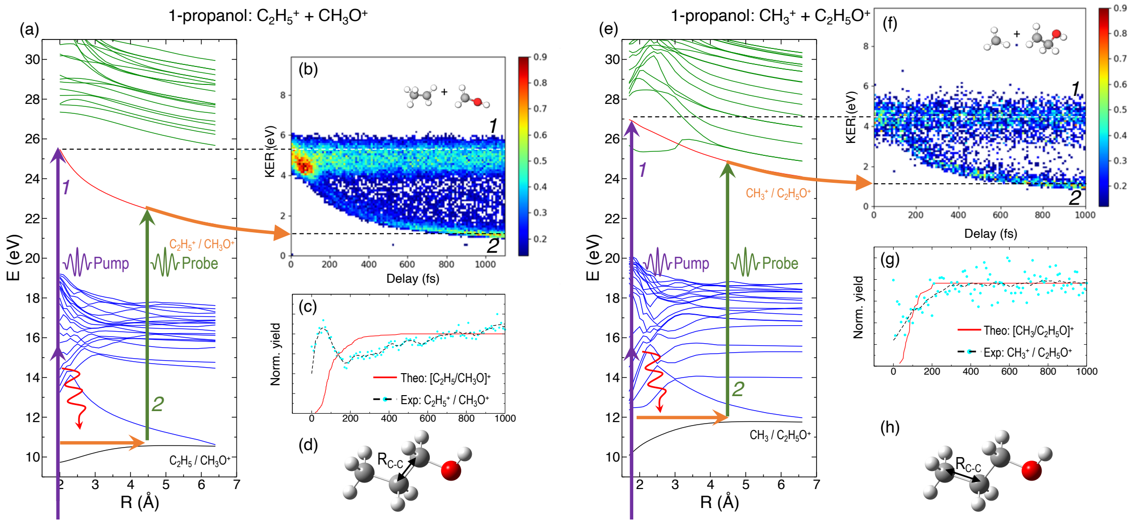

Figure 3.5: **(a)**, **(e)** Potential energy curves showing the ground and excited cationic and dicationic states of 1-propanol along the C$-$C bonds indicated in the ball-and-stick models shown in **(d)** and **(h)**, respectively. Purple arrows, representing multiphoton absorption induced by the pump pulse, indicate population of electronically excited states. Red curly arrows indicate relaxation to the ground state of the cation, with energy transfer to vibrational modes. Kinetic energy release as a function of the time delay between the pump and probe pulses for the double coincidence fragmentation channels **(b)** $C_2H_5^+$ + CH_2OH^+ and **(f)** CH_3^+ + $C_2H_4OH^+$ of 1-propanol. **(c)**, **(g)** Comparison between the projection of experimentally obtained dynamic KER signal intensities and theoretical yields using $E_{exc} = 10$ eV for the corresponding channels.

In general, the laser pump pulse can initiate various types of dynamics in a molecule which can result in the formation of different ionic fragments depending on the molecular geometry and its potential energy surfaces. Due to the position of the $-$OH group on one of the terminal carbon atoms in 1-propanol, $CH_3CH_2CH_2OH$ (see Fig. 3.5 (d)), cleavage of either of the two C$-$C bonds gives rise to two unique double-ion coincidence channels: $C_2H_5^+$ + CH_2OH^+ or CH_3^+ + $C_2H_4OH^+$. The experimentally obtained delay-dependent kinetic energy release (KER) of these two fragmentation channels are shown in Fig. 3.5 (b) and (f) and the corresponding potential energy diagrams, along the C$-$C bonds highlighted in (d) and (h), are shown in (a) and (e), respectively. The black and orange curves are the ground cationic and dicationic states, while the blue and green curves are the excited cationic and excited dicationic states, respectively. The potential energy curves explain the two types of distributions seen in the KER plots. The time-independent (static) distribution, indicated as ***1***, centered around ~ 5 eV in both Fig. 3.5 (b) and (f) is observed due to the direct promotion of the molecule to the dication state by the pump pulse. The time-dependent (dynamic) band, indicated by ***2***, shows a decrease in the KER as a function of pump-probe time delay. This band, which originates at 5 eV and reaches its asymptotic limit at ~ 1 eV, shows the dynamics that the molecule undergoes upon excitation to the ground or excited cationic states by the pump pulse. The probe pulse subsequently excites the molecule to the ground dicationic state which results in the typical Coulomb explosion (CE) behavior as the ionic fragments repel each other along the 1/R Coulomb potential curve. Fig. 3.5 (c) and (g) show the projection (cyan dots) of the dynamic band from the respective KER signal intensities (Fig. 3.5 (b) and (f)) onto the time delay axis. Additionally, the moving average of the projection signal is given by black dashed line. The fitting procedure for the extraction of solely the dynamic band from the KER plot is discussed in detail in Section 3.6 below. The theoretically obtained delay-dependent yield (red line) for the corresponding channels are plotted in the same figure. As can be seen, in general, there is qualitative agreement between theory and experiment, although, in some cases, theory predicts slightly faster fragmentation times compared to experiment. A possible explanation is that the excitation energy used in these calculations (10-15 eV) may be somewhat overestimated.

In contrast to 1-propanol, the central location of the $-$OH group results in the same photo-products upon cleavage of either of the two C$-$C bonds. Strictly speaking, for neutral 2-propanol, $CH_3CHOHCH_3$, the C$-$H bond (on the central carbon) breaks the symmetry and points towards one of the methyl groups. However, the energy required to move the central H atom from one side of the molecule to the other is much smaller than the amount of energy available in the system. Therefore,

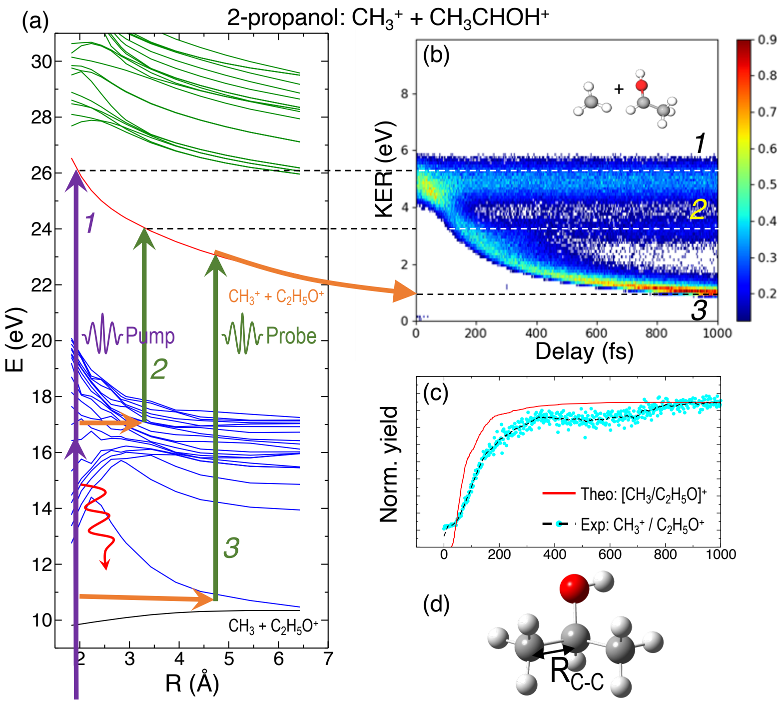

Figure 3.6: **(a)** Potential energy curves of the ground and excited cationic and dicationic states of 2-propanol along the C$-$C bond shown in the **(d)**. Purple arrows, representing multiphoton absorption induced by the pump pulse, indicate population of electronically excited states. Red curly arrows indicate relaxation to the ground state of the cation, with energy transfer to vibrational modes. **(b)** Delay-dependent KER for the fragmentation channel CH$_3^+$ + CHOHCH$_3^+$. **(c)** Comparison between the projection of experimentally obtained dynamic KER signal intensity and theoretical yield using E$_{\text{exc}}$ = 10 eV for the fragmentation channel.

the effect on the dynamics is expected to be negligible. Similar to Fig. 3.5, Fig. 3.6 (a) and (b) show the potential energy diagram and the delay-dependent KER for the fragmentation channel CH$_3^+$ + C$_2$H$_4$OH$^+$ of 2-propanol. Here, three distinct features are observed in the KER plot for this channel, marked as distributions ***1***, ***2*** and ***3*** in Fig. 3.6 (b). ***1*** and ***3*** are similar to the time-independent and -dependent features observed for 1-propanol (Fig. 3.5) and can be explained using the same mechanisms. ***2*** is indistinguishable from ***3*** up to 200 fs, after which it appears as a separate time-independent distribution centered around 3 eV. This KER distribution is unique to the fragmentation of 2-propanol and will be discussed in more detail in the next section. Additionally, for completeness, Tables 3.2 and 3.3 show a comparison between the calculated and measured relative yields for the two-body fragmentation channels shown in Figs. 3.5 and 3.6, respectively. These channels have been unambiguously identified in the coincidence maps and in the calculations. As can be seen, the agreement for the relative yields is reasonable for all initial internal energies considered in the calculations.

1-propanol	Experimental Yield	5 eV	10 eV	15 eV
$C_2H_5^+ + CH_3O^+$	93.77		82.68	80.69
$CH_3^+ + C_2H_4OH^+$	6.23		17.32	19.31

Table 3.2: Comparison between the calculated and measured relative branching ratios for the most dominant channels in 1-propanol.

2-propanol	Experimental Yield	5 eV	10 eV	15 eV
$CH_3^+ + C_2H_5O^+$	99.91	98.2	86.12	67.39
$H^+ + C_3H_7O^+$	0.09	1.7	13.88	32.61

Table 3.3: Comparison between the calculated and measured relative branching ratios for the most dominant channels in 2-propanol.

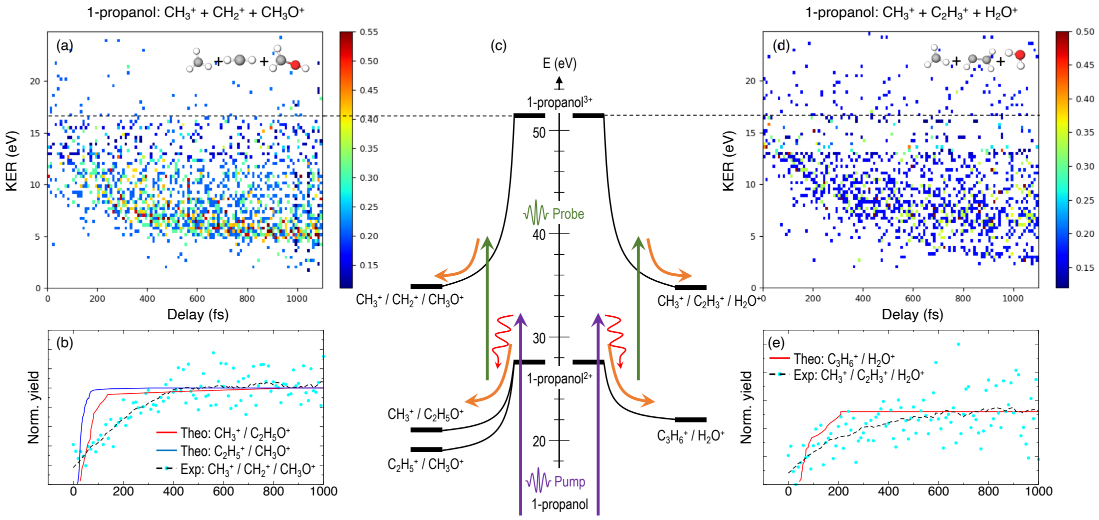

Figure 3.7: KER as a function of the time delay between the pump and probe pulses for the triple coincidence channels showing direct fragmentation, **(a)** CH_2^+ + CH_3^+ + CH_2OH^+, and single hydrogen migration **(d)** CH_3^+ + H_2O^+ + $C_2H_3^+$ in 1-propanol, respectively. **(c)** Schematic of the fragmentation and hydrogen migration dynamics evolving from doubly ionized 1-propanol. **(b)**, **(e)** Comparison between the experimentally obtained dynamic KER signal intensity along with the theoretical yields using E_{exc} = 10 eV for the two triple coincidence channels.

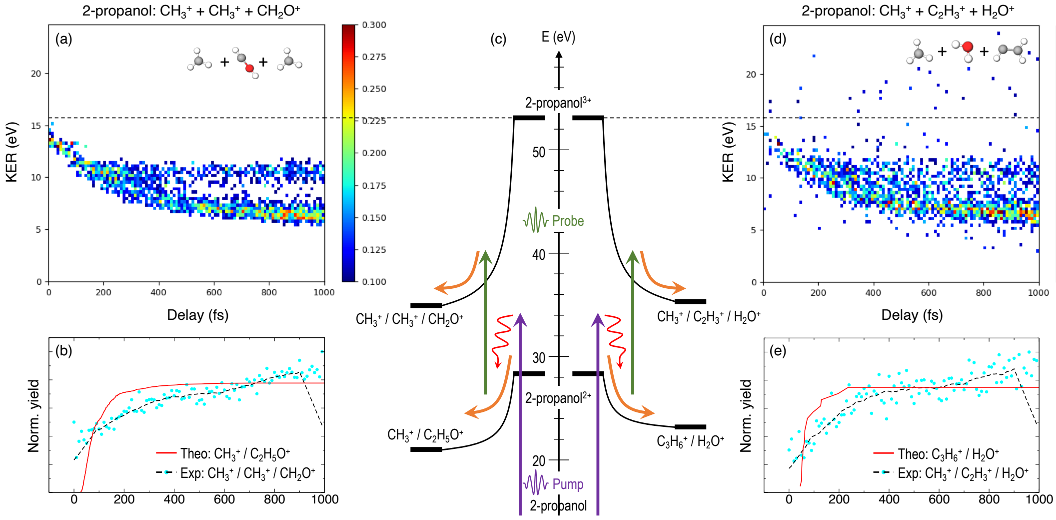

Figure 3.8: KER as a function of the time delay between the pump and probe pulses for the triple coincidence channels showing direct fragmentation, **(a)** CH_3^+ + CH_3^+ + $CHOH^+$, and single hydrogen migration **(d)** CH_3^+ + H_2O^+ + $C_2H_3^+$ in 2-propanol, respectively. **(c)** Schematic of the fragmentation and hydrogen migration dynamics evolving from doubly ionized 2-propanol. **(b)**, **(e)** Comparison between the experimentally obtained dynamic KER signal intensity along with the theoretical yields using $E_{exc} = 10$ eV for the two triple coincidence channels.

Furthermore, triple ionization of the molecule by the pump and probe pulses can result in three-body breakup channels which may reveal new fragmentation mechanisms induced in the molecule or may shed more light on subsequent fragmentation of the previously observed two-body channels. Figs. 3.7 and 3.8 show the delay-dependent KER plots for the observed triple coincidence channels for 1- and 2-propanol along with their potential energy diagrams. In this case, both the isomers show similar dynamics, each undergoing either fragmentation or hydrogen migration. Direct breakup of both C$-$C bonds in 1-propanol gives rise to the fragmentation channel CH_2^+ + CH_3^+ + CH_3O^+. Similarly, in 2-propanol, both C$-$C bonds fragment giving rise to CH_3^+ + CH_3^+ + CH_2O^+. Besides fragmentation, there is evidence of single hydrogen migration (SHM) in the three body channels. H_2O^+ is detected in coincidence with the CH_3^+ and $C_2H_3^+$ ions, thereby forming kinematically complete channels in both 1- and 2-propanol. However, the low yield of the SHM channels compared to the three-body fragmentations indicates that hydrogen migration is not very probable in both propanol isomers.

3.6 Discussion

To understand the time dependence of the measured KER spectra, we focus on the double-coincidence spectrum shown in Fig. 3.6. The experimentally measured KER results from two contributions: (i) the nuclear dynamics occurring in the singly-charged molecule in between the pump and the probe steps, and (ii) the nuclear dynamics occurring in the doubly-charged molecule after the probe step. Our AIMD simulations only give access to the dynamics associated with (i). In order to make a full comparison to the experimental KER, one should, in principle, include the effect of the probe pulse, which is not possible due to the computational demand. One can, however, estimate the KER associated with (ii) by using a sudden approximation, i.e., by assuming a perfect projection of the molecular geometry on the potential energy surface of the doubly charged molecule. In this approximation, the KER acquired after the probing step is approximately given by 1/R, where R is the C−C distance between the two separating fragments at a given time. Fig. 3.9 (b) shows the calculated KER as a function of the pump-probe delay for some of the trajectories associated with the CH_3^+ + $C_2H_5O^+$ channel resulting from the fragmentation and subsequent probing of singly-ionized 2-propanol. As the estimations of both components of the measured KER are only meaningful when the C−C bond distance stretches significantly, the figure does not include the results of those trajectories associated with roaming or other dissociation mechanisms. The temporal evolution of the KER for all trajectories is quantitatively very similar to that obtained in the experiment (see Fig. 3.6 (b)). Furthermore, Fig. 3.9 (a) shows a typical trajectory in which Coulomb explosion of the doubly-charged molecule makes the dominant contribution to the KER. KER contributions from before and after the interaction with the probe pulse (Coulomb explosion) become comparable only at about 1 ps (of the order of 0.5 eV).

In Fig. 3.6 (b), distribution ***2*** is a unique feature since it neither follows the asymptotic behavior of distribution ***3*** (Coulomb repulsion) nor the time-independent

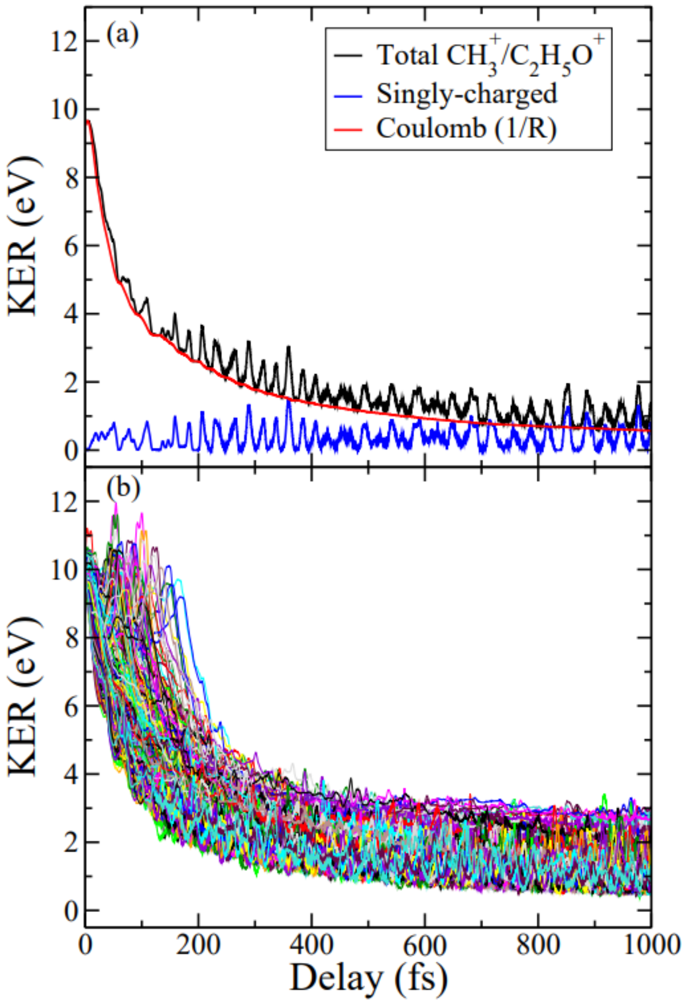

Figure 3.9: **(a)** Decomposition of the measured CH_3^+ + $C_2H_5O^+$ KER (black line) into the KER gained by the two fragments in the singly-charged 2-propanol molecule, i.e., before the probe step (blue line), and the KER resulting from Coulomb explosion after the probe step (red line). **(b)** Calculated KER as a function of the pump-probe delay for some trajectories associated with the CH_3^+ + $C_2H_5O^+$ channel of 2-propanol.

nature of distribution ***1***. A possible explanation is that this distribution is the result of the pump-excited molecular wave packet evolving along the excited cationic states which have very strong bonding character below 3 Å (Fig. 3.6 (a)). Consequently, for small time delays, there is a decrease in the KER as the C−C bond elongates but at larger delays, this bond cannot get stretched beyond 3 Å. Due to this, the probe pulse populates the same point in the dicationic surface resulting in no change in the KER value after ∼ 200 fs. Despite the potential energy curves for both 1- and 2-propanol cations being identical along the $H_3C{-}C_2H_5O$ bond distance, distribution

2 is not observed in the KER spectrum associated with double coincidences in 1-propanol. This could be due to the lower statistics available for 1-propanol, but the difference in atomic configurations of the two isomers is a more likely explanation.

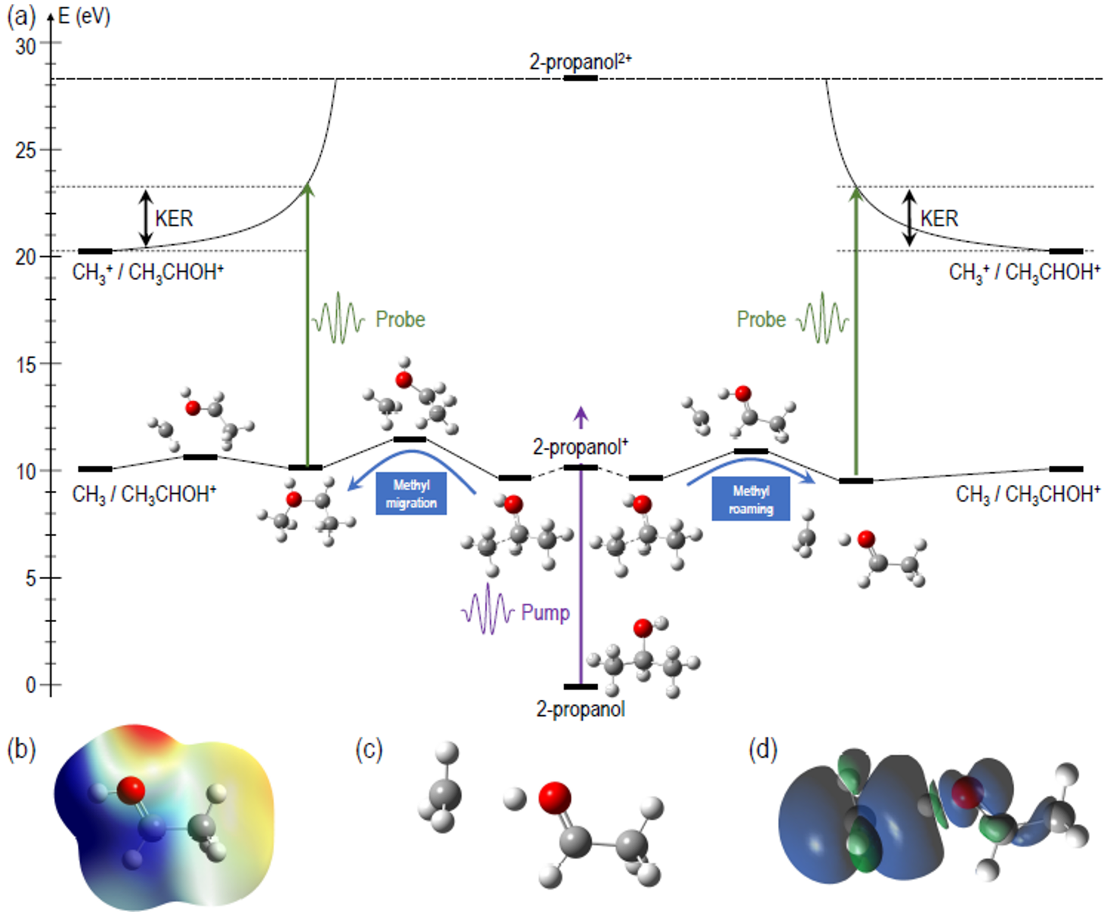

Figure 3.10: (a) Critical points in the potential energy surface of singly ionized 2-propanol showing isomerization of the methyl group. Pathway to the left involves cleavage of the C−C bond and formation of a new C−O bond. Methyl migration is stable in the new structure. Pathway to the right shows methyl roaming leading to the formation of a hydrogen bonded structure. CH_3 is subsequently released in both the pathways. Relative energies are given in eV and are relative to the ground state of neutral 2-propanol. (b) Electrostatic potential projected on the electron density; isovalue of the electron density: 0.0004 a.u., limits of the potential: 0.15 a.u. (red) 0.22 a.u. (blue). (c) Hydrogen bonded structure, minimum in the PES of the cationic 2-propanol after CH_3 roaming (d) Spin density difference: $\delta\rho_{\text{spin}} = \rho_\alpha - \rho_\beta$ in the singly-charged hydrogen bonded structure.

For a better understanding of the KER distribution *2*, one must go beyond the present AIMD simulations and perform explicit calculations of the critical points of the multi-dimensional potential energy surface, i.e., the local minima and saddle points that determine the fate of the calculated trajectories. After the pump pulse, cationic 2-propanol can undergo relaxation via a significant elongation of one of the C−C bonds. As discussed earlier, the methyl group can not only be directly ejected by the probe pulse but can also change its position relative to the remaining molecular fragment. Two isomerization pathways involving one of the methyl groups are shown in the Fig. 3.10 (a): (i) methyl migration: this leads to the formation of a new C−O bond, and CH_3 is subsequently released from the new structure and (ii) methyl roaming: the methyl fragment moves around forming a hydrogen-bonded structure before undergoing probe-induced fragmentation. Both mechanisms shown in Fig. 3.10 (a) indicate that the CH_3 group does not immediately escape; instead it remains temporally trapped in the potential generated by the larger CH_3CHOH^+ fragment. Fig. 3.10 (b) shows the electrostatic potential generated by the remaining cationic fragment (CH_3CHOH^+) after cleavage of neutral CH_3 in singly-charged 2-propanol. The dark blue color indicates the region of attractive potential which is favorable for CH_3 roaming and facilitates the formation of hydrogen bonded structure shown in Fig. 3.10 (c). Since neutral CH_3 is a radical, with one unpaired electron in a p_z orbital perpendicular to the molecular plane, it can be easily polarized by the electrostatic potential. As a result, the methyl group is electrostatically trapped before getting ejected by the probe pulse.

The molecular dynamics simulations confirm our hypothesis of methyl roaming in 2-propanol. As an illustration, Fig. 3.11 shows the results for a typical trajectory demonstrating methyl roaming, where the methyl group evolves, approaching the −OH group to form the hydrogen bonded structure. C−C bond cleavage is observed after approximately 200 fs while the methyl group remains at a distance of 3 - 4 Å during the propagation time of 1000 fs. We note from Fig. 3.6 (a) that a C−C distance of ∼ 3 Å leads to ∼ 3 eV KER of the fragments when projected onto the dicationic state after the probe pulse. The appearance of methyl roaming strongly depends on the energy available in the system; at 10 eV and 15 eV internal energy, it is very rare, but at 5 eV methyl roaming is seen in

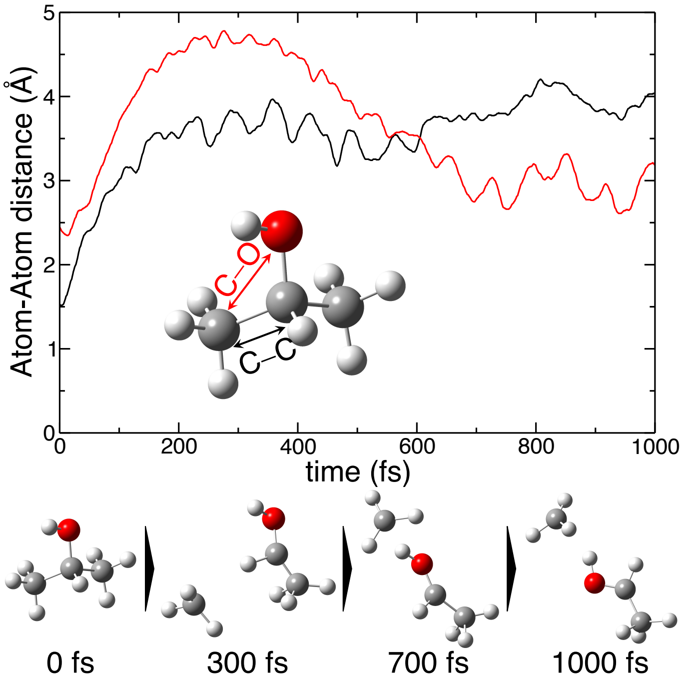

Figure 3.11: A typical trajectory of the molecular dynamics simulations showing methyl roaming. The upper plot shows C−O and C−C bond distances as a function of the time. The lower part shows snapshots of methyl roaming at different propagation time.

about 7.5 % of the trajectories. A similar roaming mechanism is not possible in 1-propanol due to its different atomic configuration. In summary, distribution ***2*** in 2-propanol indicates a possible methyl roaming mechanism, wherein the trapping of CH_3 in the electrostatic potential leads to an unchanging distance between the fragments with time, thereby giving rise to a constant KER. However, further experimental and theoretical work is needed to explicitly assign this feature to methyl roaming. For instance, previous experiments have observed similar methyl roaming mechanisms in the photodissociation of acetaldehyde, which was inferred from the formation of vibrationally hot CH_4 due to a hydrogen atom abstraction by the roaming CH_3 [103, 104]. These results were then confirmed by ab-initio calculations [105] as well as quasi-classical trajectory calculations using a global potential energy surface for acetaldehyde [106].

An important aspect of studying these molecular dynamics is to resolve the ultrafast timescales on which such processes occur. In order to obtain quantitative temporal information from the time-dependent KER band of different channels, a 2D

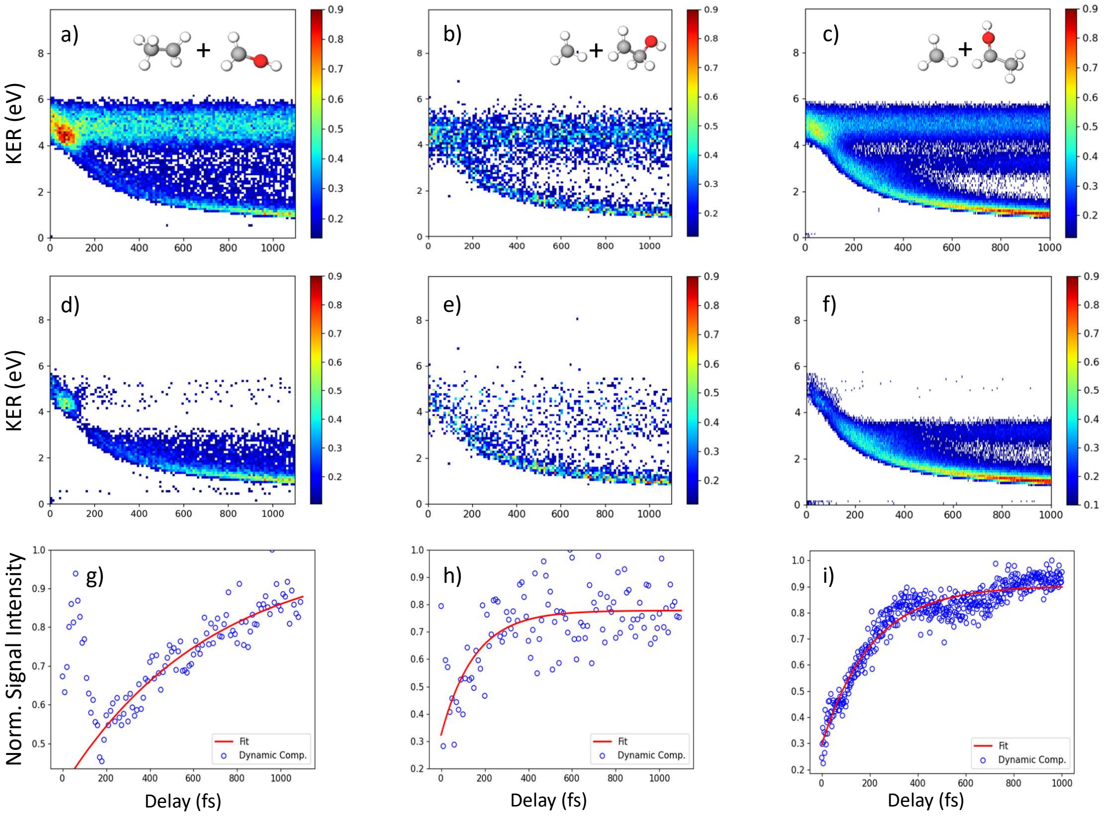

Figure 3.12: Fitting and projection of the delay-dependent KER for three different fragmentation channels of 1- and 2-propanol. Experimentally obtained KER vs time delay spectra for **(a)** CH_3^+ + CH_3O^+ and **(b)** CH_3^+ + $C_2H_5O^+$ of 1-propanol and **(c)** CH_3^+ + $C_2H_5O^+$ of 2-propanol, respectively. **(d) - (f)** the time-dependent KER spectra obtained from the subtraction of the Gaussian fit of the static KER band from the experimental data. **(g) - (i)** the projection of the time-dependent KER onto the delay axis (blue circles) along with their fits to a saturating exponential function (red line).

global fitting method is used [22]. The KER vs time delay spectra for all the reported channels is fit using two independent Gaussian functions at each recorded delay step. One Gaussian is used to fit the static band centered around 4.8 eV for the two-body coincidence channels (around 14 eV for the three-body coincidence channels). The mean position, amplitude and width of this Gaussian are constrained in order to model the relatively constant position and intensity of the static KER bands. The second Gaussian is used to model the dynamic KER distribution. Subtraction of the time-independent Gaussian fit from the KER vs. time delay spectrum isolates the time-dependent distribution which is then projected onto the delay axis. Afterwards, the data is fit to a saturating exponential of the form $1-e^{-(\Delta t-t_0)/\tau}$ in order to obtain the exponential time constant τ and time offset t_0. In Fig. 3.12, (a) - (c) show the experimental delay-dependent KER for the two-body fragmentation channels of 1- and 2-propanol. Fig. 3.12 (d) - (f) show the isolated time-dependent distribution obtained from subtraction of the static Gaussian fit from the experimental data, and (g) - (i) show the projection of the dynamic distribution and their fits to a saturating exponential. The values of τ and t_0 for all the channels of 1- and 2-propanol are given in Tables 3.4 and 3.5 respectively. Interestingly, of all the coincidence channels analyzed, only the two-body fragmentation channel $C_2H_5^+ + CH_3O^+$ of 1-propanol shows a strong enhancement in intensity at small delays, with the peak occurring at around 50 fs. For comparison, the temporal resolution of our experiment is $\sim$ 13 fs. We do not have a complete understanding of what causes this enhancement effect but it can possibly be attributed to some kind of enhanced ionization (EI) for this particular channel at small time delays.

Channel	τ (fs)	t_0 (fs)
$CH_3^+ + C_2H_4OH^+$ (Fragmentation)	152 ± 64	37 ± 30
$C_2H_5^+ + CH_2OH^+$ (Fragmentation)	671 ± 338	73 ± 70
$CH_2^+ + CH_3^+ + CH_2OH^+$ (Fragmentation)	219 ± 73	33 ± 29
$CH_3^+ + H_2O^+ + C_2H_3^+$ (SHM)	289 ± 187	56 ± 58

Table 3.4: Time constant and time shift of double and triple coincidence channels observed for 1-propanol

Channel	τ (fs)	t_0 (fs)
$CH_3^+ + C_2H_4OH^+$ (Fragmentation)	210 ± 13	8 ± 6
$CH_3^+ + CH_3^+ + CHOH^+$ (Fragmentation)	728 ± 310	35 ± 33
$CH_3^+ + H_2O^+ + C_2H_3^+$ (SHM)	321 ± 94	29 ± 28

Table 3.5: Time constant and time shift of double and triple coincidence channels observed for 2-propanol

In addition to the unique distribution ***2*** indicating possible methyl roaming in the fragmentation channel $CH_3^+ + C_2H_5O^+$ of 2-propanol, evidence of EI identified by an increase in the ionization yield is also observed. To better quantify the EI, Fig. 3.13 (b) shows the projection of the dynamic part of the KER signal inside the red dashed box from Fig. 3.13 (a), onto the time delay axis. The dashed box spans from 200 fs to 1000 fs on the delay axis and from 0.5 eV to 4.0 eV on the KER axis. The experimental data points (grey dots) in Fig. 3.13 (b) are used to generate a moving average (red line) which shows an increase in the signal intensity between 200 fs and 450 fs, indicating EI. This phenomenon has been observed in various hydrocarbons like ethylene, acetylene and 1,3-butadiene [107, 108] where unexpectedly high molecular charge states are observed when the internuclear distance reaches a critical value. As the bond gets stretched in the presence of an external laser field, there may exist regions in the molecular potential where the tunneling barriers become lower and/or narrower than at equilibrium geometry. This can result in a more efficient ionization pathway for the electrons to tunnel out. In the case of 2-propanol, it is possible that at some critical internuclear separation between the two carbon atoms and in the presence of the electric field of the probe pulse, electrons are more readily ejected leading to an increase in the yield of this double coincidence channel. More precisely, from a plot of the spin density difference ($\rho_\alpha - \rho_\beta$, see Fig. 3.10(d)) for the geometry corresponding to the hydrogen bonded structure (the more favorable one in methyl roaming), one can observe that the unpaired electron of the methyl group appears quite delocalized with one lobe pointing outwards in the direction perpendicular to the molecular plane. This electronic distribution of the unpaired electron of the roaming CH_3 fragment could also be responsible for the enhanced ionization observed in 2-propanol.

Single and double hydrogen migration, though ubiquitous, are complicated molecular processes that are not completely understood. Similar experiments to study hydrogen migration conducted on ethanol [21] and acetonitrile [22] reveal stark differences in the molecular dynamics initiated by laser ionization. Comparison with the propanol isomers shows that factors such as the length of the

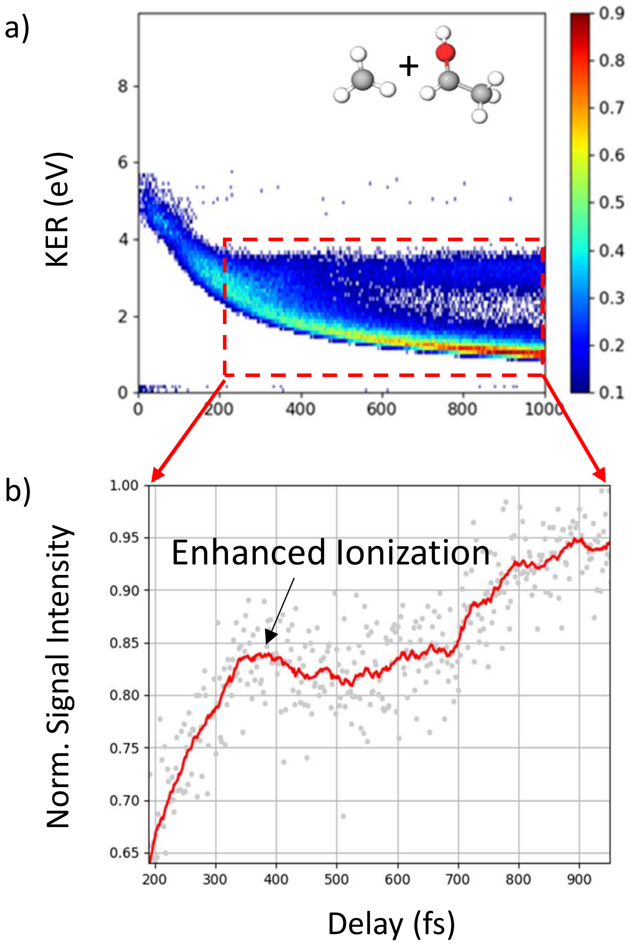

Figure 3.13: **(a)** Delay-dependent KER for the fragmentation channel CH_3^+ + $CHOHCH_3^+$ of 2-propanol. **(b)** Projection of KER signal inside the red-dashed box, shown in **(a)**, onto the delay axis shows increase in ionization yield indicating enhanced ionization. See text for more details.

carbon chain have a strong impact on the likelihood of hydrogen migration. Reported yields for double ion coincidences in ethanol [21] show that the double hydrogen migration (DHM) channel has the highest yield, followed by SHM and direct fragmentation of the C−C bond. Similarly, in acetonitrile [22], hydrogen migration leads to formation of very stable linear and ring isomers upon laser excitation, most of which are more stable than its canonical cationic structure. This results in SHM being the most likely process, closely followed by DHM. However, in the propanol isomers, no hydrogen migration is observed in the two-body fragmentation channels, and only weakly observed in the three-body channels. These findings indicate, surprisingly, that the viability of intramolecular hydrogen migration decreases as the carbon chain length increases, even though the number of hydrogen atoms available for migration increases. Our results show similar trends to a recent study of primary alcohols in a strong laser field, where it was observed that the probability of ${H_3}^+$ formation, via a roaming neutral H_2, decreases as the carbon chain length increases from methanol to the propanol isomers [109]. The authors indicate that molecular structural features such as the prevalence of α-hydrogen atoms affect the pathways and thus the probability of ${H_3}^+$ formation.

3.7 Conclusion

In summary, we have used a IR pump - IR probe spectroscopy in combination with kinematically complete coincident Coulomb explosion imaging to investigate hydrogen migration dynamics in acetonitrile and the two propanol isomers. Our measurements enabled us to examine the time-resolved dynamics of single and double hydrogen migration across two- and three-body coincidence channels, as well as to compare the relative yields of various fragmentation mechanisms within these molecules. To gain deeper insights into the underlying mechanisms, we used ab-initio molecular dynamics calculations and explored several potential energy surfaces using density functional theory.

In acetonitrile, we discover that isomerization, involving both single and double hydrogen migration, is significantly more probable than direct C-C bond breakup. Theoretical modelling allows us to understand this effect by demonstrating that the isomerized structures of singly-charged acetonitrile are remarkably stable and can be accessed via relatively low potential energy barriers.

In contrast, for 1- and 2-propanol, we observe that direct C-C bond fragmentation is the most dominant channel. Hydrogen migration is found to occur with a very low yield and is only observed in the case of triple ionization in these molecules. Our work on propanol and acetonitrile, in combination with our previous work on ethanol [21], highlights the strong effect that an increase in carbon chain length has on the likelihood of hydrogen migration. Contrary to expectations, our results suggest that an increase in alkyl chain length diminishes the likelihood of hydrogen migration. In particular, while double hydrogen migration is the most dominant channel observed in ethanol, this process is entirely absent in both the propanol isomers. This chapter is based on work that was done in collaboration with Aaron LaForge, Razib Obaid, Matteo McDonnell, Juan Reino-González, Martin Disla, Nora Kling, Margaret Sundberg, Vít Svoboda, Sergio Díaz-Tendero, Fernando Martín, and Nora Berrah [22, 23].

Chapter 4

Studying roaming reactions by tracking neutral fragments

4.1 Introduction

Understanding the multitude of complex molecular processes proceeding through photoexcitation is of fundamental importance to a wide variety of biological and chemical systems. One of the most common photochemical processes is dissociation, which typically proceeds by the fragmenting molecule moving along the minimum energy path. However, there exists a more complex pathway, known as roaming, where the neutral fragment spans the relatively flat regions of the potential energy surface, farther from the minimum energy path, due to long-range, weakly-bound interactions. Roaming has been a subject of great interest in recent years [110–112] since its initial indirect observation in formaldehyde [113], and has been proposed to occur in several small molecules such as acetaldehyde [103, 114], acetone [115], nitrate [116], methyl formate [117, 118], propane [119], and 2-propanol [23].

Roaming is known to play a crucial role in the formation of H_3^+, one of the most abundant molecular ions in the universe [120, 121]. H_3^+ formation dynamics is of great importance in gas-phase astrochemistry, due to its critical role as an intermediate in the synthesis of more complex molecules [122–124]. Very recent works [123, 124] have specifically examined the formation of D_3^+, an isotope of H_3^+, from a bimolecular reaction in D_2–D_2 dimers as a potential explanation for its unexpectedly high abundance in interstellar molecular clouds. High-powered, ultrafast lasers have emerged as an efficient means of producing H_3^+ ions through photoexcitation of organic molecules and have thus facilitated further exploration of their dynamics [125–131]. Notably, roaming of H_2, triggered by intense femtosecond IR laser pulses, has been shown to result in H_3^+ formation in monohydric alcohols [109, 132]. Complementary experiments, using XUV femtosecond laser pulses and Coulomb explosion imaging (CEI) [2, 133–136], have also explored the role of this mechanism leading to H_3^+ formation. In both cases, roaming is initiated in the molecular dicationic state. IR pulses rely on strong-field ionization due to a strong coupling between the molecular system and the electric field of the laser, while XUV pulses can prompt single-photon double-ionization. As such, roaming is quite ubiquitous and recently has also been suggested to occur in neutral formaldehyde, rather than from the dicationic state [137].

Despite recent efforts, the real-time, direct visualization of roaming has remained elusive from experimental observations due to its complex nature. The central problem is the random nature of the roaming process, where the position of the roaming particle relative to the rest of the system is not deterministic. For instance, pioneering experimental studies inferred the role of roaming neutral H_2 in H_3^+ formation by using time-resolved mass spectra [109, 132]. In the absence of coincident momentum imaging, it is not possible to directly identify which fragmentation channels contributed to the formation of H_3^+. More recently, Endo *et al.* [137] demonstrated the time-resolved signature of roaming in neutral formaldehyde by investigating a three-ion coincidence channel using CEI. However, this channel carried imprints of various reactions that are triggered via UV excitation of formaldehyde, including molecular and radical dissociation, as well as roaming. As a result, it was necessary to incorporate high-level simulations to identify the signature of roaming from the experimental results.

In this chapter, we directly track the roaming process by experimentally measuring the complex dynamics of the neutral H_2, a crucial intermediate in the formation of H_3^+, in acetonitrile, CH_3CN. In general, the neutral character of the roaming fragment makes it invisible to charged-particle detection schemes and further, its random trajectory makes it extremely difficult to track both spatially and temporally. However, with the use of coincident momentum imaging in combination with femtosecond 800 nm IR-IR pump-probe spectroscopy, we have access to the full, time-resolved 3D momentum information of each detected fragment. This enables us to reconstruct the momentum vector of the undetected neutral fragment in a reaction, by virtue of momentum conservation. Such kinematically complete information, even for a coincidence channel involving a neutral fragment, is crucial for mapping out a direct signature of roaming reactions without any interference from other excited state dynamics. For our experiment, we choose acetonitrile (CH_3CN), an ideal molecule with a relatively simple structure comprising just three hydrogen atoms, all bonded to the same carbon. As compared to previous work [109, 132], this eliminates any ambiguity regarding the specific hydrogen atoms involved in H_3^+ formation, ensuring a singular pathway for this process. Additionally, considering acetonitrile's extensive use in industrial and chemical applications [138, 139], gaining an in-depth understanding of its electronic and molecular reaction dynamics is critically important.

4.2 Schematic

The schematic shown in Fig. 4.1 illustrates the dynamics induced in CH_3CN via the pump and probe pulses as well as the intermediate processes in our experiment. Using a femtosecond IR pump pulse, we excite CH_3CN to the dicationic state, where a neutral H_2 dissociates and roams in the vicinity of C_2NH^{2+} due to the relatively flat potential energy surface. This forms the parent roaming channel, from which various fragmentation pathways emerge. Predominantly, we observe H_2 + H^+ + C_2N^+ from the parent roaming channel. A subset of the events from the parent channel undergo proton transfer (PT), where the roaming H_2 captures a hydrogen ion from C_2NH^{2+} to form H_3^+ + C_2N^+ [109, 132, 135]. Additionally, electron transfer (ET) from the roaming neutral H_2 to C_2NH^{2+} may occur, resulting in H_2^+ + C_2NH^+ [2, 135]. These competing pathways of PT and ET occur on the dicationic state with roaming H_2, independent of the probe pulse. On the other hand, interaction with the probe pulse can ionize the roaming H_2,

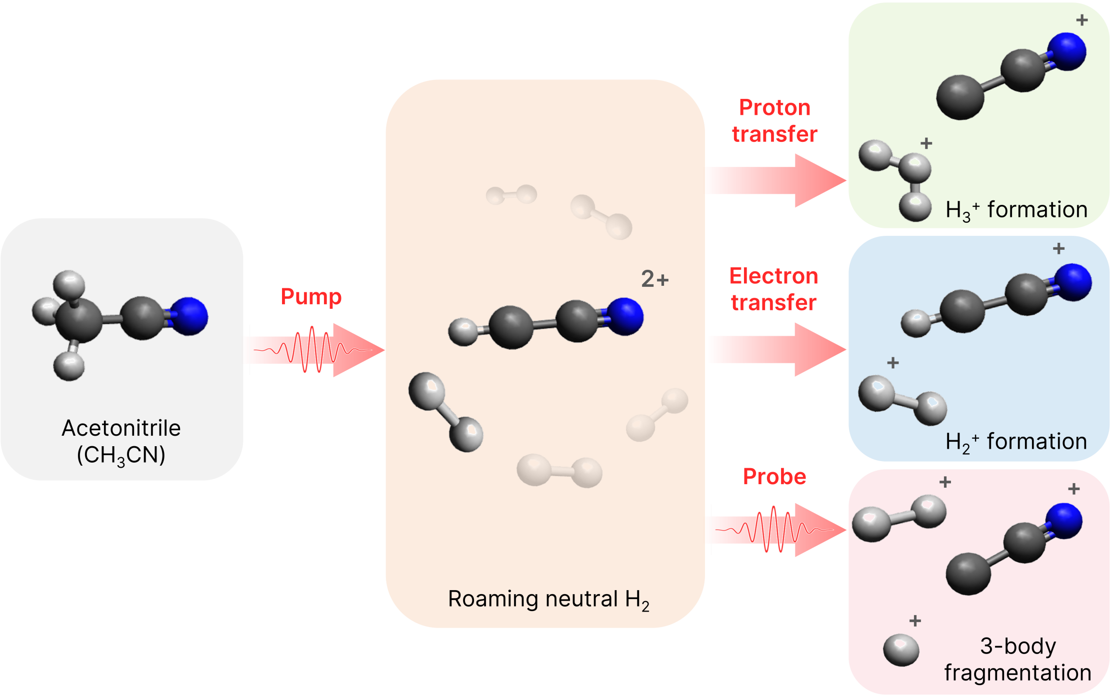

Figure 4.1: Schematic representation of H_2 roaming induced by the pump pulse and the resultant product channels in CH_3CN. The pump pulse creates the parent dicationic state, $[CH_3CN]^{2+}$ through multiphoton absorption, followed by neutral dissociation of H_2. A small subset of these events may lead to either proton transfer ($H_3^+ + C_2N^+$) or electron transfer ($H_2^+ + C_2NH^+$) without the involvement of the probe pulse. Conversely, the roaming H_2 may be ionized by the probe pulse, resulting in the formation of $H^+ + H_2^+ + C_2N^+$ channel.

leading to a triple-ion coincidence channel, $H^+ + H_2^+ + C_2N^+$, which disrupts both the PT and ET pathways. A detailed comparison of the relative yields of the parent roaming channel and the three product channels is discussed later in the manuscript, focusing on the correlation and competition between the channels. All the channels of interest are determined in a kinematically complete manner as the momenta of all ionic fragments are measured in coincidence using the COLTRIMS technique [47, 89] discussed in Chapter 2 of this thesis. An in-depth discussion of our specific experimental parameters is given in the Experimental Methods section below. We have additionally performed analogous measurements using deuterated acetonitrile, where all three hydrogen atoms are replaced by deuterium. This allows us to better resolve different masses of the detected charged particles. The deuterated or undeuterated measurements will be explicitly noted throughout the chapter, including a comparison of their temporal dynamics.

4.3 Experimental methods

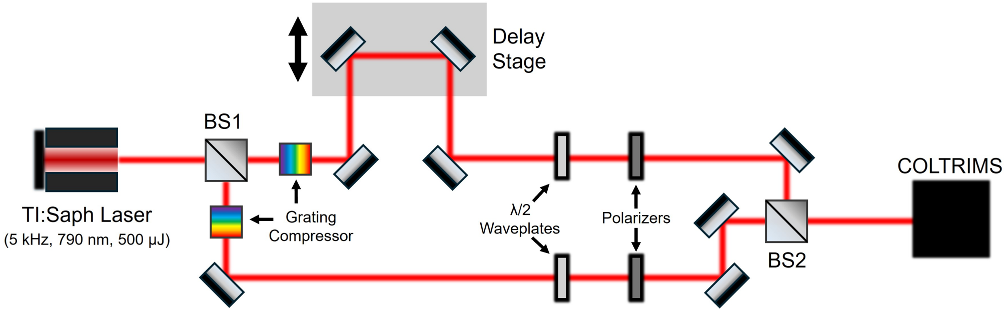

Figure 4.2: A schematic of the IR pump-IR probe experimental setup.

A schematic of the experiment setup is shown in Fig 4.2. We used a 5 kHz Ti:Sapphire laser producing 35 fs pulses with a central wavelength of 790 nm. The laser beam was split into two independent arms which were time-delayed with respect to one another. Each arm had an optical grating compressor to generate transform limited pulses and had variable intensity controlled by a combination of $\lambda/2$ waveplate and polarizer. The pulse intensities were optimized to produce the highest contrast on the ${H_3}^+/{D_3}^+$ signal. For this experiment, the intensity of the pump and probe arms were respectively 3.2×10^{14} W/cm^2 and 2.0×10^{14} W/cm^2. The higher-intensity laser pulse served as the pump, and the weaker pulse as the probe for positive delays (vice-versa for negative delays). The two beams were directed into the interaction region where they were overlapped and back-focused to a spot size of about 10 μm with a temporal resolution of about 60 fs. Both beams were linearly polarized in the direction of the time-of-flight axis of the spectrometer. A cold, molecular jet of acetonitrile, from a room-temperature bubbler, was produced by expansion through a 30 μm nozzle seeded with 1 bar of helium gas and propagated into the spectrometer perpendicular to the two laser pulses. Acetonitrile was ionized and resulting charged fragments were detected by a Cold Target Recoil Ion Momentum Spectrometer (COLTRIMS) [47, 89], also discussed in Chapter 2 of this thesis. Using a weak, homogeneous electric field of 8.8 V/mm, the ions were directed towards a position-sensitive detector, which is capable of measuring the three-dimensional momentum distributions of the charged particles. For CEI, we primarily focus on measuring the fragmented ions, and for the current experimental conditions, we have an ion momentum resolution of 0.1 a.u. By applying the coincidence technique, we can isolate specific mass channels of acetonitrile and gain the most relevant information about the fragmentation dynamics.

4.4 Simulation methods

Ab initio molecular dynamics simulations were performed by our collaborators Fernando Martín and Sergio Díaz-Tendero, using the Atom Centered Density Matrix Propagation method (ADMP) [96–98] as implemented in the Gaussian16 program [100]. The electronic structure was computed, employing the density functional theory (DFT), in particular, the B3LYP functional [94, 95] in combination with the 6-31++G(d,p) basis set [140, 141]. To ensure the adiabaticity of the dynamics, we established a time step of $\Delta t = 0.1$ fs and a fictitious electron mass of $\mu = 0.1$ amu. Mimicking the experimental conditions, we considered a vertical double ionization of the acetonitrile molecule in a Franck–Condon manner, introducing a given amount of internal energy, $E_{exc} = 3$ eV, which was randomly redistributed over the nuclear degrees of freedom. This value was chosen to ensure that the energy available in the system agrees with the experimentally measured KER.500 trajectories were propagated up to 1 ps. We analyzed the statistical population of the different channels considering separated fragments with distances larger than 2.5 Å between atoms forming a moiety. Charges in the different atomic positions were computed from a Mulliken population analysis in the last step of each trajectory. We have successfully used this computational strategy in the past to infer the fragmentation dynamics in ionized molecules and clusters in the gas phase (see e.g. [21–23, 84, 90, 91, 93, 102, 142, 143]).

4.5 Results and discussion

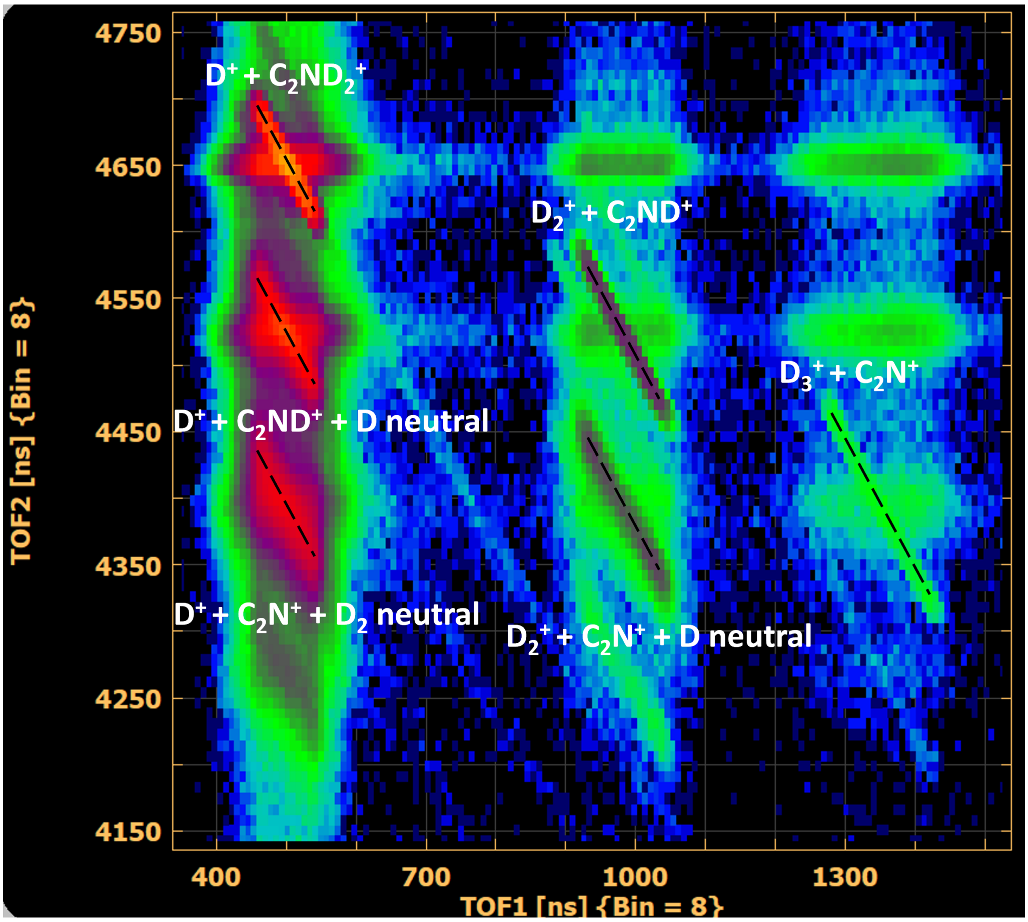

Figure 4.3: Photoion-photoion coincidence map for deuterated acetonitrile.

The photoion-photoion coincidence map, described in more details in Chapter 2 of this thesis, for deuterated acetonitrile is shown in Fig. 4.3 with all the complete and incomplete channels identified. Our investigation into the roaming process starts with the experimental imaging of the underlying dynamics of roaming neutral D_2, the precursor to the formation of D_3^+. Here, we investigate the incomplete coincidence channel of D^+ and C_2N^+, using photoion–photoion coincidence (PIPICO) maps, shown as an isolated channel in Fig. 4.4 (a). Such incomplete coincidence channels carry valuable information about the intrinsic dynamics in neutral fragmentations or events involving undetected fragments. Recent studies have started to explore such channels in small molecules, utilizing both Coulomb explosion imaging [135, 136, 144] and photoelectron momentum distributions [145]. The incomplete PIPICO channel in Fig. 4.4 (a) exhibits a distribution of slope of -1 and is broad due to the missing momentum carried away by the undetected fragment, D_2. Such broadening of the coincidence channel implies a case of deferred charge separation, where the neutral fragment is ejected first, followed by the remaining dicationic moiety breaking apart into two ions [60]. For comparison, the PIPICO map for the complete channel, ${D_3}^+$ and C_2N^+, is shown in Fig. 4.4 (b), where a very sharp distribution of slope -1 is observed due to momentum conservation.

An in-depth examination of the kinematic and time-resolved dynamics associated with this incomplete coincidence channel will enable us to disentangle the behavior of the roaming fragment. By leveraging momentum conservation of the three fragments, the momentum vector and hence, the kinetic energy of D_2 can be reconstructed. The reconstructed kinetic energy, shown in Fig. 4.5, is less than 1 eV, which reinforces that the missing fragment D_2 in our incomplete channel is indeed neutral, and not an ion that was simply lost in the detection process. In Fig. 4.4 (c), we plot the angle between the momentum vectors of D_2 and D^+ (blue line), and D_2 and C_2N^+ (orange line). Overall, we see a large spread in the angular distributions between the neutral D_2 and the other two ions, implying a nearly random angle of emission for D_2, a key signature of roaming. This is because roaming fragments traverse relatively flat regions of the potential energy surface, which results in wide variations in their pathways, in contrast to direct dissociation, where the fragments follow a fixed minimum energy path. By mapping the momentum vector of the neutral fragment, we thus have a more direct method for tracking roaming reactions.

In contrast to the roamer-ion angular distributions, in Fig. 4.4 (c), the ion-ion angular distribution for D^+ and C_2N^+ (green line) for this incomplete channel is much sharper and centered at $\sim 160°$, indicating strong Coulomb interaction resulting in a stronger momentum correlation. Additionally, for comparison, the angular distribution for ${D_3}^+$ and C_2N^+ (crimson line), which forms a complete two-

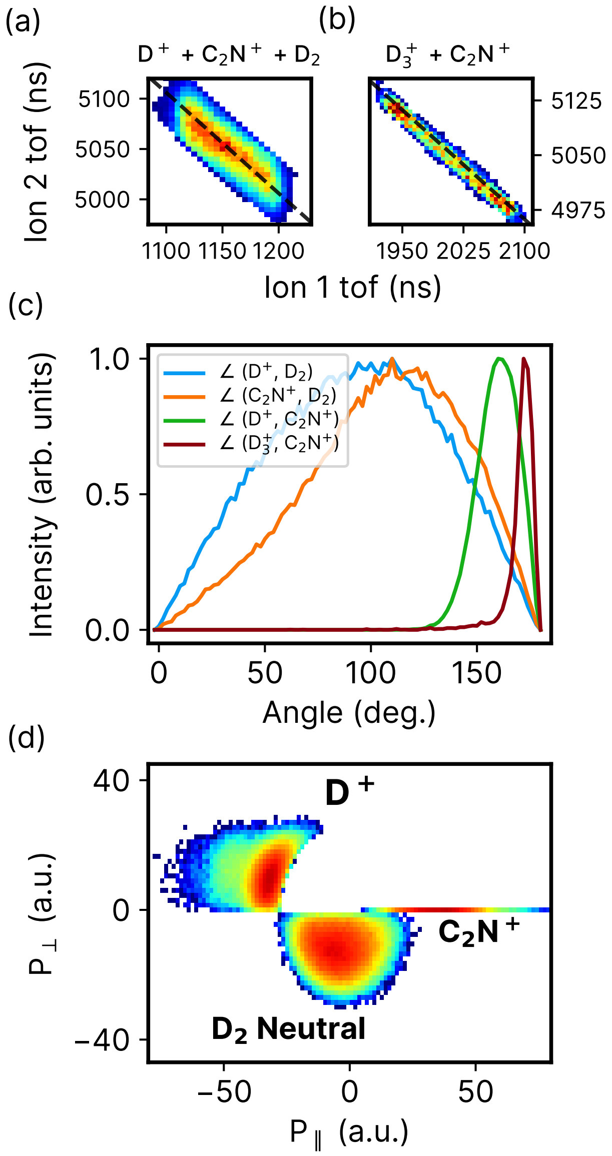

Figure 4.4: Photoion-photoion coincidence lines for (a) D^+ + C_2N^+ + D_2 and (b) ${D_3}^+$ + C_2N^+ from acetonitrile, integrated over all pump-probe delays. Black dashed lines of slope -1 are overlaid on the PIPICO channels (a) and (b) to demonstrate the agreement between the expected and experimentally-obtained slope of these channels. (c) Angular distribution between the momentum vectors of D^+ and D_2 (blue line), C_2N^+ and D_2 (orange line), D^+ and C_2N^+ (green line), and ${D_3}^+$ and C_2N^+ (crimson line) within the first 200 fs time delay window. (d) Newton diagram for the channel D^+ + D_2 neutral + C_2N^+ integrated over the first 200 fs of pump-probe delay. The momentum vector of C_2N^+ lies along the x-axis while those of D^+ and D_2 neutral are plotted in the top and bottom halves, respectively.

body channel, is even narrower and centered at ∼ 175° indicating back-to-back emission, as would be expected from a two-body fragmentation process.

Beyond examining angular correlations between momentum vectors, we can

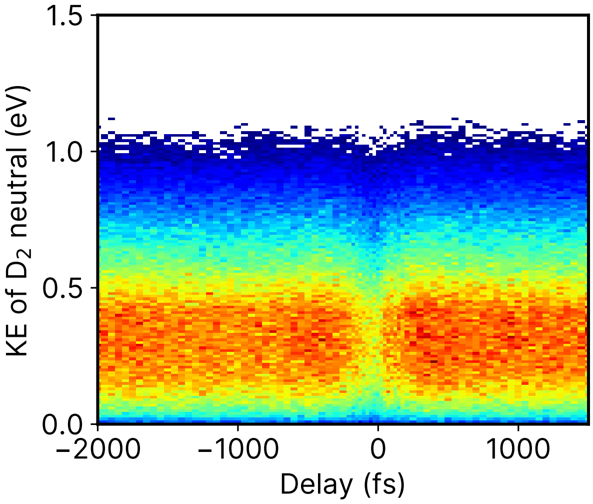

Figure 4.5: Pump-probe delay dependent kinetic energy of the neutral D_2 from the channel D^+ + C_2N^+ + D_2.

also map the relative 3D momenta of the coincident fragments using Newton diagrams. In general, Newton diagrams are very useful tools for providing structural information about the reaction dynamics of a molecular system [24, 51, 53]. One of their unique features is the ability to distinguish different mechanisms of fragmentation: concerted, instantaneous fragmentation would appear as sharp, localized distributions in the Newton diagram [70], whereas sequential fragmentation would appear as a thin semicircle [51, 71, 146].

Fig. 4.4 (d) shows the Newton diagram for the channel D^+ + D_2 neutral + C_2N^+. Here, the pump-probe delay is constrained to values less than 200 fs. The momentum vector of C_2N^+ is fixed along the x-axis, while those of D^+ and the reconstructed D_2 are plotted on the top and bottom halves, respectively. Due to momentum conservation amongst the three fragments, the Newton diagram lies on a plane and shows the relative momentum distributions of the two other fragments with respect to C_2N^+. Overall, several features of the D_2 neutral momentum distribution are markedly different from the all-ion channel (D^+ + ${D_2}^+$ + C_2N^+). Particularly, the distribution of the neutral D_2 in Fig. 4.4 (d) shows a lack of clear angular dependence in addition to a very broad, albeit lower momentum magnitude distribution. This implies that the neutral D_2 departs with a smaller fraction of the total momentum involved in this process, as would be expected from neutral fragmentation. This broad distribution of momentum magnitude of the neutral D_2 in conjunction with a lack of clear angular correlation is an unambiguous experimental signature for the roaming pathways. In contrast, the two ions in this incomplete channel, D^+ and C_2N^+, share a stronger momentum correlation mediated via Coulomb interaction, as evidenced by a narrower angular spread along with a localized distribution of the magnitude of momentum. It is worth noting that in sequential processes, broad angular distributions can also arise from the rotation of the intermediate fragment. To eliminate any ambiguity, the Newton diagram in Fig. 4.4 (d) is integrated over the first 200 fs pump-probe delay window, which is significantly shorter than the rotational timescale of the intermediate C_2ND^{2+}. As a result, the broad angular correlation that we observe here cannot be attributed to the rotation of C_2ND^{2+} and is solely due to the roaming process.

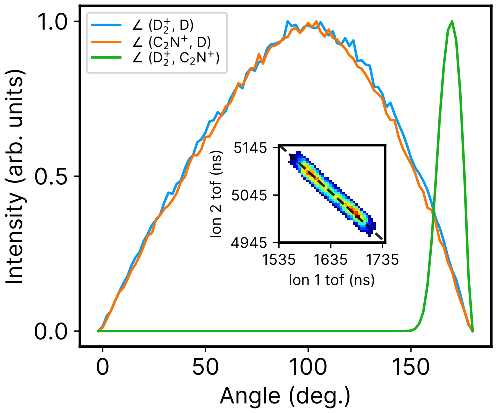

Figure 4.6: Angular distributions between pairs of fragments in the incomplete ${D_2}^+$ + C_2N^+ + D channel

Thus far, we have only discussed the role of neutral D_2 in the formation of ${D_3}^+$. However, for a comprehensive exploration of the various pathways that can contribute to ${D_3}^+$ formation, we must also consider a roaming neutral D which can potentially abstract ${D_2}^+$. Interestingly, we do observe such an incomplete coincidence channel, ${D_2}^+$ + C_2N^+ + D, shown as the inset in Fig. 4.6, which indicates the existence of a neutral D roaming pathway. We note that the yield for this channel is nearly 4.5 times lower than D^+ + C_2N^+ + D_2, consequently making it a weak contributor to the ${D_3}^+$ channel. This is not surprising, since a free H or

D atom is a radical, which makes it less likely to be formed than H_2 or D_2. In fact, this channel is not observed in our theoretical simulations due to the limited number of trajectories used in the present work. To our knowledge, it has also not been observed in previous works. Following the same sequence as before, we first ensure that the missing D is indeed a neutral by looking at its kinetic energy as a function of time-delay. Furthermore, we show the angular correlation between all pairs of fragments in the channel ${D_2}^+$ + D neutral + C_2N^+ in Fig. 4.6. The broad and symmetric angular correlations between the neutral D and the other two ionic fragments are indications of roaming D. Unlike in Fig. 4.4 (c), the correlation between D and C_2N^+ is quite symmetric. This could be a result of D being a lighter roaming fragment compared to D_2.

To better understand the mechanism of H_2 roaming and ${H_3}^+$ formation, our theory collaborators performed molecular dynamics simulations. We find that the primary fragmentation channels producing cationic hydrogen species and their respective abundances are: $H^+/H_2C_2N^+ \rightarrow 79.6\%$, ${H_2}^+/HC_2N^+ \rightarrow 7.6\%$, and ${H_3}^+/C_2N^+ \rightarrow 0.8\%$. For the current work, we focus our analysis on those trajectories producing ${H_3}^+$.

Among the 500 trajectories, we have identified 38 which lead to the release of H_2 (7.6% of trajectories). The production of H_2 in these trajectories occurs in a time interval of 20 - 350 fs. In some of those cases, we clearly observe roaming trajectories. We have selected one of these trajectories and performed a detailed analysis, shown in Fig. 4.7, with snapshots and time-evolution of C-H distances. Here, we can see that the excitation energy is stored in C-H vibrational modes while the H_2 is roaming. At ∼180 fs the vibrational energy is transferred to the H_2, which is observed by the C-H vibrational amplitude decreasing while the kinetic energy of H_2 increases simultaneously. In other words, while H_2 is roaming, the C-H bond stores a significant amount of vibrational energy, and there is not enough translational kinetic energy to emit the H_2. As soon as the energy is transferred from the vibrational mode of the C-H bond to the translation of H_2, then emission

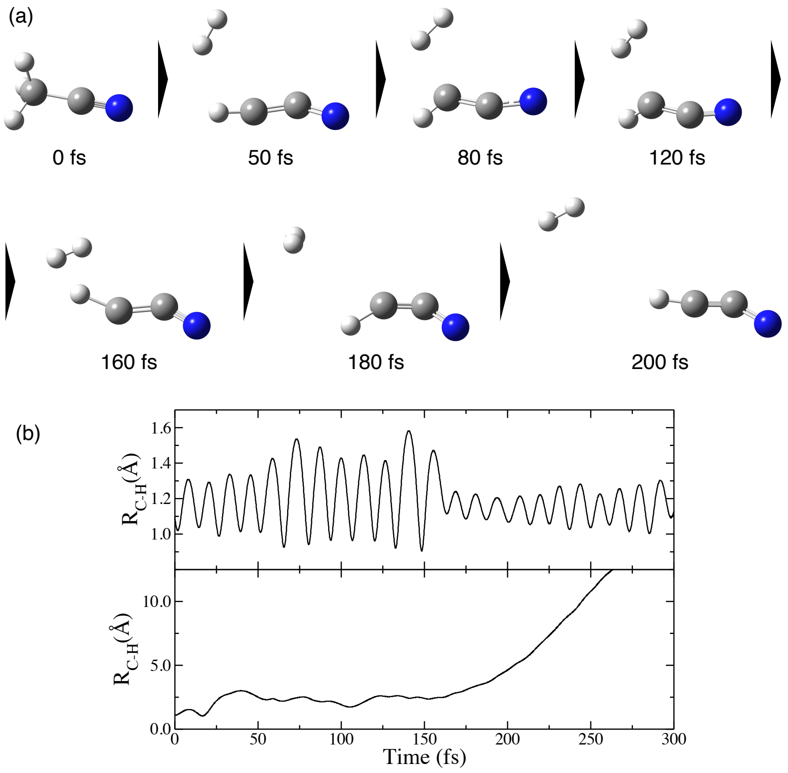

Figure 4.7: Example of trajectory leading to H_2 emission. (a) Snapshots at different times. (b) Two C-H distances as a function of time: upper panel the H atom that remains bonded to the C atom ; lower panel one of the H atoms of the emitted H_2.

occurs. It is impossible that an H_2^+ is the 'roamer' since it would get expelled due to Coulomb repulsion. We can thus conclude that H_2 is produced after roaming.

Further insight into H_2 roaming has been obtained via a careful exploration of the potential energy surface (PES). In particular, we computed the minimum energy path (MEP) that a doubly charged acetonitrile molecule would follow after vertical ionization, i.e., the maximum gradient on the PES, starting from the optimized geometry of the neutral system, shown in Fig. 4.8 (a). We clearly observe the release of neutral H_2, followed by the production of a weakly bonded H_2...$HCCN^{2+}$ complex. Furthermore, this shows that the neutral H_2 is polarized by the potential exerted by the dicationic fragment. We evaluated such potential by computing the electrostatic potential (ESP) of $HCCN^{2+}$ in two different configurations: using the geometry of the optimized structure from the moiety (Fig. 4.8 (b)) and using the geometry of the last point given in the MEP exploration (Fig. 4.8 (c)). The ESP is plotted in both cases by projecting the actual value on the electronic density isosurface, which

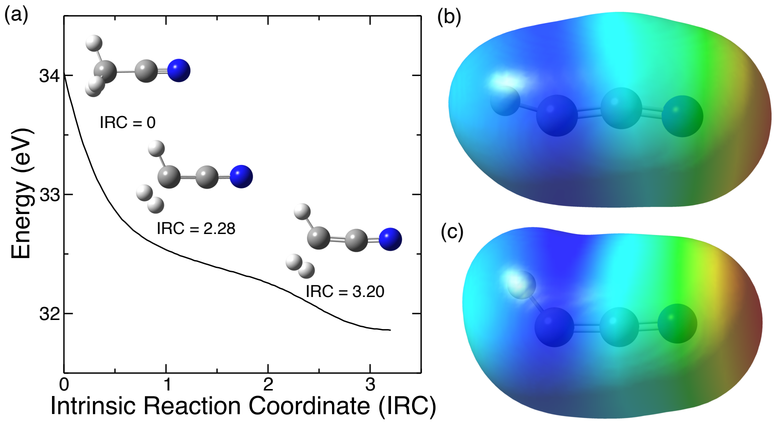

Figure 4.8: (a) Minimum energy path (MEP) followed in the potential energy surface of the doubly ionized acetonitrile; relative energy in eV referred to the neutral molecule as a function of the Intrinsic Reaction Coordinate (IRC). (b) and (c) Electrostatic potential (ESP) of $HCCN^{2+}$ mapped on the electronic density with isovalue 0.0004 a.u.. Color code for the extreme values: red = 0.32 a.u. and dark blue = 0.48 a.u.. The geometry used in (b) corresponds to the channel $H_2/HCCN^{2+}$, i.e. after release of neutral H_2, and in (c) to the weakly bonded $H_2...HCCN^{2+}$, i.e. last point in the MEP.

provides a visualization of the potential that polarizes the neutral H_2. Overall, Figs. 4.8 (b) and (c) reveal that the regions with the highest electrostatic potential (blue in color) are nearest to the C–H bond in $HCCN^{2+}$. It is most likely that the roaming H_2 remains weakly-bound in this region. Upon fragmentation of H^+ and CCN^+, the H_2 is approximately at 90° with respect to the two ionic fragments, which qualitatively agrees with the angular correlations given in Fig. 4.4 (c).

After thoroughly investigating the dynamics of the neutral roamer, we now shift our focus to one of the final photoproducts formed through such roaming reactions in acetonitrile, namely $H_3{}^+$ formation. Fig. 4.9 (a) shows the kinetic energy release (KER) map of the complete coincidence channel $H_3{}^+ + C_2N^+$ as a function of pump-probe delay. Here, we primarily observe a horizontal KER band centered around 5 eV along with a very weak time-dependent KER behavior. This distinctive constant KER behavior is due to a single pulse exciting the molecule directly into the dicationic state, which induces the formation of $H_3{}^+$ and C_2N^+. This is in contrast to the generally observed time-dependent decrease in kinetic energy which is due to the excitation of the system into an ionic state by the pump pulse and further ionization by the probe pulse.

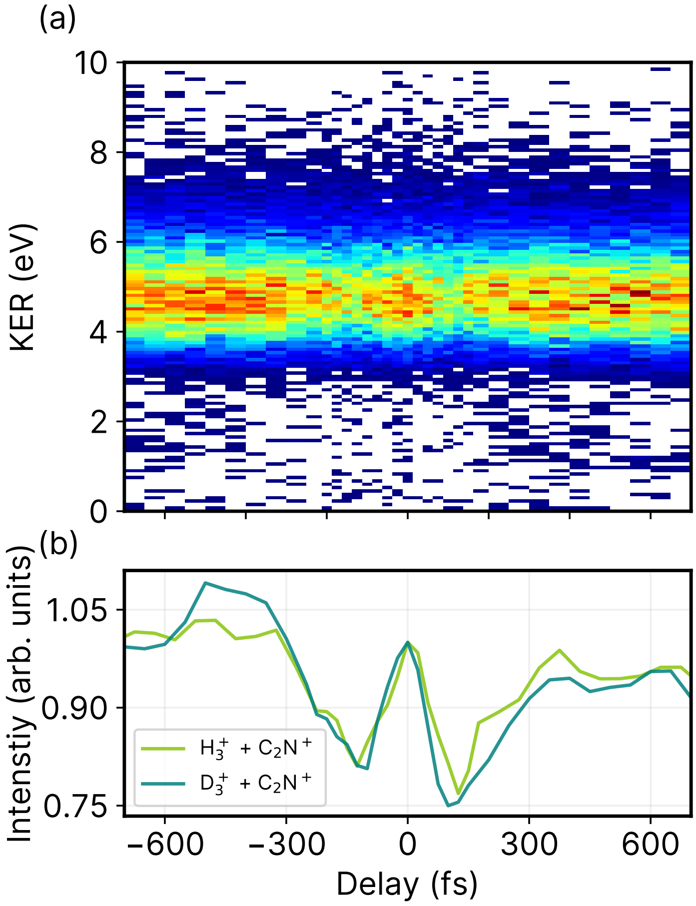

Figure 4.9: (a) Kinetic energy release of ${H_3}^+$ + C_2N^+ as a function of pump-probe delay. (b) Projection of the KER signal (between 3 eV and 7 eV) for ${H_3}^+$ + C_2N^+ (light green) and ${D_3}^+$ + C_2N^+ (dark green) on the pump-probe delay axis. The projected signal intensity in (b) is normalized to 1 at 0 fs pump-probe delay for both ${H_3}^+$ and ${D_3}^+$ channels.

Fig. 4.9 (b) shows the projection of the KER signal onto the pump-probe delay axis, highlighting the strong time-dependence of the KER intensity. The observed features can be explained as follows. The enhancement of the total yield around time zero of the pump-probe delay is due to the overlap of the two pulses. On either side of time zero, we see an immediate decrease in the yield before the signal steadily increases again - this behavior is the result of the disruptive nature of the probe pulse that prevents ${H_3}^+$ formation by ionizing the neutral roamer H_2 before it can abstract an H^+. In other words, if the probe pulse arrives before H^+ abstraction, then it disrupts the roaming H_2, resulting in a decreased ${H_3}^+$ yield. Conversely, for longer time delays, the probe pulse arrives after H^+ abstraction. Thus, it is unable to disrupt H_3^+ formation, which results in an increase in its yield until it reaches saturation.

In Fig. 4.9 (b), we show the delay-dependent KER projections of the formation of both H_3^+ (light green line) and D_3^+ (dark green line). Overall, we observed no significant differences, within our experimental resolution, between the two isotopes of acetonitrile in the time-resolved measurements. This observation strongly indicates that the roaming process in this particular case relies mostly on electronic properties rather than on nuclear dynamics. This differs from other roaming reactions observed in deuterated methanol (CH_3OD) [132, 147], where differences in timescale and kinetic energy release (KER) are noted for H_2D^+ and H_3^+ formation. In CH_3OD, these product fragments are formed through two distinct pathways, potentially explaining the observed variations in timescale and KER. On the other hand, acetonitrile exhibits a singular pathway for H_3^+ or D_3^+ formation, providing a contrasting scenario.

We next fit the projections of the KER signal with a rising exponential of the form: $y = A(1 - e^{(t-t_0)/\tau}) + y_0$ where A is the normalization constant, t is the pump-probe delay, t_0 is the time offset, τ is the time constant, and y_0 is the intensity offset. t_0 and τ have physical significance since they reveal the timescales of the respective depletion and enhancement of the H_3^+ and D_3^+ formation. The values from the fitting function are given in Table. 4.1 while a comparison of the fits with the experimental data is given in Fig. 4.10. The average value of the time offset, t_0, is 125 fs, which is larger than the temporal resolution of the experiment (60 fs) and that of the time constant, τ, is 105 fs. The fits indicate that H_2 roaming and H_3^+ formation occur on ultrafast timescales of approximately 200 fs, consistent with previously reported H_3^+ formation timescales in methanol, ethanol, acetone, and ethylene glycol [109, 132, 134].

Table 4.1: Fit values

Signal	**t_0**	τ
H_3^+ Neg Delay	-131 ± 6 fs	111 ± 23 fs
H_3^+ Pos Delay	127 ± 6 fs	75 ± 20 fs
D_3^+ Neg Delay	-121 ± 10 fs	105 ± 30 fs
D_3^+ Pos Delay	113 ± 5 fs	122 ± 25 fs

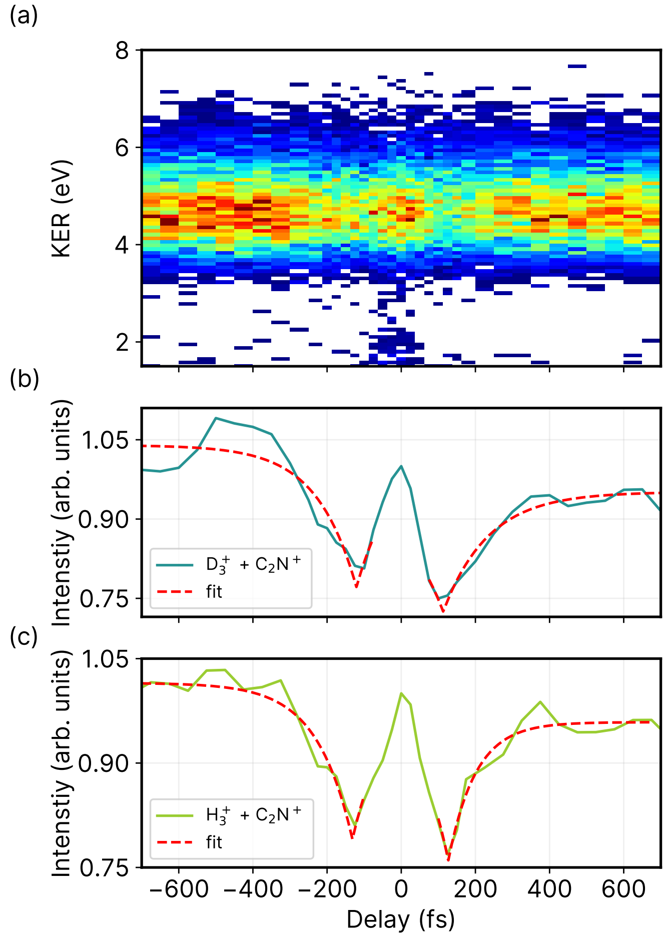

Figure 4.10: (a) Kinetic energy release of D_3^+ + C_2N^+ as a function of pump-probe delay. Projection of KER for (b) D_3^+ + C_2N^+ and (c) H_3^+ + C_2N^+ on the pump-probe delay axis. Red dashed lines obtained from the fit function (mentioned in the main text) are overlaid for comparison. The values from the fitting function are given in Table 4.1.

By leveraging the power of coincident Coulomb explosion imaging, we can explore time-dependent correlations between the different fragmentation channels. In this case, each final product channel proceeds through the roaming channel, C_2ND^{2+} + D_2, which is created by the pump pulse. Fig. 4.11 shows the yields of the predominantly-observed roaming neutral D_2 in coincidence with the ionic parent fragments (orange line), along with ${D_3}^+$ formation through proton transfer (green line), ${D_2}^+$ formation through electron transfer (blue line), and three-body ionization through probe pulse interaction (magenta line). All channels show an initial peak at zero delay due to pump-probe overlap, followed by a decrease in signal, which varies depending on the channel.

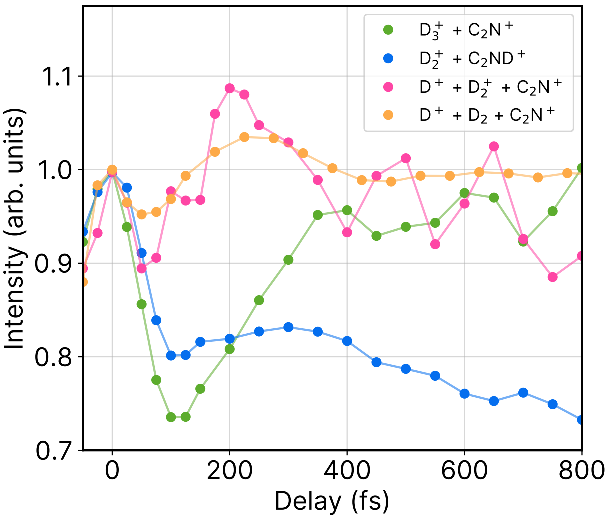

Figure 4.11: Projection of the KER signals as a function of pump-probe delay for ${D_3}^+$ + C_2N^+ and D^+ + ${D_2}^+$ + C_2N^+ and ${D_2}^+$ + C_2ND^+. Delay-dependent projection of the reconstructed roaming neutral D_2 is also shown. The projections are normalized to one at zero delay between the pump and probe pulses.

The roaming neutral channel (D_2 + D^+ + C_2N^+) shows a subtle delay-dependent change in yield. It has slightly higher yield at short time delays due to the increased ejection of the roaming neutral D_2, but this yield decreases slightly at longer delays as a result of branching into the final ionic product channels. Among them, the yield of the proton transfer channel (${D_3}^+$ + C_2N^+) initially shows a significant decrease before steadily increasing at later time delays. On the other hand, the three-body ionization channel (D^+ + ${D_2}^+$ + C_2N^+) shows the opposite trend, with a sharp initial increase followed by a slow decay. The inverse correlation between these two channels is due to the direct competition between these fragmentation processes. Specifically, the formation of ${D_3}^+$ is affected by the ionization of neutral D_2 to ${D_2}^+$ from the probe pulse. As a result, there is a significant increase in the yield of the triple-ion coincidence channel at short time delays, which then decreases due to higher ${D_3}^+$ formation at later time delays.

Finally, the electron transfer channel (${D_2}^+$ + C_2ND^+) shows an enhanced signal intensity near zero delay, with a relatively low, constant yield up to 400 fs. This is likely due to the fact that the ET process is effectively suppressed in our experiment, either due to disruption by the probe pulse at shorter delays or large internuclear separations hindering ET at later delays [135].

4.6 Comparing roaming and non-roaming neutral fragmentation processes

The technique of reconstruction of neutral fragment dynamics discussed here is very general and can also be applied for studying other types of photochemical processes mediated by neutral fragmentation. In order to fully demonstrate the differences between a roaming and non-roaming neutral fragmentation channel, we have plotted in the left column of Fig. 4.12 the relevant dynamics from ${CH_3}^+$ + H_2O neutral + ${C_2H_3}^+$ in 2-propanol ($CH_3CHOHCH_3$). The PIPICO channel, shown in Fig. 4.12 (a), is for ${CH_3}^+$ measured in coincidence with ${C_2H_3}^+$, with a missing mass of H_2O. This channel involves two primary fragments, ${CH_3}^+$ and $C_2H_5O^+$, the latter of which subsequently dissociates into ${C_2H_3}^+$ and neutral H_2O, with a slope that can be calculated as $-m_{C_2H_3^+}/(m_{C_2H_3^+} + m_{CH_3^+})$ = -0.643 [60]. A black dashed line of slope -0.643 is overlaid on this PIPICO channel to demonstrate the agreement between the expected and experimentally-obtained slope. Fig. 4.12 (b) shows the angular correlations between the momentum vectors of neutral H_2O and ${C_2H_3}^+$ (blue line) and neutral H_2O and ${CH_3}^+$ (orange line). Both these distributions are asymmetrically shifted either towards or away from 0° implying stronger momentum correlation, further corroborating that the neutral fragmentation of H_2O proceeds through a secondary decay from $C_2H_5O^+$. This behavior is in sharp contrast to that of corresponding angular distributions observed for the roaming neutral D_2 (shown to the right for comparison).

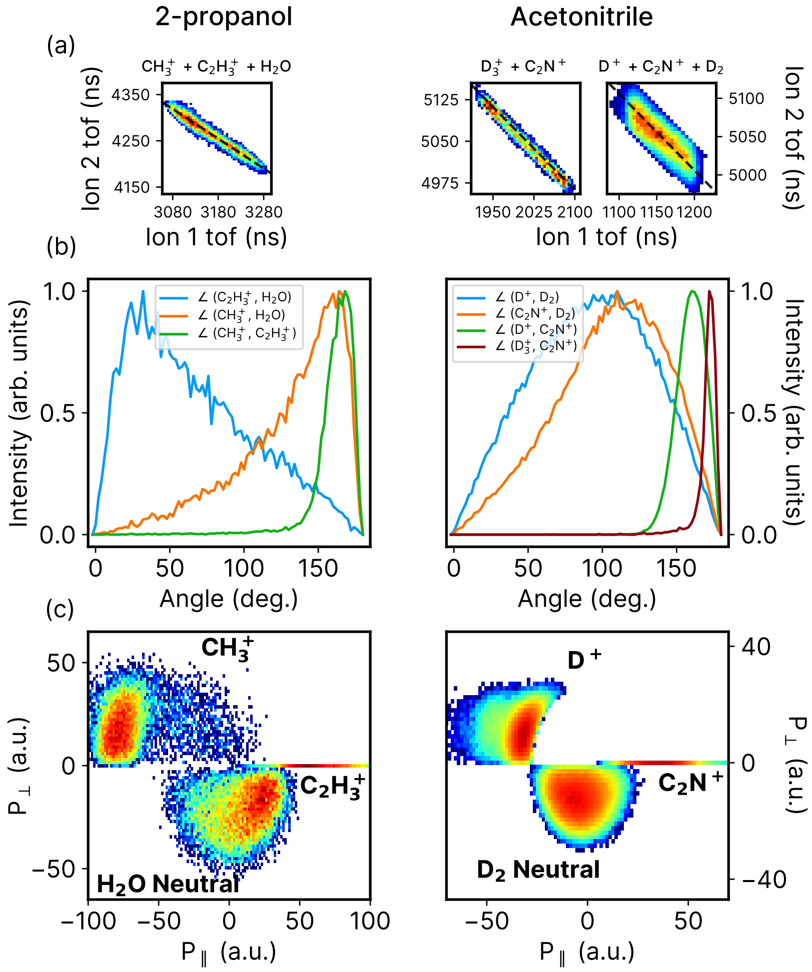

Figure 4.12: (a) Incomplete PIPICO channel for CH_3^+ + H_2O neutral + $C_2H_3^+$ from 2-propanol integrated over the first 200 fs. A black dashed line of slope -0.643 is overlaid on the PIPICO channel to show the agreement between the calculated slope and experimental coincidence channel. (b) Angular distributions between the momentum vectors of $C_2H_3^+$ and H_2O (blue line), CH_3^+ and H_2O (orange line), CH_3^+ and $C_2H_3^+$ (green line) within the first 200 fs time-delay window. (c) Newton plot for the channel CH_3^+ + $C_2H_3^+$ + H_2O neutral integrated over the first 200 fs of pump-probe delay. The momentum vector of $C_2H_3^+$ lies along the x-axis while those of CH_3^+ and H_2O neutral are plotted in the top and bottom halves, respectively. Fig. 4 from the main text is shown in the right column for comparison to D_2 neutral roaming dynamics in acetonitrile.

Additionally, Fig. 4.12 (c) shows the Newton diagram for this channel over the first 200 fs pump-probe delay window. Here, the momentum vector of $C_2H_3^+$ is fixed along the x-axis, while those of CH_3^+ and the reconstructed H_2O are plotted on the top and bottom halves, respectively. Although the ionic fragments, $C_2H_3^+$ and CH_3^+, share similar characteristics to their counterparts in deuterated acetonitrile (shown in the right column of Fig. 4.12), the neutral fragments are significantly different. Specifically, the reconstructed momentum of neutral H_2O is strongly directed towards $C_2H_3{}^+$, which fully supports that H_2O is produced through a secondary decay from $C_2H_5O^+$. On the other hand, the reconstructed momentum of neutral D_2 displays no such preferential angularity and has a broad distribution centered at low momentum.

Conclusion

In conclusion, we have developed a direct means to image neutral roaming reactions in small molecular systems. Using ultrafast IR pump-IR probe spectroscopy combined with coincident Coulomb explosion imaging, we have time-resolved the formation of $H_3{}^+$ from neutral H_2 roaming in acetonitrile, which was measured to occur within a few hundred femtoseconds. This technique enables us to directly track the 'invisible' neutral roamer, the precursor to $H_3{}^+$ formation, from incomplete fragmentation channels. Additionally, with the aid of quantum chemistry calculations, we have fully simulated the possible roaming trajectories, allowing us to follow some of the unique intramolecular processes that occur in this type of dissociation. Our novel technique gives us a more straightforward means to observe neutral fragments which can allow us to gain a better understanding of the underlying molecular dynamics in roaming reactions. More generally, this provides a means to characterize neutral fragmentation processes, which are typically not possible with conventional spectroscopic techniques. This chapter is based on work that was done in collaboration with Aaron LaForge, Sergio Díaz-Tendero, Fernando Martín, and Nora Berrah and is currently under review with Nature Communications.

Chapter 5

XUV-induced fragmentation dynamics in C_{60}

5.1 Introduction

Short-wavelength free-electron lasers (FELs) are ideal for investigating light-matter interactions due to their high intensity and ultrashort pulse duration. These unique attributes are used in a broad field of scientific investigation, including atomic, molecular, and optical physics, condensed matter physics, matter in extreme conditions, materials science, chemistry, and biology [148, 149]. Furthermore, FELs have revealed a variety of nonlinear phenomena in the X-ray and XUV regimes, when intense short-wavelength pulses interact with atoms and molecules [150, 151]. In more complex, larger systems, the absorption of multiple photons leads to the system becoming highly excited or ionized within a few femtoseconds. In that state, numerous interatomic processes offer a means for redistribution of energy throughout the system via various relaxation mechanisms. However, it is quite challenging to decipher the relaxation dynamics and the underlying mechanisms for complex highly excited systems, both experimentally as well as from simulations.

Fullerenes are an ideal molecular system that allow for the investigation of energy redistribution upon photoexcitation [152–159]. C_{60} is a prototype for large finite systems, acting as an ideal intermediate between molecules and semiconductor surfaces for studying the dynamic behavior of large systems when exposed to intense radiation [152]. C_{60} has 240 valence electrons, forming 60 delocalized π bonds, thereby constituting an extended pi system with unique electronic properties, such as the phenomenon of 'giant resonance' [160]. This giant plasmon resonance involves the collective excitation of the loosely bound delocalized pi electrons and can significantly influence the ionization of C_{60} [161]. Notably, C_{60} exhibits both molecular [156] and bulk [157] behavior, making it an excellent testing ground for both experimental and theoretical studies [154, 155, 158]. Furthermore, due to its highly symmetric and compact structure, there is a strong coupling between the electronic and phonon degrees of freedom in C_{60}, which can result in complex relaxation dynamics and phenomena such as delayed ionization and thermionic emission [162]. In particular, multiphoton processes in C_{60} have been extensively studied with strong-field NIR (near infrared) table-top lasers [152, 153, 163–166] as well as with X-ray FELs [154, 155, 167]. Short wavelengths, specifically in the X-ray regime, enable high degrees of ionization and fragmentation through multiphoton absorption, Auger-Meitner decay, and intramolecular interactions. However, a comprehensive understanding of the ionization and consequent energy dissipation mechanisms of C_{60} in the XUV (extreme ultraviolet) regime, which bridges the gap between NIR and X-rays, remains elusive.

In this chapter, we exploit the high absorption cross section at the C_{60} plasmon resonance ($\hbar\omega$=20.7 eV [161]) in the XUV, as shown in Fig. 5.1, to rapidly deposit substantial amount of electronic energy using FEL pulses within a few femtoseconds. This allows us to investigate a previously unexplored excitation regime and temporally map out the subsequent relaxation pathways in C_{60}. For this work, we use single-color pump-probe spectroscopy in combination with a reaction microscope (REMI), also known as COLTRIMS. The first XUV pulse ionizes C_{60} through multiphoton absorption at and around the plasmon resonance while the second XUV pulse probes the induced dynamics. The lighter fragments generated in this process, such as C^{+}, C_2^{+}, and C^{2+} ions, show a delayed dynamic response. This observed delay is due to the highly symmetric and inherently stable structure of C_{60}, which enables a substantial amount of excitation energy to be stored in its numerous nuclear degrees of freedom before eventual fragmentation.

Specifically, in our work, we observe a unique temporal behavior in the C^{2+} fragment ions, a behavior not observed in prior investigations on clusters or larger molecular systems. Our experimental findings for the C^{2+} are effectively explained and reproduced using a simple dynamical model that accurately captures the complex dynamics of the C^{2+} yield resulting from the multiphoton ionization of C_{60}. This underscores the effectiveness of using simple models for understanding the dynamics in complex systems, even under extreme conditions.

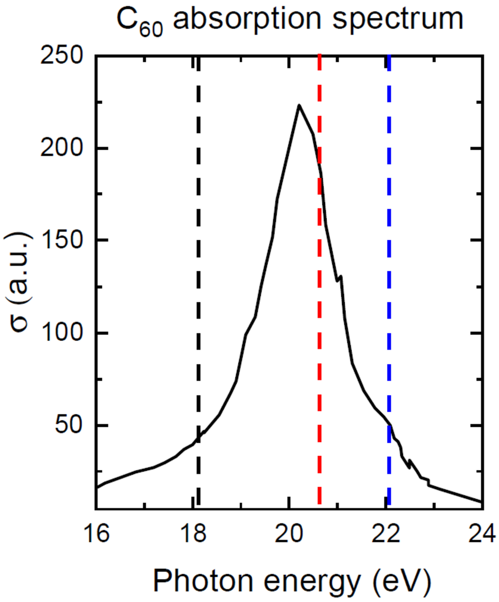

Figure 5.1: Predicted photoionization cross-section of C_{60} as a function of photon energy from simulations, adapted from [168]. The vertical dashed lines correspond to the photon energies (18.1 eV, 20.7 eV, and 22.1 eV) used for the measurements shown in this work.

5.2 FLASH free-electron laser

Free-electron lasers (FELs) are fourth generation synchrotron light sources that are capable of producing extremely bright and short pulses of radiation with laser-like properties in the extreme-ultraviolet (XUV) and X-ray regions of the electromagnetic spectrum. The fundamental principle governing light amplification in a traditional FEL is the resonant coupling between ultra-relativistic electrons and the X-ray radiation they emit. Initially, electrons undergo acceleration to relativistic speeds through linear accelerators and are then guided by a periodic magnetic field produced by a long undulator. An undulator consists of a series of alternating magnets arranged along the path of the electron beam, inducing electron oscillation thereby generating intense radiation. As a consequence of the interaction between electrons and the electromagnetic field, the highly energetic electron beam is modulated in energy. As the electron beam travels further through the undulator, the energy modulation is transformed into spatial modulation, causing the bunching of electrons. This leads to in-phase emission of radiation via these micro-bunches of electrons. FELs can be categorized into two types based on the source of electromagnetic radiation causing microbunching – SASE (self amplified spontaneous emission) FELs [169] and seeded FELs. Seeded FELs use an initial seed laser [170] or a portion of the FEL radiation itself [171] to precisely control the wavelength and characteristics of the generated coherent radiation. SASE FELs, however, leverage the self-amplified spontaneous emission phenomenon, wherein the inherent electron bunching within the electron beam, induced by the interaction with the undulator's periodic magnetic field, serves as the natural source of amplification for generating intense, coherent X-ray radiation, eliminating the need for external seeding mechanisms.

Figure 5.2: Aerial view of the FLASH facility. Adapted from [172].

The XUV free-electron laser FLASH is the first short-wavelength FEL and operates in the SASE mode without requiring an external input signal. The lasing process is triggered via the spontaneous undulator radiation. FLASH2, an extension of FLASH that came into operation in 2016 [173, 174], shares the electron accelerator with FLASH1, but is equipped with its own set of undulators which have variable gaps thus enabling rapid adjustments and extensive scans of the photon wavelength across a wide spectrum. Lasing in the undulator is achieved through SASE, which results in intense FEL pulses with short pulse duration between 10 to 200 fs [172]. However, the trade-off here is limited pulse-to-pulse stability with respect to intensity and spectral properties compared to optical lasers. FLASH2 delivers photon energies in a range from 14 to 310 eV. FLASH generates electron bunches, and hence photon pulses, in a burst mode with patterns consisting of short pulse trains repeating at 10 Hz.

5.3 Experimental methods

The experiment was performed with a REMI endstation [175, 176] at the FLASH FEL in Hamburg, Germany. A REMI can measure the 3D momentum of each detected ion in coincidence. The XUV FEL pulses were delivered with an effective repetition rate of 400 Hz in a burst mode operating at 10 Hz (≈ 40 pulses with 10 μs spacing). The pulse energy was measured upstream by a gas-monitor detector, and for our experiments, we varied the pulse energy from 1 μJ to 5 μJ by changing the gas attenuation. We scanned the photon energy of the FEL pulse from 18 eV to 22 eV by varying the undulator gap. The nominal pulse length was 60 fs and the pulses were focused to approximately $10\,\mu\mathrm{m} \times 10\,\mu\mathrm{m}$ (FWHM) in the interaction region. A collimated beam of C_{60} molecules, oriented perpendicular to the FEL beam, was generated from a resistively-heated oven operating at 600 °C. Upon ionization by the XUV FEL pulses, C_{60} ions and the resulting charged fragments were detected by the REMI [175, 176]. Using a weak and homogeneous electric field, the ions were directed towards a position-sensitive detector. From the time-of-flight (TOF) and the 2D position information, we reconstructed the 3D momentum distributions of the charged particles, which were then converted into mass-resolved kinetic-energy distributions.

5.4 Simulation methods

Our theory collaborators led by Prof. Jan-Michael Rost from Dresden, Germany, calculated the classical molecular dynamics for atoms (ions) and electrons. The active electrons (one per atom) are initially bound to the carbon ions by smoothed Coulomb forces, representing a neutral C_{60}. Additionally, it is essential to account for the covalent forces between the carbon ions. This is achieved by implementing standard empirical short-range two- and three-body forces [177]. Absorption of photons is modeled as a sudden increase in the kinetic energy of an electron, corresponding to the photon energy. Such 'kicks' are exerted over the pulse duration of the FEL. Only the most deeply bound electron is kicked, ensuring that the free electrons do not absorb photons. The subsequent heating and fragmentation dynamics are determined for 1000 realizations, typically extending up to 5 ps. At that point, the kinetic energy of the well-separated fragments is stable, and can be used to calculate kinetic-energy spectra. Similar approaches have previously been applied to study dynamics in clusters [178] and fullerenes [155].

5.5 Results and discussion

The top panel of Fig. 5.3 shows the ion TOF with respect to the detector position. The photon energy of both the XUV pump and probe pulses in this TOF spectrum is 20.7 eV, which corresponds to the peak of the C_{60} plasmon resonance. Both the pump and probe have a pulse energy of 6 μJ. The TOF spectrum shown here is averaged over all pump-probe delays (± 2000 fs). The mass-to-charge ratio, m/q, of the ions is determined from their TOF information. The various lighter fragments such as C^{2+}, C^{+}, C_2^{+} are identified in Fig. 5.3. As can be seen, these ions exhibit a broad distribution with respect to the $X-$ position of the detector,

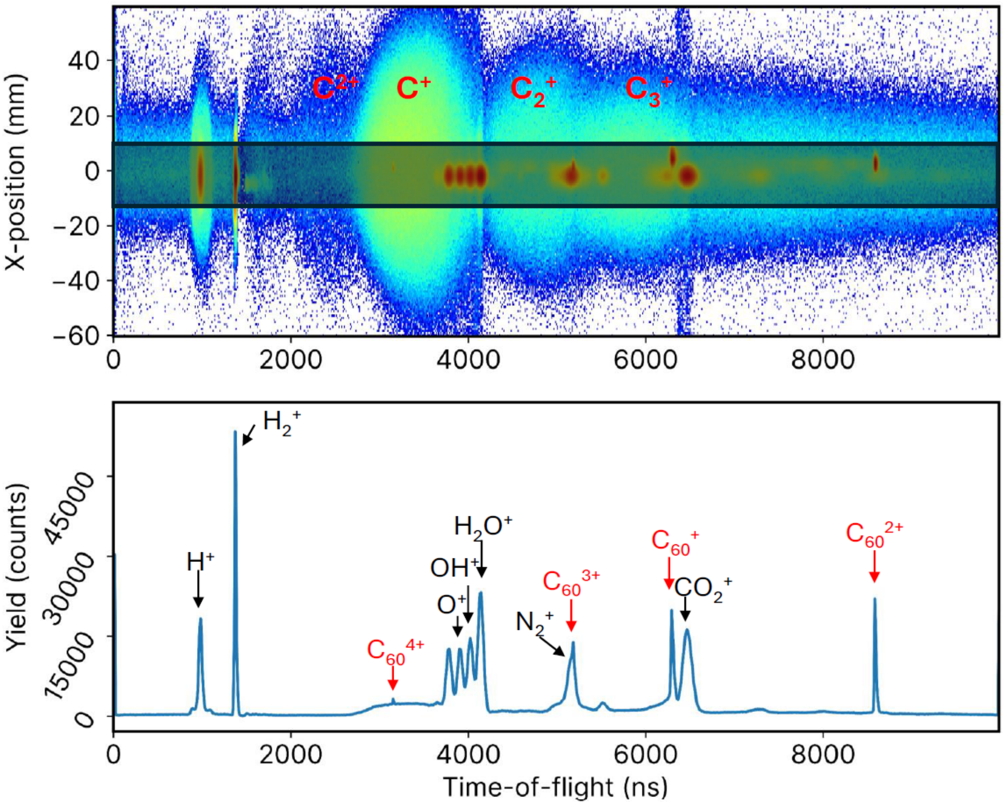

Figure 5.3: Top panel: ion time-of-flight versus detector position. Bottom panel: projection of the gray shaded portion of the top panel. The photon energy is 20.7 eV and the pulse energy was 6 μJ. The data is averaged over all time delays.

which implies that they have a higher spread in momentum and hence, kinetic energy. Aside from such broad distributions, we also observe some very sharp, intense distributions around the $X = 0$ position of the detector. These ions clearly have very small spread in momentum and hence, very low kinetic energy, which implies that they have heavier masses. In order to identify these ions, only the data segment around $X = 0$ position, highlighted by a grey-shaded box, is projected onto the TOF axis and shown in the bottom panel of Fig. 5.3. The parent ions, C_{60}^{n+}, have been labeled in red, while the peaks originating from background gas have been labeled in black. Parent ions being significantly heavier, require a longer TOF than the 10 μs time-window. In the burst mode operation of the FLASH FEL, pulses within each train are separated by 10 μs, which means that the heavier parent ions will not be detected until subsequent FEL pulses. This results in a 'wrapped around' signal. For example, the C_{60}^+ ions are wrapped around 3 time windows while the higher charge states of C_{60} are wrapped around 2 time windows.

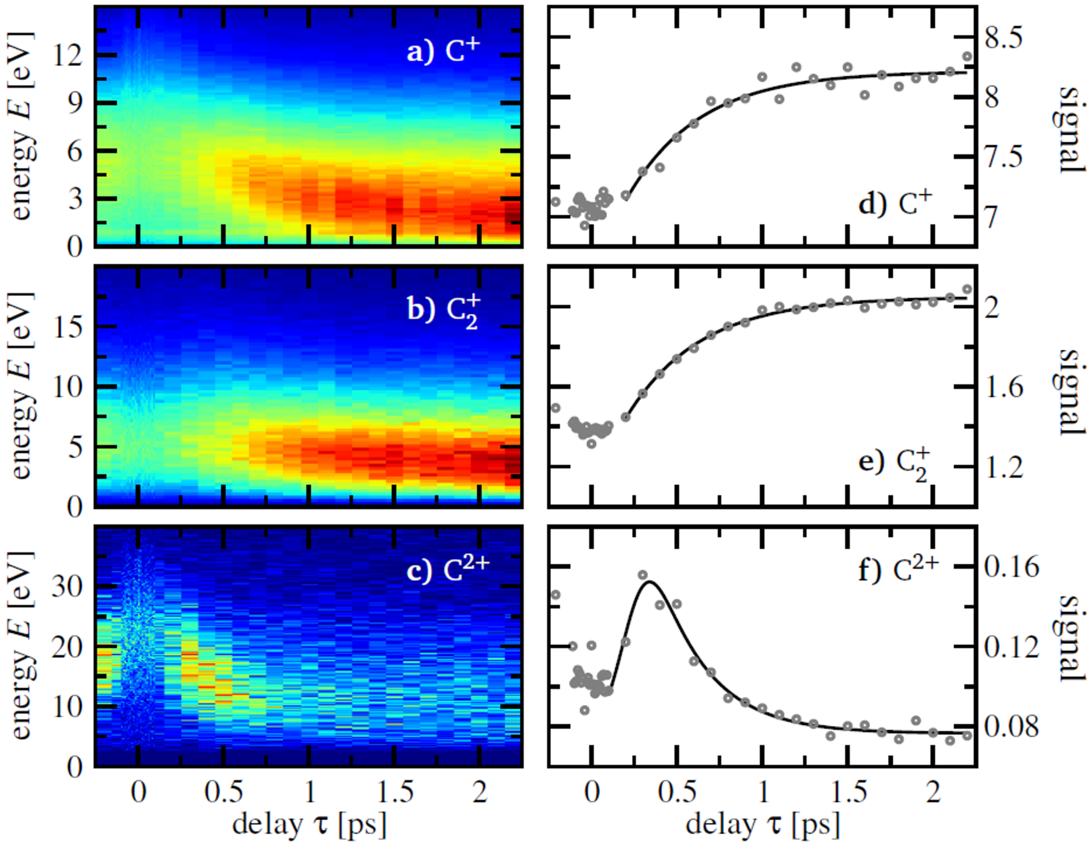

Figure 5.4: (a)-(c) Kinetic energy distributions and (d)-(f) ion yield spectra as a function of pump-probe delay for C^+, C_2^+, and C^{2+}, respectively. The FEL pulse energy is 6 μJ and the photon energy is 20.7 eV.

Fig. 5.4 shows the kinetic energy distributions of the ionic fragments as a function of pump-probe delay for (a) C^+, (b) C_2^+, and (c) and C^{2+}. The pulse energy for both pump and probe was 6 μJ and the photon energy was 20.7 eV, at the peak of the plasmon resonance [161]. Overall, all three ionic fragments show a similar trend in their kinetic energy. Each of the ions shows a decrease in the mean kinetic energy as the pump-probe delay increases, which results from the Coulomb repulsion among the ionic fragments. Notably, the C^{2+} ion has the largest kinetic energy, followed by C^+ and C_2^+. The corresponding signal yields, which are simply the projections of the kinetic energy onto the time-delay axis, are shown in Fig. 5.4 (d) – (f) as a function of pump-probe delay. The C^{2+} yield shows a distinct behavior compared to the monomer and dimer carbon ion fragments. While its yield is initially low near $\tau = 0$ ps, it sharply increases leading to a maximum at short delays, followed by a slower decay at longer pump-probe delays. On the other hand, the yields of C^+ and C_2^+ show a monotonic increase, with the lowest signal intensity at $\tau = 0$ ps. This observed gradual enhancement in signal yield for the monomer and dimer ions is inversely correlated with the yields of the charged parent fullerene ions, which exhibit a gradual time-dependent decrease, as shown in Fig. 5.5. This emphasizes the resistance of the fullerene cage to fragmentation.

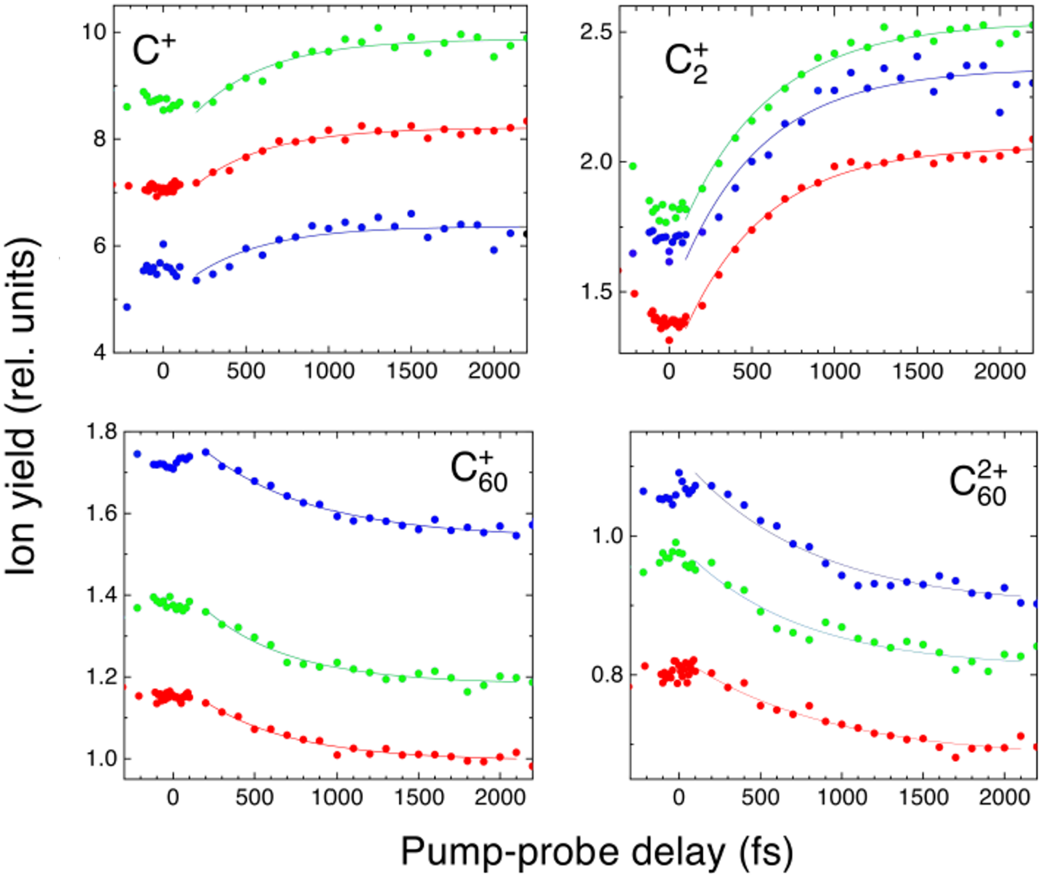

Figure 5.5: Ion yields for C^+, C_2^+, C_{60}^+, and C_{60}^{2+} as a function of pump-probe delay for different photon energies. The pulse energy is kept constant for all photon energies at 6 μJ.

Fig. 5.5 shows the time-dependent ion yields and their fits for C^+, C_2^+, C_{60}^+, and C_{60}^{2+} at photon energies of 18.1 eV (blue), 20.7 eV (red) and 22.1 eV (green). These photon energies scan the plasmon resonance, which occurs at ~ 20.7 eV. The pulse energy of both pump and probe pulses is fixed at 6 μJ for all the photon energies shown here. As previously mentioned, the yield of the charged states of the parent C_{60} ions decreases with increasing pump-probe delay, with highest yield observed at $\tau = 0$ ps. Overall, we see similar time-scales for the time-dependent ion yields as we scan across the plasmon resonance. To characterize and compare the time-dependent dynamics of the ion yields across thse photon energies, we have fitted the ion yield data to a exponential of the form

$$P(t) = \Theta(t - t_0)\left[A + B\exp\left(-(t - t_0)/\tau_s\right)\right] \tag{5.1}$$

where τ_s is the exponential time constant. The values of fitted time constants are shown in Table 5.1 below. The time constants of C_{60}^{n+} are longer than that of the smaller fragments and increase for the higher charge states. On the other hand, the time constants for C^+ and C_2^+ are similar, indicating that these fragments are created in a similar process.

ion	18.1 [eV]	20.7 [eV]	22.1 [eV]
C_{60}^{+}	670 ± 70	556 ± 64	531 ± 70
C_{60}^{2+}	779 ± 124	883 ± 148	713 ± 147
C_2^{+}	510 ± 65	500 ± 25	535 ± 30
C^{+}	437 ± 96	436 ± 39	445 ± 55

Table 5.1: Time constants τ_s for the delay-dependent ion yields shown in Fig 5.5.

Fig. 5.5 reveals that the yield of monomers is significantly higher than that of dimers, despite previous findings that fullerenes primarily dissipate energy by ejecting carbon dimers [166]. The simulations performed by our theory collaborators confirm that dimers are the predominant initial photoproducts. However, in our experiment, the XUV probe pulse further interacts with the ejected dimer ions, resulting in a Coulomb explosion of $C_2^+ \rightarrow C^+ + C^+ + e^-$. This process is supported by fitting the experimentally obtained kinetic energy spectrum of C^+ at different time-delays, to a model that comprises of a linear combination of monomer spectrum from both direct ionization and from Coulomb explosion of the dimer ions. As shown in Fig. 5.6 for different time-delays, the contributions from these two sources of carbon monomer yield vary with time. Overall, the primary contribution to the monomer yield arises from the Coulomb explosion of dimers. This finding is consistent with our observations of similar rise-times in the delay-dependent ion yields for C^+ and C_2^+, as seen in Fig. 5.5.

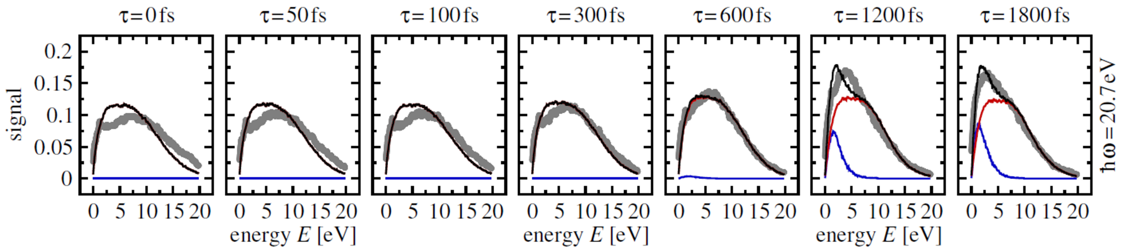

Figure 5.6: Carbon monomer energy spectrum at various time-delays: data from experiment (gray) compared to the simulated sum (black) of direct release of monomers from C_{60} (blue) and Coulomb explosion of dimers (red), shown for on-resonance photon energy 20.7 eV.

The C^{2+} fragment shows the most unexpected and distinctive dynamics compared to the other carbon fragments, which requires further investigation. In the time-dependent analysis, C^{2+} yield shows a sharp peak at a few hundred femtoseconds as shown in Fig. 5.4 (f). This peak occurs on a timescale which is significantly shorter than the typical picosecond-scale fragmentation processes, but also much longer than the FEL pulse length of $\sim$ 60 fs. Additionally, we observe a shift in the peak of the C^{2+} yield to larger time-delay values as the photon energy increases from 18 eV to 22 eV, as shown in Fig. 5.7.

The maximum in the C^{2+} yield observed in our experiments indirectly indicates the radial dependence of the global positive nanoplasma potential within the charged fullerene, which we discuss further below. Initially, the carbon cage remains relatively intact for the first few hundred femtoseconds, despite absorbing a large number of XUV photons. We estimate about 50 photons are absorbed from a simple calculation using the experimental FEL beam parameters and the neutral C_{60} absorption cross section on the plasmon resonance ($\approx$ 500 Mbarn [168]). However, once the first four to five electrons are ejected, the fullerene develops a

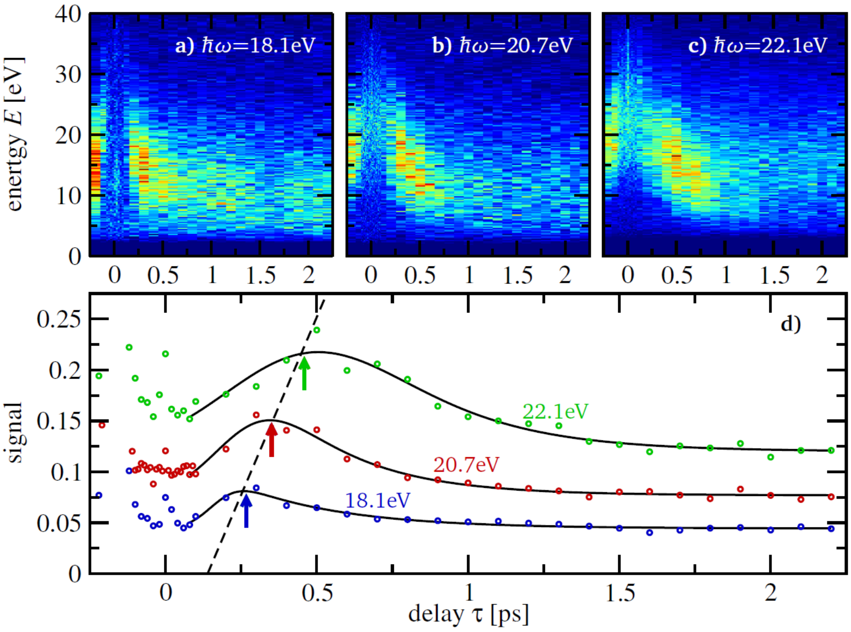

Figure 5.7: (a) - (c) Delay-dependent kinetic energy distribution of C^{2+} for different photon energies. (d) Corresponding ion yields, shown in circles and empirical fits (solid lines). The black-dashed line tracks the shift of the maxima in yield to guide the eye.

positive charge, creating a strong electrostatic potential around it. This positive background potential becomes sufficiently deep to trap subsequent photoelectrons, leading to the formation a nanoplasma [179, 180] – a dense, positively charged cloud of ions and electrons. This stabilizes the multiply ionized complex, a phenomenon similar to that observed in clusters exposed to intense IR pulses [178, 181, 182]. This nanoplasma develops rapidly during the laser pulse and if the resulting trapping potential, which is almost spherical, is sufficiently deep and its slope near the radius of the fullerene is steep, it facilitates electric field-assisted photoionization (FAI) of C^+ ions. The presence of this background potential from the fullerene nanoplasma effectively lowers the ionization energy required to remove an additional electron from C^+, leading to the formation of C^{2+}. This ionization of C^+, which would otherwise be impossible due to inadequate photon energies for direct ionization, is schematically represented in Figure 5.8.

While the nanoplasma potential builds up during the laser pulse (∼ 60 fs), the production of C^{2+} ions is notably slower. This is due to the delayed formation of C^+ ions from the fullerene cage which is resistant to fragmentation. On the other hand,

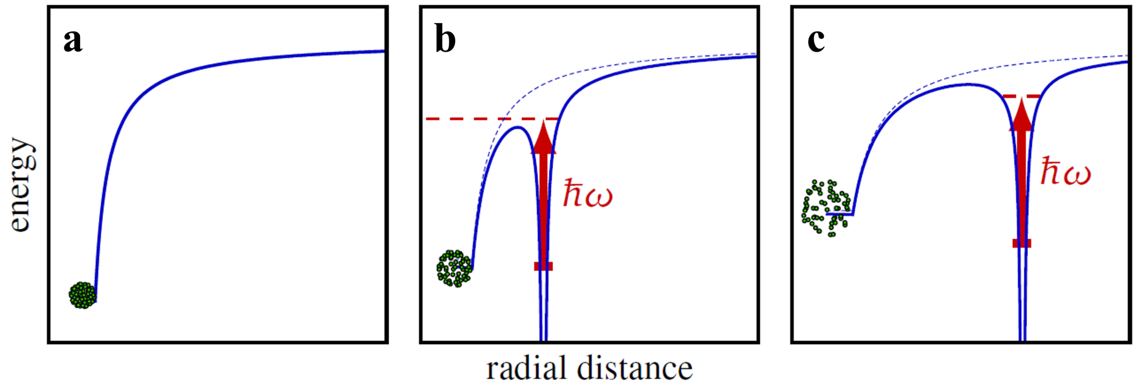

Figure 5.8: Snapshots for increasing time of the attractive potential seen by the (plasma) electrons as a function of distance from the fullerene center: (a) before a carbon monomer is released from the C_{60} cage, (b) with a C^{+} ion at a suitable distance for field-assisted ionization (FAI) to create C^{2+}, and (c) with C^{+} at a distance such that the background potential is too weak for FAI.

over longer timescales, the monomers move further from the fullerene to regions where the nanoplasma potential is too weak to support FAI. Therefore, there exists an optimal intermediate delay during which the second pulse can efficiently produce C^{2+} via FAI.

Clearly, the C^{2+} yield results from a complex interplay between molecular fragmentation forces, which lead to the ejection of lighter ions, and the electrostatic forces of the carbon monomer ion combined with the background potential of the nanoplasma. This dynamic interaction between Coulombic and molecular forces is evident from the photon energy dependence of the experimental C^2+ yields, as shown in Fig. 5.7. Generally, at equivalent pulse energies, a higher photon energy results in a deeper nanoplasma potential, enhancing the efficiency of FAI even when the fragmented ions are spatially further away from the fullerene center. As a result, the peak in the C^{2+} yield is shifted to longer pump-probe delays for higher photon energies. Moreover, a higher photon energy also leads to more effective ionization of carbon fragments, which should increase the overall C^{2+} yields. The experimental results confirm both of these outcomes, demonstrating both a shift in the yield maximum towards longer pump-probe delays as well as higher overall yields at increased photon energies, as shown in 5.7.

After analyzing the time-dependent dynamics and yields of fragmentation products, we can now examine the underlying role of the plasmon resonance, which mainly facilitates the highly efficient energy absorption. This influence, though subtle, has a consistent effect on the measured observables. The primary carriers of the absorbed energy are the dimer and parent ions, which can easily further decay into other channels. Therefore their yield is the lowest at the on-resonance energy (20.7 eV), compared to all other explored photon energies, as seen in Fig. 5.5. In contrast, the yields of the other two fragments we measured, C^+ and C^{2+}, are primarily influenced by the absorption of additional photons not via the plasmon resonance. Specifically, the singly-charged carbon ions are produced through Coulomb explosion of dimers, while the doubly-charged carbon ions are a result of field-assisted photoionization of C^+. Consequently, the delay-dependent yields of both these ions increase with photon energy, as can be seen in Fig. 5.5 and Fig. 5.7.

5.6 Conclusion

In conclusion, we have explored the relaxation and fragmentation dynamics of gas-phase C_{60} using intense, ultrashort FEL pulses in a single-color XUV-pump XUV-probe setup, paired with a reaction microscope. The temporal and kinetic energy dynamics of both light and heavy ionic fragments reveal the complex interplay between Coulombic and molecular forces following intense energy absorption over ultrashort timescales which is facilitated by the giant plasmon resonance. Furthermore, our theoretical analysis reveals a transient nanoplasma state, essential for understanding the unique time delay-dependent behavior of the C^{2+} ion yield. These mechanisms are crucial in scenarios where significant energy is rapidly deposited into large molecular systems, offering insights particularly relevant for large heterogeneous systems where efficient energy redistribution to lighter fragments is critical. This chapter is based on work that was done in collaboration with Aaron LaForge, Ulf Saalmann, Razib Obaid, Shashank Pathak, Hannes Lindenblatt, Severin Meister, Florian Trost, Philipp Rosenberger, Rupert

Michiels, Shubhadeep Biswas, Krishna Saraswathula, Frank Stienkemeier, Francesca Calegari, Markus Braune, Marcel Mudrich, Matthias Kling, Daniel Rolles, Edwin Kukk, Thomas Pfeifer, Jan-Michael Rost, Robert Moshammer, and Nora Berrah and is currently under review with Physical Review Letters.

Chapter 6

Structural imaging with ultrafast electron diffraction

6.1 Introduction

Ultrafast electron diffraction (UED) in the gas phase is a cutting-edge technique that enables the direct determination of time-dependent structural transitions in isolated molecules with subangstrom and femtosecond resolution in space and time [183, 184]. Unlike optical spectroscopy, where the probe is tuned to specific transitions in the molecule, the electron probe in UED is sensitive to all species in its path and can hence reveal all the intermediate structures. This is achieved by analyzing the interference patterns of the electron waves scattering off all atoms and atom-atom pairs in the molecular sample. These patterns are recorded on a detector to obtain information about the internuclear distances within molecular structures. Furthermore, UED can track the structural dynamics of reactions at relevant time scales for all structures that are formed after photoexcitation [9, 185, 186]. The strong interaction of electrons with matter results in a short penetration depth, making UED particularly useful for the characterization of surfaces, thin samples, and gases [187].

The origins of gas-phase electron diffraction can be traced back to 1930, marked by the pioneering work by Mark and Wierl [188, 189], which was subsequently advanced by the work of Brockway and Pauling [190, 191]. The field saw significant progress in the late 1990s with Zewail's experiments to determine the structures of molecules with femtosecond temporal resolution using UED [1]. Additionally, several studies on gas-phase electron diffraction have described electron scattering with different levels of detail [192–196]. By interfacing a

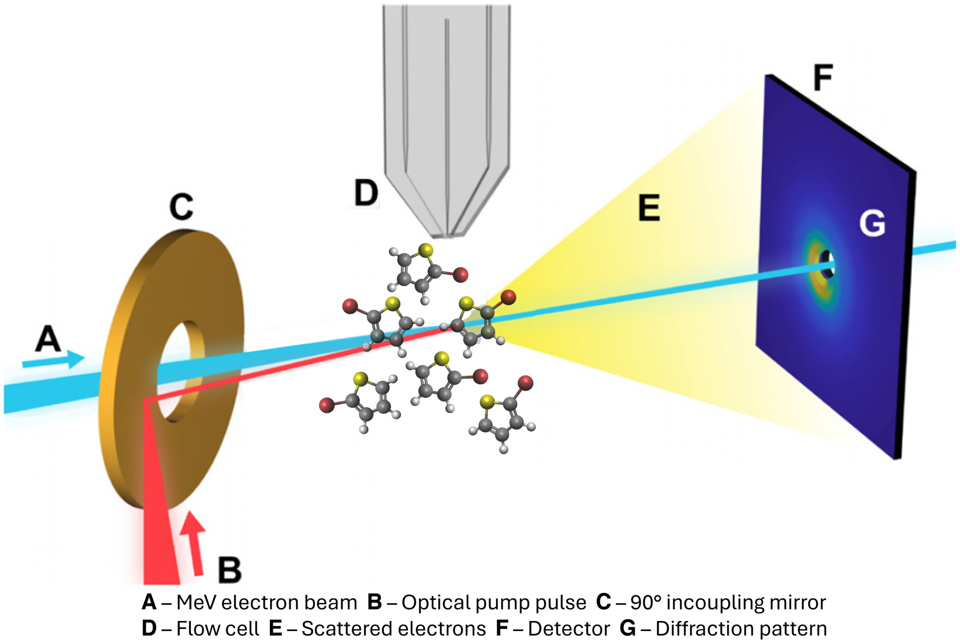

Figure 6.1: Schematic representation of the gas-phase MeV UED experimental setup at SLAC National Accelerator Laboratory. The figure is adapted from [200].

gas-phase electron diffraction instrument with an ultrafast pulsed laser system for electron pulse generation and sample excitation in a pump-probe scheme, current state of the art experiments can spatially and temporally track all structures that are formed after photoexcitation [197–199]. A schematic of the experimental set up for UED is shown in Fig. 6.1.

Typically, small organic molecules exhibit strong absorption in the ultraviolet spectrum, which initiates a wide array of photophysical processes with the goal of finding efficient electronic relaxation pathways [183, 201–205]. These intricate processes, particularly in cyclic molecules, often involve nuclear motions such as out-of-plane structural distortions, leading to significant molecular rearrangement through ring-opening reactions. These mechanisms are critical in synthetic organic chemistry and naturally-occurring processes alike, underscoring their fundamental importance in ultrafast photochemistry. For instance, ring-opening and closing reactions are interesting candidates for mechanical molecular motors [206], and have been used as building blocks of molecular logic gates [207] and molecular memory devices [208]. Furthermore, the photoinduced ring-opening of

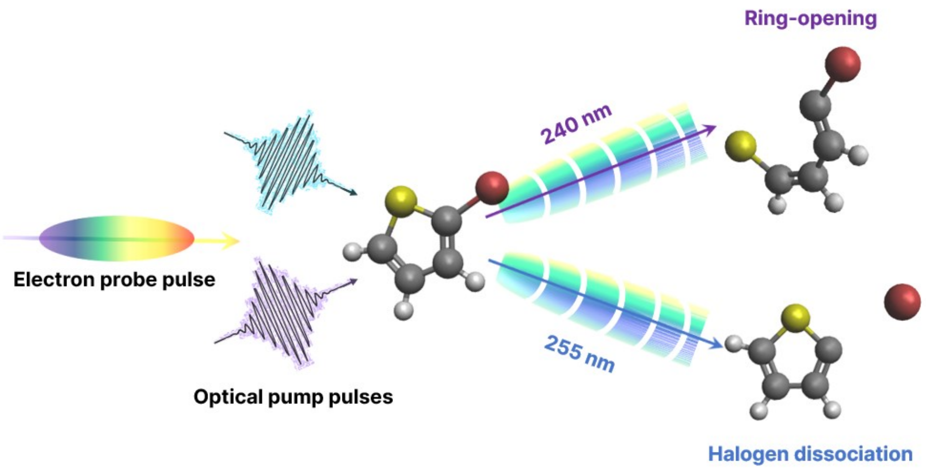

Figure 6.2: Schematic of our experiment. To investigate the wavelength-dependent dynamics initiated in 2-Bromothiophene, the molecule is excited at two different wavelengths, 240 nm and 255 nm. The time-resolved dynamics induced by each of these pump-pulses is probed in a time-resolved manner using an ultrafast electron pulse and the scattered signal reveals the geometry of the evolving molecular structure.

1,3-cyclohexadiene plays a crucial role in the biosynthesis of vitamin D_3 [202, 209], exemplifying the importance of these reactions in both technological and biological applications. As a result, it is important to identify the systems that exhibit characteristic ring-opening reactions and to understand how these pathways interact with other photochemical processes.

Upon molecular excitation, multiple relaxation pathways can be energetically open, initiating a competition between the different photochemical processes. Depending on their relative efficiencies and wavelength of excitation, the branching ratios among the different channels can vary dramatically. In this chapter, we use UED to study the reaction dynamics of 2-Bromothiophene, (C_4H_3SBr), with a particular focus on how the excitation wavelength can influence the competition between ring-opening and bond dissociation. This study not only sheds light on the complex interplay between electronic and nuclear dynamics, but also demonstrates the capability to manipulate and control molecular reactions with tunable UV lasers. Our experimental results, aided by state-of-the-art theoretical analysis, reveal that the excitation wavelength can significantly affect the reaction channels in a photochemical process. Beyond advancing our understanding of molecular dynamics on femtosecond timescales, this work provides a blueprint for manipulating molecular systems with light. Its implications range from the development of novel photoresponsive materials to the precise control of photochemical synthesis. A schematic of the experiment, showing the investigation of wavelength-dependent dynamics in 2-Bromothiophene using UED, is shown in Fig. 6.2.

6.2 Basic theory of gas-phase electron diffraction

The electron scattering intensity is typically represented as a function of s, the magnitude of momentum transfer between an incident electron and an elastically scattered electron, which is expressed as

$$s = \frac{4\pi}{\lambda} \sin\left(\frac{\theta}{2}\right) \tag{6.1}$$

where λ is the de Broglie wavelength of the electrons which is 0.3 pm in the case of 3.7 MeV electron beam used in this experiment, and θ is scattering angle. The experimentally available momentum transfer range is s = 0.5–10 Å^{-1} which determines the spatial resolution based on the inverse relationship between s and real-space distances, $2\pi/s_{max} = 0.6$ Å.

The total scattering intensity, I, is a sum of atomic ($\mathrm{I_A}$, contributions from individual atoms) and molecular scattering ($\mathrm{I_M}$, interference terms from all atom-atom pairs).

$$I(s) = I_{\mathrm{A}}(s) + I_{\mathrm{M}}(s) \tag{6.2}$$

The independent atom model (IAM) assumes that the electronic potentials of each atom in a molecule are independent and hence, the atomic scattering intensity can be expressed as the sum of elastic and inelastic scattering contributions [210]

$$I_{\mathrm{A}}(s) = C\sum_{n=1}^{N}\left(|f_i(s)|^2 + 4\frac{S_i(s)}{a_0^2 s^4}\right) \tag{6.3}$$

where f_i and S_i are the elastic and inelastic scattering amplitudes for atoms i, respectively, N is the number of atoms in the molecule, a_0 is the Bohr radius, and C is the proportionality constant.

$\mathrm{I_M}$ is the relevant term for structural determination, since it is a superposition of intensities from all the atom pairs in a molecule, and is expressed as [210]

$$I_{\mathrm{M}}(s) = C\sum_{n=1}^{N}\sum_{j\neq i}^{N}|f_i||f_j|\exp\left(-\frac{1}{2}l_{ij}^2 s^2\right)\cos\left(\eta_i - \eta_j\right)\frac{\sin(sr_{ij})}{sr_{ij}} \tag{6.4}$$

where f_i and η_i are the elastic scattering amplitude and corresponding phase for the $\mathrm{i^{th}}$ atom, r_{ij} is the distance between the $\mathrm{i^{th}}$ and $\mathrm{j^{th}}$ atom, l_{ij} is the vibrational amplitude and C is the proportionality constant. The scattering factors f and η depend on λ, s and atomic number Z and can be obtained from literature [211]. The elastic scattering amplitude, f, scales as Z/s^2, while $\mathrm{I_A}(s)$ decays as $1/s^5$. Hence, in order to highlight the oscillatory behavior of the diffraction signal, a modified molecular scattering intensity, $\mathrm{sM}(s)$, is used and is defined as

$$sM(s) = s\frac{I_{\mathrm{M}}(s)}{I_{\mathrm{A}}(s)} \tag{6.5}$$

The modified molecular scattering intensities in momentum-space can be transformed into the pair distribution function (PDF) in real space, which allows for a more intuitive understanding of the molecular structure and how it changes. We can obtain the PDF by taking the sine transform of $\mathrm{sM}(s)$,

$$PDF(r) = \int_0^{s_{\max}} sM(s)\sin(sr)\exp\bigl(-ks^2\bigr)ds \tag{6.6}$$

where k is a damping constant used to reduce the oscillations caused by the finite s range of signal.

6.3 Experiment

A schematic of the experimental set up is shown in Fig. 6.1. The experimental setup and instruments are described in detail in earlier studies [11, 212]. Below is a brief description of the experimental parameters used for our experiment on 2-Bromothiophene. The third harmonic of the 800 nm output of a Ti:sapphire laser system is used to produce electron bunches that are accelerated to a kinetic energy of 3.7 MeV at a repetition rate of 360 Hz. Pump pulses were generated using an optical parametric amplifier. The two different wavelengths, 240 ± 2 nm and 255 ± 2 nm were generate with 15 μJ and 62 μJ intensities, respectively. The pump pulses are focused into the experimental chamber to a diameter of 240 μm full-width at half-maximum and overlapped with the electron beam. The time-delay between the optical pump and the electron probe pulses are varied using a delay stage in the pump path. The electron beam had a typical pulse duration of 150 fs for low bunch- charge and 500-1000 fs for high bunch-charge. The temporal resolution of the experiment is estimated to be ∼150 fs. 2-Bromothiophene from a heated flow cell, with an opening of 200μm, was injected into the interaction region. Diffracted electrons are detected on a phosphor screen which is imaged by an electron multiplying charge coupled device (EMCCD) camera. The phosphor screen has a hole in the center in order to transmit the undiffracted electron beam as well as the optical pulses, which sets a limit on the minimum observable momentum transfer at 0.5Å^{-1}. The maximum momentum transfer is 10Å^{-1}, limited by signal-to-noise ratio. The analysis procedure and results are discussed in more details in sections 6.5 and 6.6, respectively.

6.4 Simulation methods

Ab initio molecular dynamics (AIMD) simulations were carried out by our collaborators, Todd Martinez (Stanford, US) and Nanna Holmgaard List (KTH, Sweden), to model the relaxation of 2-Bromothiophene following photoexcitation with 240 and 255 nm pump wavelengths. Initial nuclear positions and momenta were obtained via sampling from the ground state vibrational wavefunction within the harmonic approximation. Pump wavelength effects were incorporated via two independent sets of AIMD simulations that utilize initial nuclear geometries with computed UV absorption resonant with the 240 and 255 nm pump wavelengths. This was achieved through weighting with Gaussians centered at the corresponding band center energies (5.17 and 4.86 eV respectively) and a standard deviation of 0.02 eV (corresponding to a FWHM of 2 nm).

The initial dynamics following photoexcitation was simulated with the equation of motion coupled cluster singles and doubles (EOM-CCSD [213]), utilizing Tully's fewest switches surface hopping (FSSH [214]) approach for describing nonadiabatic population transfer between different singlet electronic states. This EOM-CCSD/FSSH approach predicted the onset of either C-S or C-Br bond cleavage within 300 fs, leading to a reduced gap between the ground (S_0) and first excited (S_1) singlet states. However, the linear-response EOM-CCSD approach cannot correctly describe regions of the potential energy surface where the S_1 and S_0 states become nearly degenerate [215]. We consequently simulated longer time dynamics of the biradical(oid) species resulting from bond cleavage with ground state unrestricted density functional theory (DFT) calculations utilizing the ωB97X-D3 functional [216]. Specifically, we switched from EOM-CCSD to DFT when the computed EOM-CCSD excitation energy of the S_1 state dropped below 0.75 eV in the dynamics simulations, with the ground state unrestricted DFT AIMD simulations being initiated with the EOM-CCSD level nuclear geometry and momenta at this time point. Two sets of unrestricted DFT calculations were performed for each probe wavelength, corresponding to singlet (i.e. equal numbers of up and down spin electrons) and triplet (two more up spin electrons than down spin) multiplicities. This is expected to encapsulate all possible behavior in the biradical(oid) broken bond regime and potentially reveal signatures for any intersystem crossing phenomenon. All electronic structure calculations utilized the

Q-Chem software package [217] and the cc-pVDZ basis set [218–220]. Further details about the calculations are provided in the supporting information.

6.5 Data analysis

The 2D diffraction patterns recorded at the EMCCD detector were processed into 1D scattering intensity curves, I(s), using the following steps. First, pixels with intensities 4 standard deviations above the mean of identical pixels across time-delay and detector coordinates were removed and then the diffraction patterns that were acquired at the same delay were averaged. A background signal, estimated by linearly interpolating between the intensities of the four corners of the average image frame, was subtracted from all the images. Subsequently, masks were applied to all the detector areas which do not image the phosphor screen, such as the hole at the center of the detector through which the electron beam passes as well as the edges. Next, in order to reduce the 2D diffraction images to 1D scattering intensity curves, the center of each diffraction image was determined by fitting circles to pixels with identical intensities and outliers (pixels with intensities above 3 standard deviations from the mean) were removed. Then, these cleaned up 2D images were radially averaged around the diffraction pattern center to produce the 1D scattering curves for each delay point.

The experimentally obtained and simulated scattering intensity curves in the momentum space for the ground state 2-Bromothiophene structure are shown in blue and red, respectively, in Fig. 6.3 (a). The simulated scattering curve is obtained by implementing IAM on an optimized ground state geometry of 2-Bromothiophene and it agrees quite well to the experimentally obtained curve. Both experimental and simulated signals are then sine-transformed to get the pair-distribution curve in the real space as shown in Fig. 6.3 (b). The peaks in the PDF curve are assigned color-coded vertical sticks that correspond to the unique average inter-atomic distances between any two atom pairs of 2-Bromothiophene shown in Fig. 6.3 (c). For instance, the distance between Br and S atoms in the

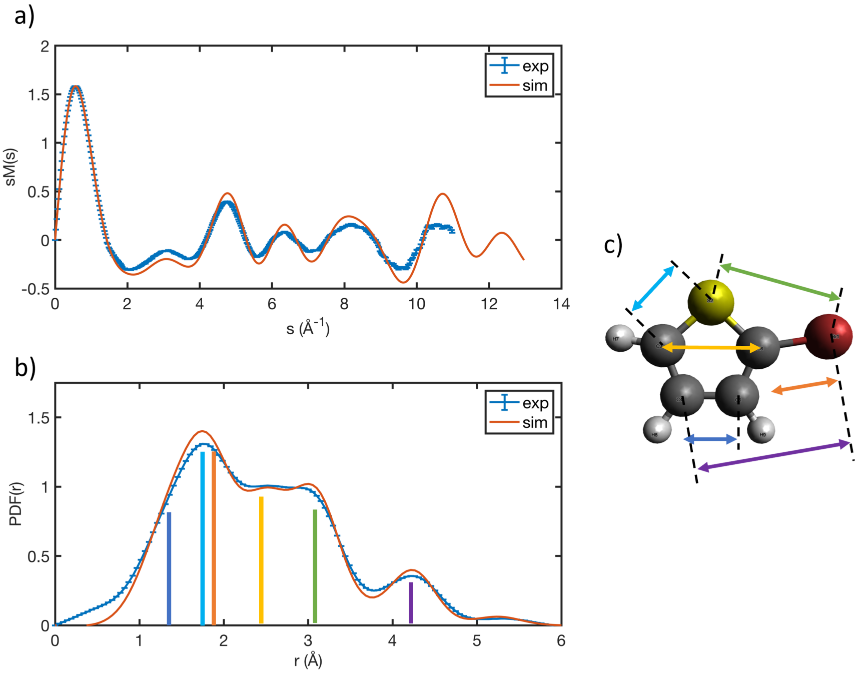

Figure 6.3: (a) Comparison between experimentally obtained and simulated ground state static diffraction signal for 2-Bromothiophene in the momentum space. (b), comparison in real space. The colored lines indicate the interatomic distances visualized in the ground state structure of 2-Bromothiophene, shown in (c).

ground state structure of this molecule is 3 Å, which is represented by the peak corresponding to the green stick in Fig. 6.3 (b).

To track the structural changes that occur after photoexcitation, we recorded a series of averaged 2D diffraction images at varying time delays between the laser pump pulse and the electron probe pulse. The fraction of molecules that are excited by the laser pulse is generally less than 10%, which means that the time-dependent signal is dominated by the parent molecules. Furthermore, the molecular scattering intensity from a reaction fragment is usually weaker than that from a parent molecule because of fewer internuclear pairs. Therefore, to extract the contribution of photoproducts to the diffraction signal, the 'difference-diffraction' method [210] is used, where we use a reference image of the ground state structure of the molecule to obtain the diffraction-difference signal $\Delta I(s,t)$. The images taken at negative time-delays where the electron beam

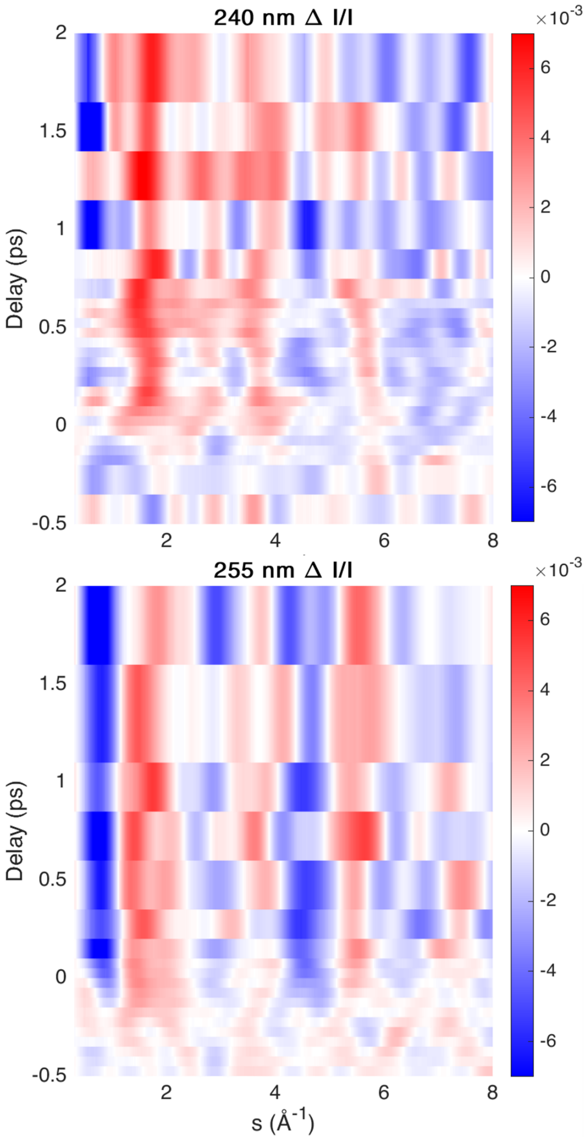

Figure 6.4: Comparison of the experimentally obtained delay-dependent ΔI/I between excitation wavelengths of 240 nm and 255 nm.

precedes the laser excitation pulse serve as the reference. Therefore, the experimental difference-diffraction signal is given by:

$$\Delta I/I(s;t) = \frac{I(s;t) - I(s;t<0)}{I(s;t<0)} \tag{6.7}$$

where $I(s;t)$ is the radially averaged diffraction intensity at any pump-probe delay time, t, and $I(s;t<0)$ is a reference pattern taken before the arrival of the pump laser and is shown in Fig. 6.4. The experimental time-dependent difference pair distribution function, $\Delta\mathrm{PDF}(r,t)$, shown in Fig. 6.5, was calculated using the sine-transform of the time-dependent difference modified scattering curves, ΔsM(s,t):

$$\Delta sM_{\text{exp}}(s,t) = \frac{I(s,t) - I(s,t<0)}{I_{\text{at}}(s)} s \tag{6.8}$$

$$\Delta PDF(r,t) = \int_0^{s_{max}} \Delta sM_{\text{exp}}(s,t) \sin(sr) \exp(-ks^2) ds \tag{6.9}$$

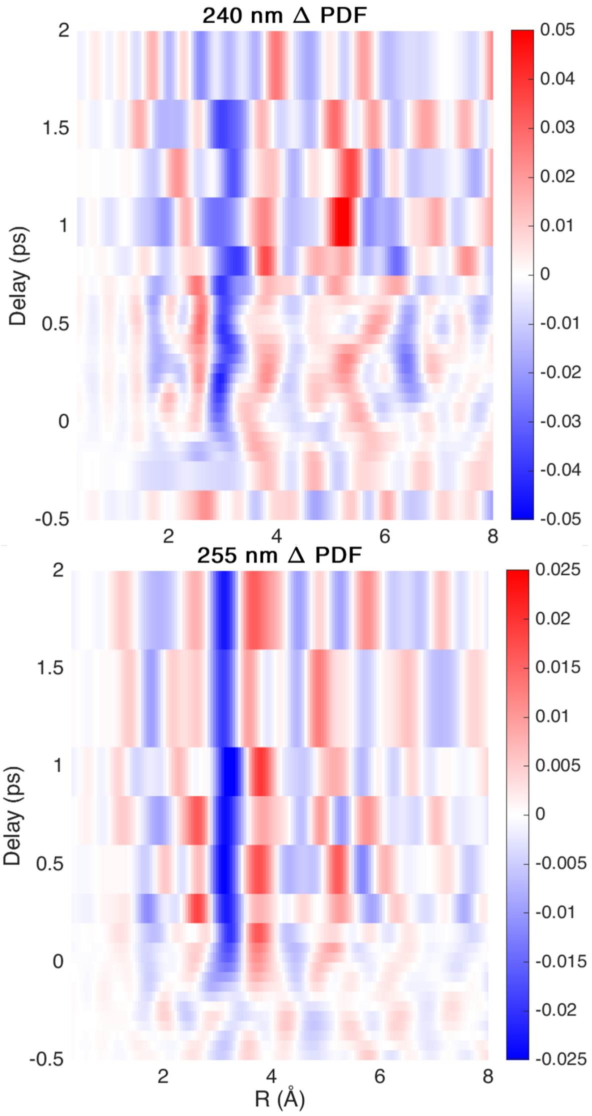

Figure 6.5: Comparison of the experimentally obtained delay-dependent ΔPDF between excitation wavelengths of 240 nm and 255 nm.

The ΔPDF(r,t) maps shown above following either 240 nm or 255 nm photoexcitation of 2-Bromothiophene at pump-probe delays up to 2 ps reveal an obvious decrease in the most intense features of the parent static PDF (Fig. 6.3 (b)). Specifically, we see a loss in signal intensity at distances corresponding to 1.7 Å, 3 Å, and 4.5 Å in Fig. 6.5 which correspond to distance between the different Br-C atoms and the Br-S atoms at positive time-delays. This implies that the structure of the molecule does change significantly upon photoexcitation. A detailed analysis to distinguish between the competing processes that contribute to the observed structural changes at both the wavelengths is given in section 6.6 below.

The statistical uncertainty of the experimental signal was estimated using a standard bootstrapping analysis. The UED dataset for each excitation wavelength was randomly resampled with replacement 150 times to generate 150 bootstrapped datasets. Each bootstrap dataset was analyzed identically and separately, which allowed us to calculate the mean and standard deviation for all the relevant analysis outputs, such as the time-averaged scattering intensity or Δ PDF curves.

6.6 Results and discussion

Quantifying the competition between bromine dissociation (Br-Diss) and ring-opening (RO) dynamics in 2-Bromothiophene is integral in understanding its photochemical behavior. Initially, our strategy was to implement the IAM to simulate these process, using simple geometrical models for both Br-Diss and RO. However, the simulated signals with a more simplistic model for these two competing processes yielded significant overlap, thus complicating the determination of their respective branching ratios. Moreover, such rudimentary models cannot capture the nuances of wavelength-dependent dynamics in complex molecular systems. This underscores the need for more sophisticated models to accurately predict the complex interplay between these processes.

To address these challenges, we employed state-of-the-art molecular dynamics simulations to capture the relevant geometries observed in 2-Bromothiophene when excited at 240 nm and 255 nm. These geometries are classified using a decision tree, which is shown in Fig. 6.6. The classification is based on bond distances between C-C or C-S atoms as well as angles of the molecular skeleton determined by carbon and bromine atoms. This allows for the identification of all unique products observed in the simulations. Broadly, all the structures from the simulation are classified into one of the four groups: (i) P0, the ring-closed 'hot' ground state structure that the molecule eventually decays into subsequent to photoexcitation, (ii) P1, Bromine dissociation, (iii) P2, ring-opening involving C-S bond fragmentation of the first type, with S and Br atoms on the same side, and (iv) P3, ring-opening involving C-S bond fragmentation of the second type, where the S and Br atoms are at the terminal ends of the opened molecular structure. The ring-opened structures show a wide variation with four sub-categories for P2 and eight for P3. However, the geometries within each subclass produce very similar scattering signals, and therefore, cannot easily be distinguished from the experimental signal.

Our goal with the classification is to generate the UED signals for the geometries in each of these categories using IAM, which would allow us to fit the time-averaged experimental $\Delta I/I(s)$ data and hence estimate the contribution of each structure in our data. The experimental ΔI/I data and the fits are shown in Fig. 6.7 (b) and (c) for the two different wavelengths. As discussed above, ΔI measures the change in pump-induced radially averaged diffraction intensity relative to the ground state structure as a function of the momentum transfer vector, s. It is worthwhile to note that, the use of ΔI, which is closest to raw experimental data, allows for a more robust fitting by minimizing the impact of potential distortions inherent in the processed data. Specifically, here we focus on the end products after excitation at 240 nm and 255 nm by analyzing their respective $\Delta I/I$ signal averaged between 1 to 4 ps time-delays. For this time

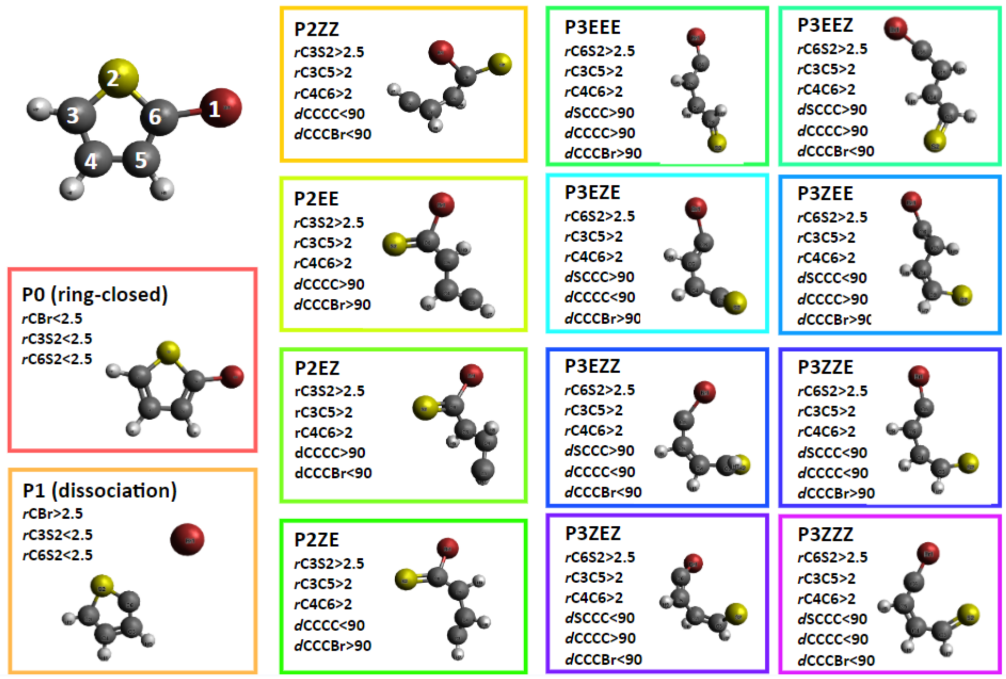

Figure 6.6: Classification of trajectories obtained from simulations into 16 categories based on bond distances and angles between atoms in 2-Bromothiophene.

range, we expect the transient photo-induced dynamics to be minimal while averaging the data for later time-delays improves the statistical reliability.

The fits for the time-averaged experimental $\Delta I/I(s)$ data are generated using a linear combination of the simulated UED signals, and are represented in red and green for 240 nm and 255 nm, respectively, in Fig. 6.7 (b) and (c). Using the basis functions to model the time-averaged experimental signal shows clear evidence of the contributions from Br-diss and RO dynamics at the two different wavelengths. Additionally, the fits reveal that, besides the ring-closed (P0) and bromine-dissociated (P1) structures, only three out of the twelve ring-opened structures significantly contribute to our final fits. Fig. 6.7 (a) shows the simulated UED signals for the five structures that contribute to our data. All the observed ring-opened structures belong to the P3 category, which involves C-S bond fragmentation such that S and Br atoms are at the terminal ends of the opened molecular structure. No contribution from P2 is observed at either of the wavelengths. Fig. 6.7 (d) – (f) show the geometries of the five structures that show

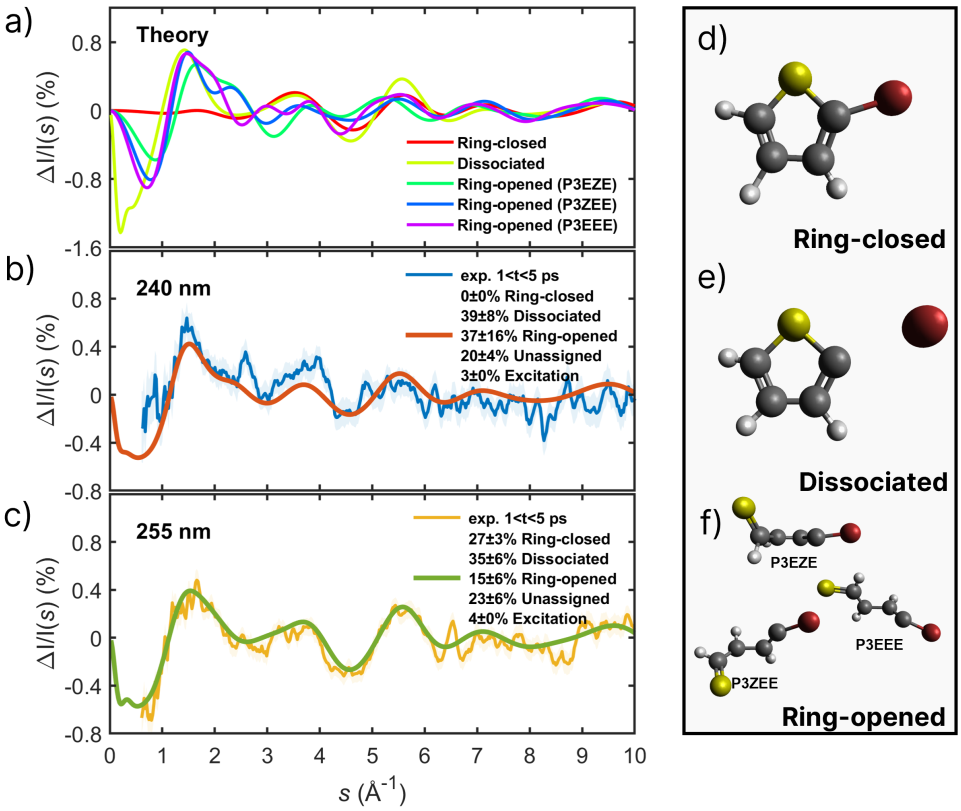

Figure 6.7: (a) Simulated UED signals of the 5 relevant structures that are observed in the experimental data. (b) and (c) show the time-averaged experimental UED signal at 240 nm and 255 nm in blue and yellow, respectively. The red and green lines are the fits generated using a linear combination of the UED signals shown in (a). (d)-(f) are the final state structures observed in our data.

a significant contribution in our data.

This simulation-based analysis approach effectively captures the distinct roles of these competing processes at each wavelength. Our comparison across the two excitation wavelengths indicates similar amounts of bromine dissociation at 255 nm (35%) and 240 nm (39%), whereas ring-opening occurs more prominently at 240 nm (37%) than at 255 nm (15%). Additionally, when excited at 255 nm, 2-Bromothiophene demonstrates a higher tendency to decay to an internally excited 'hot' ground state, P0, (27%). However, we do not detect any contribution from the 'hot' ground state structure at 240 nm. The branching ratios from the fits of the experimental data for the different relaxation pathways are shown in Table. 6.1 for the two excitation wavelengths.

In addition to observing the clear wavelength dependence in the competing processes of Br-Diss and RO, further exploration of the RO dynamics reveals clear trends as a function of wavelength. Specifically, ring-opening at 255 nm is predominantly classified as P3EEE type, whereas at 240 nm, it is mainly characterized by P3EZE and P3ZEE types shown in Fig. 6.7 (f). Although we observe ring-opening via the same C-S bond cleavage at both wavelengths, this method of structure classification enables us to decompose the experimental signal and identify the exact isomers that contribute to each wavelength. This provides an efficient means to disentangle the final molecular products, despite the complex landscape of excited states into which 2-Bromothiophene is initially excited after photoexcitation.

Table 6.1: Experimental Branching Ratios

Pathway	240 nm	255 nm
Br-Dissociation	$39 \pm 8\%$	$35 \pm 6\%$
Ring-opened	$37 \pm 16\%$	$15 \pm 6\%$
Ring-closed	$0 \pm 0\%$	$27 \pm 3\%$
Unassigned	$20 \pm 4\%$	$23 \pm 6\%$

Branching ratios obtained from experimental data of the different relaxation pathways of 2-Bromothiophene after excitation at 240 nm and 255 nm.

Table 6.2: Simulation Branching Ratios

Pathway	240 nm	255 nm
Br-Dissociation	30%	50%
Ring-opened	20%	10%
Ring-closed	50%	40%

Branching ratios obtained from simulations of the different relaxation pathways of 2-Bromothiophene after excitation at 240 nm and 255 nm.

It is important to note that the uncertainties in the fits for the 240 nm data are higher due to poorer statistics compared to the 255 nm data. Furthermore, we performed benchmark tests on our fits to determine the baseline uncertainty expected from using such a linear combination of basis functions to fit the experimental data. The performance of quantitatively retrieving contributions from the classified geometries was assessed by applying the fitting routine described above to the total theoretical difference-diffraction signal and the uncertainties obtained from such a fit established the baseline uncertainty at each wavelength. The benchmark tests reveal a baseline of 10% uncertainty for both 240 nm and 255 nm data. Contributions appearing in our fit that are lower than this baseline are considered unreliable and grouped together into the unassigned category.

To corroborate the wavelength-dependent results of our fits, we can extract similar insights directly from the simulated trajectories. The excited state non adiabatic molecular dynamics simulations were terminated when the gap between S0 and S1 went below 0.75 eV and the trajectories were continued adiabatically for both the singlet and triplet ground states, resulting in two sets of trajectories. Since the determination of the exact ratio between the singlet and triplet states is highly complex, we assumed a trajectory pool with equal contributions from both singlet and triplet trajectories. By tracking and categorizing the observed geometries from independent simulations at 240 nm and 255 nm excitations, we estimated the percentages of structures exhibiting Br-Diss versus RO dynamics.

Table 6.2 shows the branching ratios of the different relaxation pathways observed in simulations at the two wavelengths. Specifically, for RO, the simulations exhibit a general trend consistent with experimental observation with more RO at 240 nm excitation compared to 255 nm. However, the simulations predict higher Br-diss at 255 nm compared to 240 nm, deviating from the experimental observation. Additionally, simulations show a significantly higher contribution of ring-closed structures at both wavelengths – 50% at 240 nm and 40% at 255 nm – compared to 0% and 27%, respectively, obtained from the fits. This discrepancy arises because the 'hot' ring-closed geometry closely resembles the ground state structure of 2-Bromothiophene. Our analysis of the experimental data employs the difference-diffraction method, which involves subtraction of the diffraction signal contribution from the ground state structure to clearly reveal the signatures of the excited state geometries. As a result, this subtraction likely removes most of the signature from 'hot' ring-closed geometries, explaining their minimal contribution in the fits of our experimental data.

6.7 Conclusion

In summary, we have employed ultrafast electron diffraction to unravel the intricate molecular dynamics of 2-Bromothiophene under various excitation wavelengths, offering unprecedented insights into the wavelength-dependent competition between ring-opening and bond dissociation processes. Our comprehensive analysis not only highlights the critical role of the wavelength in dictating photochemical pathways but also illustrates the potential of UED as a powerful tool for probing the underlying molecular dynamics with remarkable temporal and structural resolution. Supported by sophisticated theoretical models, our findings provide a thorough understanding of the interplay between electronic and nuclear dynamics, thereby contributing significantly to the broader field of ultrafast photochemistry. This work underscores the feasibility of manipulating molecular processes through targeted photoexcitation, paving the way for innovative approaches in the synthesis and development of photoresponsive materials. Such insights are invaluable not only for the fundamental aspect of understand UV-induced photochemistry but also for applications spanning materials science, nanotechnology, and beyond by opening up new avenues for research into the control and manipulation of molecular dynamics. This chapter is based on work that was done in collaboration with Aaron LaForge, Pedro Nunes, Dean Lahana, Nanna List, Diptarka Hait, Amiel Paz, Surjendu Bhattacharyya, Kurtis Borne, Elio Champenois, Xinxin Cheng, Ruaridh Forbes, Matthias Hoffmann, Edwin Kukk Ming-Fu Lin, Shashank Pathak, Xiaozhe Shen, Anbu Venkatachalam, Matthew Ware, Jie Yang, Daniel Rolles, Martin Centurion, Thomas Wolf, Todd Martinez, and Nora Berrah. The manuscript is currently under preparation.

Chapter 7

Summary and Outlook

The goal of the experimental work described in this thesis is to observe the evolution of gas-phase photoinduced molecular dynamics at different system size scales and using different experimental techniques. We used IR pump - IR probe spectroscopy and kinematically complete coincident Coulomb explosion imaging to study the photoinduced isomerization processes, such as hydrogen migration, in relatively small molecules like acetonitrile and 1- and 2-propanol. We found that isomerization via hydrogen migration in acetonitrile is more prevalent than direct C-C bond fragmentation. This is possible due to the low energy barriers in the potential energy surface of singly-charged acetonitrile that allow access to highly stable isomerized structures. Conversely, in the propanol isomers, direct C-C bond fragmentation predominates, with hydrogen migration occurring with very low probability only in the case of triple ionization of the molecules. This highlights a trend where an increase in the alkyl chain length surprisingly reduces the likelihood of hydrogen migration in small molecules.

We have enhanced the scope of coincident Coulomb explosion imaging by developing a method to track neutral fragments in incomplete channels, as demonstrated by observing neutral H_2 roaming in acetonitrile. By integrating ultrafast IR pump-IR probe spectroscopy with this imaging technique, we can track the otherwise ’invisible’ neutral fragments involved in the roaming reaction, since our detection scheme is only capable of collecting charged particles. In doing so, we have developed an unambiguous and easily observable experimental signature to identify the presence of roaming pathways in a molecule upon photoexcitation. Our technique provides a more direct way to study neutral fragments and deepens our understanding of molecular dynamics in roaming reactions, beyond what conventional spectroscopy can achieve.

Scaling up in complexity, we have studied the relaxation and fragmentation dynamics of gas-phase C_{60} using intense, ultrashort FEL pulses in a single-color XUV-pump XUV-probe setup, combined with a reaction microscope (COLTRIMS). We were able to leverage the giant plasmon resonance of C_{60} to deposit a substantial amount of energy into the system and consequently study the time-dependent relaxation pathways through which such a stable structure dissipates energy. Our analysis of the temporal and kinetic energy dynamics of both light and heavy ionic fragments reveals the complex interplay between Coulombic and molecular forces acting over ultrashort timescales. Our theoretical analysis identified the formation of a transient nanoplasma state, which explains the distinctive temporal behavior of the C^{2+} yield compared to the other lighter fragments. The use of relatively simple theoretical models provided a comprehensive interpretation of these phenomena, which is crucial for understanding scenarios in which significant energy is rapidly deposited into large molecular systems, affecting energy redistribution in heterogeneous systems.

To gain direct insights into photoproduct geometries and their time-dependent evolution, we have used ultrafast electron diffraction, a technique distinct from Coulomb explosion imaging. This method allows us to detect changes in the diffraction patterns of a pulsed electron beam to study the molecular dynamics of 2-bromothiophene, a ring molecule, under two different UV excitation wavelengths. Through this analysis, we explored how the different wavelengths influence the competition between ring-opening and bond dissociation processes. Our findings, supported by sophisticated theoretical models, highlight UED's ability to probe molecular dynamics with exceptional temporal and structural resolution, shedding light on the interplay between electronic and nuclear dynamics that occurs upon UV photoexcitation. This work not only advances our understanding of UV-induced photochemistry but also suggests new methods for manipulating molecular processes, with potential applications in materials science, nanotechnology, and beyond.

Bibliography

1. Zewail, A. H. Femtochemistry: Atomic-scale dynamics of the chemical bond. *J. Phys. Chem. A* **104,** 5660–5694 (2000).
2. Wang, E. *et al.* Ultrafast Roaming Mechanisms in Ethanol Probed by Intense Extreme Ultraviolet Free-Electron Laser Radiation: Electron Transfer versus Proton Transfer. *J. Phys. Chem. Lett.* **14,** 4372–4380 (2023).
3. Vrakking, M. J. & Elsaesser, T. X-rays inspire electron movies. *Nature Photonics* **6,** 645–647 (2012).
4. Wells, E. *et al.* Adaptive strong-field control of chemical dynamics guided by three-dimensional momentum imaging. *Nature Communications* **4,** 2895 (2013).
5. Li, T. E., Cui, B., Subotnik, J. E. & Nitzan, A. Molecular polaritonics: Chemical dynamics under strong light–matter coupling. *Annual review of physical chemistry* **73,** 43–71 (2022).
6. Gordon, R. J. & Rice, S. A. Active control of the dynamics of atoms and molecules. *Annual review of physical chemistry* **48,** 601–641 (1997).
7. Williamson, J. C., Cao, J., Ihee, H., Frey, H. & Zewail, A. H. Clocking transient chemical changes by ultrafast electron diffraction. *Nature* **386,** 159–162 (1997).
8. Yang, J. *et al.* Diffractive imaging of coherent nuclear motion in isolated molecules. *Physical review letters* **117,** 153002 (2016).
9. Yang, J. *et al.* Diffractive imaging of a rotational wavepacket in nitrogen molecules with femtosecond megaelectronvolt electron pulses. *Nature communications* **7,** 11232 (2016).
10. Dantus, M., Kim, S. B., Williamson, J. C. & Zewail, A. H. Ultrafast electron diffraction. 5. Experimental time resolution and applications. *The Journal of Physical Chemistry* **98,** 2782–2796 (1994).

11. Weathersby, S. *et al.* Mega-electron-volt ultrafast electron diffraction at SLAC National Accelerator Laboratory. *Review of Scientific Instruments* **86,** 073702 (2015).

12. Gaffney, K. & Chapman, H. N. Imaging atomic structure and dynamics with ultrafast X-ray scattering. *science* **316,** 1444–1448 (2007).

13. Minitti, M. *et al.* Imaging molecular motion: Femtosecond x-ray scattering of an electrocyclic chemical reaction. *Physical review letters* **114,** 255501 (2015).

14. Schotte, F. *et al.* Watching a protein as it functions with 150-ps time-resolved x-ray crystallography. *Science* **300,** 1944–1947 (2003).

15. Schreier, W. J. *et al.* Thymine dimerization in DNA is an ultrafast photoreaction. *Science* **315,** 625–629 (2007).

16. Bhattacherjee, A. & Leone, S. R. Ultrafast X-ray transient absorption spectroscopy of gas-phase photochemical reactions: A new universal probe of photoinduced molecular dynamics. *Accounts of chemical research* **51,** 3203–3211 (2018).

17. Geneaux, R., Marroux, H. J., Guggenmos, A., Neumark, D. M. & Leone, S. R. Transient absorption spectroscopy using high harmonic generation: a review of ultrafast X-ray dynamics in molecules and solids. *Philosophical Transactions of the Royal Society A* **377,** 20170463 (2019).

18. Neumark, D. M. Time-resolved photoelectron spectroscopy of molecules and clusters. *Annual review of physical chemistry* **52,** 255–277 (2001).

19. Davies, J., LeClaire, J., Continetti, R. & Hayden, C. Femtosecond time-resolved photoelectron–photoion coincidence imaging studies of dissociation dynamics. *The Journal of chemical physics* **111,** 1–4 (1999).

20. Li, X. *et al.* Electron-ion coincidence measurements of molecular dynamics with intense X-ray pulses. *Scientific reports* **11,** 505 (2021).

21. Kling, N. G. *et al.* Time-resolved molecular dynamics of single and double hydrogen migration in ethanol. *Nat. Commun.* **10,** 1–8 (2019).

22. McDonnell, M. *et al.* Ultrafast laser-induced isomerization dynamics in acetonitrile. *J. Phys. Chem. Lett.* **11,** 6724–6729 (2020).

23. Mishra, D. *et al.* Ultrafast molecular dynamics in ionized 1-and 2-propanol: from simple fragmentation to complex isomerization and roaming mechanisms. *Phys. Chem. Chem. Phys.* **24,** 433–443 (2022).

24. Bhattacharyya, S. *et al.* Strong-Field-Induced Coulomb Explosion Imaging of Tribromomethane. *J. Phys. Chem. Lett.* **13,** 5845–5853 (2022).

25. Mayer, D. *et al.* Following excited-state chemical shifts in molecular ultrafast x-ray photoelectron spectroscopy. *Nature communications* **13,** 198 (2022).

26. Hüfner, S. *Photoelectron spectroscopy: principles and applications* (Springer Science & Business Media, 2013).

27. Liekhus-Schmaltz, C. E. *et al.* Ultrafast isomerization initiated by X-ray core ionization. *Nat. Commun.* **6,** 1–7 (2015).

28. Berrah, N. *et al.* Double-core-hole spectroscopy for chemical analysis with an intense X-ray femtosecond laser. *Proceedings of the National Academy of Sciences* **108,** 16912–16915 (2011).

29. Takahashi, O., Kryzhevoi, N. V. & Ueda, K. Probing chemical environment with molecular double core-hole electron spectroscopy. *Journal of Electron Spectroscopy and Related Phenomena* **204,** 290–302 (2015).

30. Figueras, M., Sousa, C. & Illas, F. Effect of electron correlation in the decomposition of core level binding energy shifts into initial and final state contributions. *Physical Chemistry Chemical Physics* **21,** 9399–9406 (2019).

31. Forbes, R. *et al.* Vacuum ultraviolet excited state dynamics of the smallest ketone: acetone. *The Journal of Physical Chemistry Letters* **12,** 8541–8547 (2021).

32. Marciniak, A. *et al.* XUV excitation followed by ultrafast non-adiabatic relaxation in PAH molecules as a femto-astrochemistry experiment. *Nature Communications* **6,** 7909 (2015).

33. Hervé, M., Boyer, A., Brédy, R., Compagnon, I. & Lépine, F. Ultrafast dynamics in molecular ions following UV and XUV excitation: a perspective. *Advances in Physics: X* **7,** 2123283 (2022).

34. Wiese, J., Onvlee, J., Trippel, S. & Küpper, J. Strong-field ionization of complex molecules. *Physical Review Research* **3,** 013089 (2021).

35. Wu, J. *et al.* Probing the tunnelling site of electrons in strong field enhanced ionization of molecules. *Nature communications* **3,** 1113 (2012).

36. Johnson, P. M. & Otis, C. E. Molecular multiphoton spectroscopy with ionization detection. *Annual Review of Physical Chemistry* **32,** 139–157 (1981).

37. l'Huillier, A., Mainfray, G. & Johnson, P. Multiphoton ionization versus dissociation of diatomic molecules irradiated by an intense 40 ps laser pulse. *Chemical physics letters* **103,** 447–450 (1984).

38. Syage, J. & Wessel, J. Molecular multiphoton ionization and ion fragmentation spectroscopy. *Applied Spectroscopy Reviews* **24,** 1–79 (1988).

39. Köuppel, H., Domcke, W. & Cederbaum, L. S. Multimode molecular dynamics beyond the Born-Oppenheimer approximation. *Advances in chemical physics,* 59–246 (1984).

40. Cederbaum, L. S. Direct calculation of ionization potentials of closed-shell atoms and molecules. *Theoretica chimica acta* **31,** 239–260 (1973).

41. Inhester, L., Hanasaki, K., Hao, Y., Son, S.-K., Santra, R., *et al.* X-ray multiphoton ionization dynamics of a water molecule irradiated by an x-ray free-electron laser pulse. *Physical Review A* **94,** 023422 (2016).

42. Jurek, Z., Son, S.-K., Ziaja, B. & Santra, R. XMDYN and XATOM: versatile simulation tools for quantitative modeling of X-ray free-electron laser induced dynamics of matter. *Journal of Applied Crystallography* **49,** 1048–1056 (2016).

43. Gallmann, L. *et al.* Photoemission and photoionization time delays and rates. *Structural Dynamics* **4** (2017).

44. Gochel-Dupuis, M., Delwiche, J., Hubin-Franskin, M.-J. & Collin, J. High-resolution HeI photoelectron spectrum of acetonitrile. *Chemical physics letters* **193,** 41–48 (1992).

45. Boll, R. *Imaging molecular structure with photoelectron diffraction* PhD thesis (Ruprecht-Karls-Universität Heidelberg, 2014).

46. Strickland, D. & Mourou, G. Compression of amplified chirped optical pulses. *Optics communications* **55,** 447–449 (1985).

47. Ullrich, J. *et al.* Recoil-ion and electron momentum spectroscopy: reaction-microscopes. *Rep. Prog. Phys.* **66,** 1463 (2003).

48. Dörner, R. *et al.* Cold target recoil ion momentum spectroscopy: a 'momentum microscope' to view atomic collision dynamics. *Physics Reports* **330,** 95–192 (2000).

49. Kircher, M. *et al.* Kinematically complete experimental study of Compton scattering at helium atoms near the threshold. *Nature physics* **16,** 756–760 (2020).

50. Schmidt-Böcking, H., Ullrich, J., Dörner, R. & Cocke, C. L. The COLTRIMS reaction microscope—the spyhole into the ultrafast entangled dynamics of atomic and molecular systems. *Annalen der Physik* **533,** 2100134 (2021).

51. Pathak, S. *et al.* Differentiating and quantifying gas-phase conformational isomers using Coulomb explosion imaging. *J. Phys. Chem. Lett.* **11,** 10205–10211 (2020).

52. Hartung, A. *et al.* Magnetic fields alter strong-field ionization. *Nature Physics* **15,** 1222–1226 (2019).

53. Boll, R. *et al.* X-ray multiphoton-induced Coulomb explosion images complex single molecules. *Nat. Phys.* **18,** 423–428 (2022).

54. Pitzer, M. *et al.* Coulomb explosion imaging as a tool to distinguish between stereoisomers. *JoVE (Journal of Visualized Experiments),* e56062 (2017).

55. Vela-Peréz, I. *et al.* High-energy molecular-frame photoelectron angular distributions: a molecular bond-length ruler. *Physical Chemistry Chemical Physics* **25,** 13784–13791 (2023).

56. Trinter, F. *et al.* Ultrafast temporal evolution of interatomic Coulombic decay in NeKr dimers. *Chemical science* **13,** 1789–1800 (2022).

57. Sabbar, M. *et al.* Combining attosecond XUV pulses with coincidence spectroscopy. *Review of Scientific Instruments* **85** (2014).

58. Burger, C. *et al.* Time-resolved nuclear dynamics in bound and dissociating acetylene. *Struct. Dyn.* **5,** 044302 (2018).

59. *RoentDek Handels GmbH - Time and Position sensitive MCP Delay Line Detectors — roentdek.com* `https://www.roentdek.com/Coltrims/`.

60. Eland, J. Dynamics of fragmentation reactions from peak shapes in multiparticle coincidence experiments. *Laser Chem.* **11,** 259–263 (1991).

61. Pandey, A. K. *Dissociation Dynamics of Unstable Molecular Systems* PhD thesis (Dissertation, Mohanlal Sukhadia University, UDAIPUR, India, 2014).

62. Vager, Z., Naaman, R. & Kanter, E. Coulomb explosion imaging of small molecules. *Science* **244,** 426–431 (1989).

63. Stapelfeldt, H., Constant, E. & Corkum, P. Wave packet structure and dynamics measured by Coulomb explosion. *Physical review letters* **74,** 3780 (1995).

64. Allum, F. *et al.* Coulomb explosion imaging of CH3I and CH2ClI photodissociation dynamics. *The Journal of chemical physics* **149** (2018).

65. Légaré, F., Lee, K. F., Bandrauk, A., Villeneuve, D. & Corkum, P. Laser Coulomb explosion imaging for probing ultra-fast molecular dynamics. *Journal of Physics B: Atomic, Molecular and Optical Physics* **39,** S503 (2006).

66. Schnorr, K. *et al.* Electron rearrangement dynamics in dissociating I 2 n+ molecules accessed by extreme ultraviolet pump-probe experiments. *Physical review letters* **113,** 073001 (2014).

67. Jiang, Y. *et al.* Investigating two-photon double ionization of D 2 by XUV-pump–XUV-probe experiments. *Physical Review A* **81,** 051402 (2010).

68. Jiang, Y. *et al.* Ultrafast extreme ultraviolet induced isomerization of acetylene cations. *Physical review letters* **105,** 263002 (2010).

69. Erk, B. *et al.* Imaging charge transfer in iodomethane upon x-ray photoabsorption. *Science* **345,** 288–291 (2014).

70. Xie, X. *et al.* Structural determination of argon trimer. *AIP Adv.* **5,** 097213 (2015).

71. Neumann, N. *et al.* Fragmentation dynamics of CO 2 3+ investigated by multiple electron capture in collisions with slow highly charged ions. *Phys. Rev. Lett.* **104,** 103201 (2010).

72. Hsieh, S. & Eland, J. H. Reaction dynamics of three-body dissociations in triatomic molecules from single-photon double ionization studied by a time-and position-sensitive coincidence method. *Journal of Physics B: Atomic, Molecular and Optical Physics* **30,** 4515 (1997).

73. Ko, C. *et al.* Ab initio excited-state dynamics of the photoactive yellow protein chromophore. *Journal of the American Chemical Society* **125,** 12710–12711 (2003).

74. Allmann, S. & Baldwin, I. T. Insects betray themselves in nature to predators by rapid isomerization of green leaf volatiles. *Science* **329,** 1075–1078 (2010).

75. Wald, G. Molecular basis of visual excitation. *Science* **162,** 230–239 (1968).

76. Gai, F., Hasson, K., McDonald, J. C. & Anfinrud, P. A. Chemical dynamics in proteins: the photoisomerization of retinal in bacteriorhodopsin. *Science* **279,** 1886–1891 (1998).

77. Hayward, G., Carlsen, W., Siegman, A. & Stryer, L. Retinal chromophore of rhodopsin photoisomerizes within picoseconds. *Science* **211,** 942–944 (1981).

78. Schoenlein, R. W., Peteanu, L. A., Mathies, R. A. & Shank, C. V. The first step in vision: femtosecond isomerization of rhodopsin. *Science* **254,** 412–415 (1991).

79. Dugave, C. & Demange, L. Cis- trans isomerization of organic molecules and biomolecules: implications and applications. *Chem. Rev.* **103,** 2475–2532 (2003).

80. Merino, E. & Ribagorda, M. Control over molecular motion using the cis–trans photoisomerization of the azo group. *Beilstein journal of organic chemistry* **8,** 1071–1090 (2012).

81. Shaw, M. F. *et al.* Photo-tautomerization of acetaldehyde as a photochemical source of formic acid in the troposphere. *Nat. Commun.* **9,** 2584 (2018).

82. Burger, C. *et al.* Visualization of bond rearrangements in acetylene using near single-cycle laser pulses. *Faraday Discuss.* **194,** 495–508 (2016).

83. Turecek, F. & Syrstad, E. A. Mechanism and energetics of intramolecular hydrogen transfer in amide and peptide radicals and cation-radicals. *J. Am. Chem. Soc.* **125,** 3353–3369 (2003).

84. Piekarski, D. G. *et al.* Unusual hydroxyl migration in the fragmentation of β-alanine dication in the gas phase. *Phys. Chem. Chem. Phys.* **17,** 16767–16778 (2015).

85. Gagnon, J., Lee, K. F., Rayner, D., Corkum, P. & Bhardwaj, V. Coincidence imaging of polyatomic molecules via laser-induced Coulomb explosion. *J. Phys. B: At., Mol. Opt. Phys.* **41,** 215104 (2008).

86. Feuerstein, B. *et al.* Complete characterization of molecular dynamics in ultrashort laser fields. *Phys. Rev. Lett.* **99,** 153002 (2007).

87. Corrales, M., González-Vázquez, J., de Nalda, R. & Bañares, L. Coulomb explosion imaging for the visualization of a conical intersection. *J. Phys. Chem. Lett.* **10,** 138–143 (2018).

88. Fushitani, M. Applications of pump-probe spectroscopy. *Annu. Rep. Prog. Chem., Sect. C: Phys. Chem.* **104,** 272–297 (2008).

89. Ullrich, J. *et al.* Recoil-ion momentum spectroscopy. *J. Phys. B: At., Mol. Opt. Phys.* **30,** 2917 (1997).

90. Maclot, S. *et al.* Dynamics of glycine dications in the gas phase: ultrafast intramolecular hydrogen migration versus Coulomb repulsion. *J. Phys. Chem. Lett.* **4,** 3903–3909 (2013).

91. Maclot, S. *et al.* Determination of energy-transfer distributions in ionizing ion-molecule collisions. *Phys. Rev. Lett.* **117,** 073201 (2016).

92. Piekarski, D. G. *et al.* Production of doubly-charged highly reactive species from the long-chain amino acid GABA initiated by Ar^{9+} ionization. *Phys. Chem. Chem. Phys.* **19,** 19609–19618 (2017).

93. Rousseau, P. *et al.* Polypeptide formation in clusters of β-alanine amino acids by single ion impact. *Nat. Commun.* **11,** 3818 (2020).

94. Becke, A. D. Density-functional thermochemistry. III. The role of exact exchange. *J. Chem. Phys.* **98,** 5648–5652 (1993).

95. Lee, C., Yang, W. & Parr, R. G. Development of the Colle-Salvetti correlation-energy formula into a functional of the electron density. *Phys. Rev. B* **37,** 785–789 (1988).

96. Schlegel, H. B. *et al.* Ab initio molecular dynamics: Propagating the density matrix with Gaussian orbitals. *J. Chem. Phys.* **114,** 9758–9763 (2001).

97. Iyengar, S. S. *et al.* Ab initio molecular dynamics: Propagating the density matrix with Gaussian orbitals. II. Generalizations based on mass-weighting, idempotency, energy conservation and choice of initial conditions. *J. Chem. Phys.* **115,** 10291–10302 (2001).

98. Schlegel, H. B. *et al.* Ab initio molecular dynamics: Propagating the density matrix with Gaussian orbitals. III. Comparison with Born–Oppenheimer dynamics. *J. Chem. Phys.* **117,** 8694–8704 (2002).

99. Iyengar, S. S., Schlegel, H. B. & Voth, G. A. Atom-Centered Density Matrix Propagation (ADMP): Generalizations Using Bohmian Mechanics. *J. Phys. Chem. A* **107,** 7269–7277 (2003).

100. Frisch, M. J. *et al. Gaussian16 Revision C.01* Gaussian Inc. Wallingford CT. 2016.

101. Capron, M. *et al.* A Multicoincidence Study of Fragmentation Dynamics in Collision of γ-Aminobutyric Acid with Low-Energy Ions. *Chem.–Eur. J.* **18,** 9321–9332 (2012).

102. Kukk, E. *et al.* Internal energy dependence in X-ray-induced molecular fragmentation: an experimental and theoretical study of thiophene. *Phys. Rev. A* **91,** 043417 (2015).

103. Houston, P. & Kable, S. Photodissociation of acetaldehyde as a second example of the roaming mechanism. *Proc. Natl. Acad. Sci. U.S.A.* **103,** 16079–16082 (2006).

104. Rubio-Lago, L. *et al.* Slice imaging of the photodissociation of acetaldehyde at 248 nm. Evidence of a roaming mechanism. *Phys. Chem. Chem. Phys.* **9,** 6123–6127 (2007).

105. Harding, L. B., Klippenstein, S. J. & Jasper, A. W. Ab initio methods for reactive potential surfaces. *Phys. Chem. Chem. Phys.* **9,** 4055–4070 (2007).

106. Shepler, B. C., Braams, B. J. & Bowman, J. M. Quasiclassical trajectory calculations of acetaldehyde dissociation on a global potential energy surface indicate significant non-transition state dynamics. *J. Phys. Chem. A* **111,** 8282–8285 (2007).

107. Xie, X. *et al.* Role of proton dynamics in efficient photoionization of hydrocarbon molecules. *Phys. Rev. A* **89,** 023429 (2014).

108. Roither, S. *et al.* High energy proton ejection from hydrocarbon molecules driven by highly efficient field ionization. *Phys. Rev. Lett.* **106,** 163001 (2011).

109. Ekanayake, N. *et al.* H2 roaming chemistry and the formation of H3+ from organic molecules in strong laser fields. *Nat. Commun.* **9,** 1–11 (2018).

110. Bowman, J. M. & Shepler, B. C. Roaming radicals. *Annu. Rev. Phys. Chem.* **62,** 531–553 (2011).

111. Bowman, J. M. & Houston, P. L. Theories and simulations of roaming. *Chem. Soc. Rev.* **46,** 7615–7624 (2017).

112. Suits, A. G. Roaming Reactions and Dynamics in the van der Waals Region. *Annu. Rev. Phys. Chem.* **71,** 77–100 (2020).

113. Townsend, D. *et al.* The roaming atom: straying from the reaction path in formaldehyde decomposition. *Science* **306,** 1158–1161 (2004).

114. Heazlewood, B. R. *et al.* Roaming is the dominant mechanism for molecular products in acetaldehyde photodissociation. *Proc. Natl. Acad. Sci. U.S.A.* **105,** 12719–12724 (2008).

115. Maeda, S., Ohno, K. & Morokuma, K. A theoretical study on the photodissociation of acetone: Insight into the slow intersystem crossing and exploration of nonadiabatic pathways to the ground state. *J. Phys. Chem. Lett.* **1,** 1841–1845 (2010).

116. Grubb, M. P. *et al.* No straight path: roaming in both ground-and excited-state photolytic channels of NO3 → NO + O2. *Science* **335,** 1075–1078 (2012).

117. Nakamura, M. *et al.* Dynamical, spectroscopic and computational imaging of bond breaking in photodissociation: roaming and role of conical intersections. *Faraday Discuss.* **177,** 77–98 (2015).

118. Lombardi, A. *et al.* Rovibrationally excited molecules on the verge of a triple breakdown: molecular and roaming mechanisms in the photodecomposition of methyl formate. *J. Phys. Chem. A* **120,** 5155–5162 (2016).

119. Rauta, A. K. & Maiti, B. Roaming mediated nonadiabatic dynamics in molecular hydrogen elimination from propane at 157 nm. *Chem. Phys. Lett.* **661,** 83–88 (2016).

120. Geballe, T. & Oka, T. Detection of H3+ in interstellar space. *Nature* **384,** 334–335 (1996).

121. McCall, B., Geballe, T., Hinkle, K. & Oka, T. Detection of H3+ in the diffuse interstellar medium toward Cygnus OB2 No. 12. *Science* **279,** 1910–1913 (1998).

122. Herbst, E. & Klemperer, W. The formation and depletion of molecules in dense interstellar clouds. *Astrophys. J.* **185,** 505–534 (1973).

123. Mi, Y. *et al.* D3+ formation through photoionization of the molecular D2–D2 dimer. *Nat. Chem.* **15,** 1224–1228 (2023).

124. Zhou, L. *et al.* Ultrafast formation dynamics of D3+ from the light-driven bimolecular reaction of the D2–D2 dimer. *Nat. Chem.* **15,** 1229–1235 (2023).

125. Furukawa, Y., Hoshina, K., Yamanouchi, K. & Nakano, H. Ejection of triatomic hydrogen molecular ion from methanol in intense laser fields. *Chem. Phys. Lett.* **414,** 117–121 (2005).

126. Hoshina, K., Furukawa, Y., Okino, T. & Yamanouchi, K. Efficient ejection of H3+ from hydrocarbon molecules induced by ultrashort intense laser fields. *J. Chem. Phys.* **129,** 104302 (2008).

127. Hoshina, K. & Tsuge, M. Formation of H3O+ from ethanol clusters induced by intense femtosecond laser fields. *Chem. Phys. Lett.* **489,** 154–158 (2010).

128. Kraus, P. M. *et al.* Unusual mechanism for H3+ formation from ethane as obtained by femtosecond laser pulse ionization and quantum chemical calculations. *J. Chem. Phys.* **134,** 114302 (2011).

129. Okino, T., Watanabe, A., Xu, H. & Yamanouchi, K. Two-body Coulomb explosion in methylacetylene in intense laser fields: double proton migration and proton/deuteron exchange. *Phys. Chem. Chem. Phys.* **14,** 4230–4235 (2012).

130. Schirmel, N., Reusch, N., Horsch, P. & Weitzel, K.-M. Formation of fragment ions (H+, H3+, CH3+) from ethane in intense femtosecond laser fields–from understanding to control. *Faraday Discuss.* **163,** 461–474 (2013).

131. Kotsina, N., Kaziannis, S. & Kosmidis, C. Phase dependence of OD+, HOD+, and H3+ ions released from the deuterated dication of methanol under $\omega/2\omega$ laser field irradiation. *Int. J. Mass Spectrom.* **380,** 34–39 (2015).

132. Ekanayake, N. *et al.* Mechanisms and time-resolved dynamics for trihydrogen cation (H3+) formation from organic molecules in strong laser fields. *Sci. Rep.* **7,** 1–12 (2017).

133. Luzon, I., Livshits, E., Gope, K., Baer, R. & Strasser, D. Making sense of Coulomb explosion imaging. *J. Phys. Chem. Lett.* **10,** 1361–1367 (2019).

134. Livshits, E., Luzon, I., Gope, K., Baer, R. & Strasser, D. Time-resolving the ultrafast H2 roaming chemistry and H3+ formation using extreme-ultraviolet pulses. *Communications Chemistry* **3,** 49 (2020).

135. Gope, K., Livshits, E., Bittner, D. M., Baer, R. & Strasser, D. An “inverse” harpoon mechanism. *Sci. Adv.* **8,** eabq8084 (2022).

136. Gope, K., Bittner, D. M. & Strasser, D. Sequential mechanism in H 3+ formation dynamics on the ethanol dication. *Phys. Chem. Chem. Phys.* **25,** 6979–6986 (2023).

137. Endo, T. *et al.* Capturing roaming molecular fragments in real time. *Science* **370,** 1072–1077 (2020).

138. Hu, P. *et al.* Progress in nitrile-based polymer electrolytes for high performance lithium batteries. *J. Mater. Chem.A* **4,** 10070–10083 (2016).

139. Zhong, P., Zhang, L., Luo, N. & Liu, J. Advances in the Application of Acetonitrile in Organic Synthesis since 2018. *Catalysts* **13,** 761 (2023).

140. Clark, T., Chandrasekhar, J., Spitznagel, G. W. & Schleyer, P. V. R. Efficient diffuse function-augmented basis sets for anion calculations. III. The 3-21+G basis set for first-row elements, Li-F. *J. Comput. Chem.* **4,** 294–301 (1983).

141. Krishnan, R., Binkley, J. S., Seeger, R. & Pople, J. A. Self-consistent molecular orbital methods. XX. A basis set for correlated wave functions. *J. Chem. Phys.* **72,** 650–654 (1980).

142. Barreiro-Lage, D. *et al.* "Smart Decomposition" of Cyclic Alanine-Alanine Dipeptide by VUV Radiation: A Seed for the Synthesis of Biologically Relevant Species. *J. Phys. Chem. Lett.* **12,** 7379–7386 (2021).

143. Ganguly, S. *et al.* The origin of enhanced O2+ production from photoionized CO2 clusters. *Commun. Chem.* **5,** 16 (2022).

144. Bittner, D. M., Gope, K., Livshits, E., Baer, R. & Strasser, D. Sequential and concerted C–C and C–O bond dissociation in the Coulomb explosion of 2-propanol. *J. Chem. Phys.* **157** (2022).

145. Yang, Y. *et al.* H2 formation via non-Born-Oppenheimer hydrogen migration in photoionized ethane. *Nature Communications* **14,** 4951 (2023).

146. Ding, X. *et al.* Ultrafast dissociation of Metastable CO 2+ in a dimer. *Physical Review Letters* **118,** 153001 (2017).

147. Gope, K., Livshits, E., Bittner, D. M., Baer, R. & Strasser, D. Two pathways and an isotope effect in H 3+ formation following double ionization of methanol. *Natural Sciences* **1,** e10022 (2021).

148. Bostedt, C. *et al.* Linac coherent light source: The first five years. *Reviews of Modern Physics* **88,** 015007 (2016).

149. Bergman, U., Yachandra, V. K. & Yano, J. *X-ray free electron lasers: applications in materials, chemistry and biology* (Royal Society of Chemistry, 2017).

150. Young, L. *et al.* Femtosecond electronic response of atoms to ultra-intense X-rays. *Nature* **466,** 56–61 (2010).

151. Glover, T. E. *et al.* X-ray and optical wave mixing. *Nature* **488,** 603–608 (2012).

152. Hertel, I., Laarmann, T. & Schulz, C. in *Adv. At. Mol. Opt.* 219 (Elsevier, 2005).

153. Shchatsinin, I., Laarmann, T., Zhavoronkov, N., Schulz, C. P. & Hertel, I. V. Ultrafast energy redistribution in C_{60} fullerenes: A real time study by two-color femtosecond spectroscopy. *J. Chem. Phys.* **129,** 204308 (2008).

154. Murphy, B. *et al.* Femtosecond X-ray-induced explosion of C_{60} at extreme intensity. *Nat. Commun.* **5,** 4281 (2014).

155. Berrah, N. *et al.* Femtosecond-resolved observation of the fragmentation of buckminsterfullerene following X-ray multiphoton ionization. *Nat. Phys.* **15,** 1279–1283 (2019).

156. Johansson, J. O. & Campbell, E. E. Probing excited electronic states and ionisation mechanisms of fullerenes. *Chem. Soc. Rev.* **42,** 5661–5671 (2013).

157. Feng, M., Zhao, J. & Petek, H. Atomlike, hollow-core–bound molecular orbitals of C_{60}. *Science* **320,** 359–362 (2008).

158. Mignolet, B., Johansson, J. O., Campbell, E. E. & Remacle, F. Probing Rapidly-Ionizing Super-Atom Molecular Orbitals in C_{60}: A Computational and Femtosecond Photoelectron Spectroscopy Study. *ChemPhysChem* **14,** 3332–3340 (2013).

159. Li, H. *et al.* Coherent electronic wave packet motion in C_{60} controlled by the waveform and polarization of few-cycle laser fields. *Phys. Rev. Lett.* **114,** 123004 (2015).

160. Bréchignac, C. & Connerade, J. Giant resonances in free atoms and in clusters. *Journal of Physics B: Atomic, Molecular and Optical Physics* **27,** 3795 (1994).

161. Hertel, I. *et al.* Giant plasmon excitation in free C_{60} and C 70 molecules studied by photoionization. *Phys. Rev. Lett.* **68,** 784 (1992).

162. Campbell, E. & Levine, R. Delayed ionization and fragmentation en route to thermionic emission: Statistics and dynamics. *Annu. Rev. Phys. Chem.* **51,** 65–98 (2000).

163. Bhardwaj, V., Corkum, P. & Rayner, D. Internal laser-induced dipole force at work in C_{60} molecule. *Phys. Rev. Lett.* **91,** 203004 (2003).

164. Li, H. *et al.* Transition from SAMO to Rydberg state ionization in C_{60} in femtosecond laser fields. *J. Phys. Chem. Lett.* **7,** 4677–4682 (2016).

165. Jaroń-Becker, A., Becker, A. & Faisal, F. Single-active-electron ionization of C_{60} in intense laser pulses to high charge states. *J. Chem. Phys.* **126,** 124310 (2007).

166. Lebeault, M.-A. *et al.* Decay of C_{60} by delayed ionization and C2 emission: Experiment and statistical modeling of kinetic energy release. *J. Chem. Phys.* **137,** 054312 (2012).

167. Camacho Garibay, A., Saalmann, U. & Rost, J. M. Prevailing Features of X-Ray-Induced Molecular Electron Spectra Revealed with Fullerenes. *Phys. Rev. Lett.* **113,** 083001 (Aug. 2014).

168. Maurat, E., Hervieux, P. & Lépine, F. Surface plasmon resonance in C_{60} revealed by photoelectron imaging spectroscopy. *J. Phys. B* **42,** 165105 (2009).

169. Pellegrini, C., Marinelli, A. & Reiche, S. The physics of x-ray free-electron lasers. *Reviews of Modern Physics* **88,** 015006 (2016).

170. Allaria, E. *et al.* Highly coherent and stable pulses from the FERMI seeded free-electron laser in the extreme ultraviolet. *Nature Photonics* **6,** 699–704 (2012).

171. Ratner, D. *et al.* Experimental demonstration of a soft x-ray self-seeded free-electron laser. *Physical review letters* **114,** 054801 (2015).

172. *FLASH Parameters — photon-science.desy.de* `https://photon-science.desy.de/facilities/flash/flash_parameters/index_eng.html`.

173. Faatz, B. *et al.* Simultaneous operation of two soft x-ray free-electron lasers driven by one linear accelerator. *New Journal of physics* **18,** 062002 (2016).

174. Faatz, B. *et al.* The FLASH facility: Advanced options for FLASH2 and future perspectives. *Applied Sciences* **7,** 1114 (2017).

175. Schmid, G. *et al.* Reaction microscope endstation at FLASH2. *J. Synchrotron Radiat.* **26,** 854 (2019).

176. Meister, S. *et al.* Atomic, molecular and cluster science with the reaction microscope endstation at flash2. *Appl. Sci.* **10,** 2953 (2020).

177. Tersoff, J. Modeling solid-state chemistry: Interatomic potentials for multicomponent systems. *Phys. Rev. B* **39,** 5566 (Mar. 1989).

178. Saalmann, U., Siedschlag, C. & Rost, J. Mechanisms of cluster ionization in strong laser pulses. *J. Phys. B* **39,** R
bibrangessep 39 (2006).

179. Bostedt, C. *et al.* Multistep ionization of argon clusters in intense femtosecond extreme ultraviolet pulses. *Phys. Rev. Lett.* **100,** 133401 (2008).

180. Saalmann, U., Georgescu, I. & Rost, J. M. Tracing non-equilibrium plasma dynamics on the attosecond timescale in small clusters. *New Journal of Physics* **10,** 025014 (2008).

181. Fennel, T. *et al.* Laser-driven nonlinear cluster dynamics. *Rev. Mod. Phys.* **82,** 1793 (2010).

182. Ostrikov, K. K., Beg, F. & Ng, A. Colloquium: Nanoplasmas generated by intense radiation. *Rev. Mod. Phys.* **88,** 011001 (2016).

183. Wolf, T. J. *et al.* The photochemical ring-opening of 1, 3-cyclohexadiene imaged by ultrafast electron diffraction. *Nature chemistry* **11,** 504–509 (2019).

184. Yang, J. *et al.* Imaging CF3I conical intersection and photodissociation dynamics with ultrafast electron diffraction. *Science* **361,** 64–67 (2018).

185. Xu, S., Park, S. T., Feenstra, J. S., Srinivasan, R. & Zewail, A. H. Ultrafast electron diffraction: structural dynamics of the elimination reaction of acetylacetone. *The Journal of Physical Chemistry A* **108,** 6650–6655 (2004).

186. Park, S. T., Feenstra, J. S. & Zewail, A. H. Ultrafast electron diffraction: Excited state structures and chemistries of aromatic carbonyls. *The Journal of chemical physics* **124** (2006).

187. Srinivasan, R., Lobastov, V. A., Ruan, C.-Y. & Zewail, A. H. Ultrafast electron diffraction (UED) a new development for the 4D determination of transient molecular structures. *Helvetica chimica acta* **86,** 1761–1799 (2003).

188. Mark, H. & Wierl, R. Über Elektronenbeugung am einzelnen molekül. *Naturwissenschaften* **18,** 205–205 (1930).

189. Mark, H. & Wierl, R. The determination of molecular structures by diffraction of electrons on a steam jet. *journal for electrochemistry and applied physical chemistry* **36,** 675–676 (1930).

190. Brockway, L. O. Electron diffraction by gas molecules. *Reviews of Modern Physics* **8,** 231 (1936).

191. Pauling, L. & Brockway, L. O. The radial distribution method of interpretation of electron diffraction photographs of gas molecules. *Journal of the American Chemical Society* **57,** 2684–2692 (1935).

192. Shorokhov, D., Park, S. T. & Zewail, A. H. Ultrafast electron diffraction: Dynamical structures on complex energy landscapes. *ChemPhysChem* **6,** 2228–2250 (2005).

193. Baskin, J. S. & Zewail, A. H. Ultrafast electron diffraction: Oriented molecular structures in space and time. *ChemPhysChem* **6,** 2261–2276 (2005).

194. Williamson, J. C. & Zewail, A. H. Ultrafast electron diffraction. 4. Molecular structures and coherent dynamics. *The Journal of Physical Chemistry* **98,** 2766–2781 (1994).

195. Michalik, A., Sherman, E. Y. & Sipe, J. Theory of ultrafast electron diffraction: The role of the electron bunch properties. *Journal of Applied Physics* **104** (2008).

196. Hedberg, K. Electron diffraction in gases by MI Davis. *Acta Crystallographica Section A: Crystal Physics, Diffraction, Theoretical and General Crystallography* **28,** 475–475 (1972).

197. Liu, Y. *et al.* Rehybridization dynamics into the pericyclic minimum of an electrocyclic reaction imaged in real-time. *Nature Communications* **14,** 2795 (2023).

198. Lin, M.-F., Reid, A., Shen, X. & Wolf, T. Imaging Ultrafast Structural Dynamics with Megaelectronvolt Ultrafast Electron Diffraction (2023).

199. Centurion, M., Wolf, T. J. & Yang, J. Ultrafast imaging of molecules with electron diffraction. *Annual Review of Physical Chemistry* **73,** 21–42 (2022).

200. Nunes, J. *et al.* Liquid-phase mega-electron-volt ultrafast electron diffraction. *Structural Dynamics* **7,** 024301 (2020).

201. Ashfold, M. N. *et al.* Exploring the dynamics of the photoinduced ring-opening of heterocyclic molecules. *The journal of physical chemistry letters* **8,** 3440–3451 (2017).

202. Karashima, S. *et al.* Ultrafast ring-opening reaction of 1, 3-cyclohexadiene: identification of nonadiabatic pathway via doubly excited state. *Journal of the American Chemical Society* **143,** 8034–8045 (2021).

203. Pathak, S. *et al.* Tracking the ultraviolet-induced photochemistry of thiophenone during and after ultrafast ring opening. *Nat. Chem.* **12,** 795–800 (2020).

204. Attar, A. R. *et al.* Femtosecond x-ray spectroscopy of an electrocyclic ring-opening reaction. *Science* **356,** 54–59 (2017).

205. Dasgupta, J., Frontiera, R. R., Taylor, K. C., Lagarias, J. C. & Mathies, R. A. Ultrafast excited-state isomerization in phytochrome revealed by femtosecond stimulated Raman spectroscopy. *Proc. Natl. Acad. Sci.* **106,** 1784–1789 (2009).

206. Eelkema, R. *et al.* Nanomotor rotates microscale objects. *Nature* **440,** 163–163 (2006).

207. Kompa, K. & Levine, R. A molecular logic gate. *Proceedings of the National Academy of Sciences* **98,** 410–414 (2001).

208. Geppert, D., Seyfarth, L. & de Vivie-Riedle, R. Laser control schemes for molecular switches. *Applied Physics B* **79,** 987–992 (2004).

209. Deb, S. & Weber, P. M. The ultrafast pathway of photon-induced electrocyclic ring-opening reactions: the case of 1, 3-cyclohexadiene. *Annual review of physical chemistry* **62,** 19–39 (2011).

210. Ihee, H., Goodson, B. M., Srinivasan, R., Lobastov, V. A. & Zewail, A. H. Ultrafast electron diffraction and structural dynamics: Transient intermediates in the elimination reaction of C2F4I2. *The Journal of Physical Chemistry A* **106,** 4087–4103 (2002).

211. Shmueli, U. *International Tables for Crystallography, Volume B: Reciprocal Space* (Springer Science & Business Media, 2008).

212. Shen, X. *et al.* Femtosecond gas-phase mega-electron-volt ultrafast electron diffraction. *Structural Dynamics* **6,** 054305 (2019).

213. Stanton, J. F. & Bartlett, R. J. The equation of motion coupled-cluster method. A systematic biorthogonal approach to molecular excitation energies, transition probabilities, and excited state properties. *J. Chem. Phys.* **98,** 7029–7039 (1993).

214. Tully, J. C. Molecular dynamics with electronic transitions. *J. Chem. Phys.* **93,** 1061–1071 (1990).

215. Köhn, A. & Tajti, A. Can coupled-cluster theory treat conical intersections? *J. Chem. Phys.* **127** (2007).

216. Lin, Y.-S., Li, G.-D., Mao, S.-P. & Chai, J.-D. Long-range corrected hybrid density functionals with improved dispersion corrections. *J. Chem. Theory Comput.* **9,** 263–272 (2013).

217. Epifanovsky, E. *et al.* Software for the frontiers of quantum chemistry: An overview of developments in the Q-Chem 5 package. *J. Chem. Phys.* **155** (2021).

218. Dunning Jr, T. H. Gaussian basis sets for use in correlated molecular calculations. I. The atoms boron through neon and hydrogen. *J. Chem. Phys.* **90,** 1007–1023 (1989).

219. Woon, D. E. & Dunning Jr, T. H. Gaussian basis sets for use in correlated molecular calculations. III. The atoms aluminum through argon. *J. Chem. Phys.* **98,** 1358–1371 (1993).

220. Wilson, A. K., Woon, D. E., Peterson, K. A. & Dunning Jr, T. H. Gaussian basis sets for use in correlated molecular calculations. IX. The atoms gallium through krypton. *J. Chem. Phys.* **110,** 7667–7676 (1999).